

Chalcogenide microwires cladded with hydrogen- and fluorine-based polymers and their applications

Lizhu Li



Department of Electrical & Computer Engineering
McGill University
Montreal, Canada

April 2017

A thesis submitted to McGill University in partial fulfillment of the requirements for the degree of
Doctor of Philosophy.

© 2017 Lizhu Li

Abstract

In this thesis, I introduce the PC- and COP-cladded As_2Se_3 microwires, two highly nonlinear microwires optimized to operate in the wavelength range of 1.85 μm to 2.20 μm . Like the previously reported PMMA-cladded As_2Se_3 microwire, the PC- and COP-cladded microwires benefit of a large waveguide nonlinear parameter and engineerable chromatic dispersion level, but without the absorption features of PMMA in the 1.85 μm to 2.20 μm range. The design rules and fabrication technique of each polymer-cladded microwire is provided. COP- and PMMA-cladded microwires with identical length and waveguide nonlinearity parameter are also operated in the nonlinear regime, highlighting features of self-phase modulation, four-wave mixing and Raman scattering in the 1.85 μm to 2.20 μm range.

Secondly, I demonstrate optical transmission results of highly nonlinear As_2Se_3 optical microwires cladded with fluorine-based CYTOP, and compare them with microwires cladded with typical hydrogen-based polymers. In the linear optics regime, the CYTOP-cladded microwire transmits light in the spectral range from 1.3 μm up to >2.5 μm without trace of absorption peaks such as those observed using hydrogen-based polymer claddings. The microwire is also pumped in the nonlinear optics regime, showing multiple-orders of four-wave mixing and supercontinuum generation spanning from 1.0 μm to >4.3 μm . With such a broadband transparency and high nonlinearity, the As_2Se_3 -CYTOP microwire is an appealing solution for nonlinear optical processing in the mid-infrared.

Finally, I demonstrate all-fiber far-detuned and widely tunable mid-infrared wavelength conversion using As_2Se_3 microwires. In a first experiment, an idler is generated and tuned from 2.351 μm to >2.500 μm from four-wave mixing in a 0.5 cm long microwire. In a second experiment, tunable parametric sidebands are generated via modulation instability in a 10 cm long microwire. The resulting parametric frequency conversion reaches up to 49.3 THz, the largest ever reported in soft glass materials.

Résumé

Dans la première partie de cette thèse, les règles de conception, les techniques de fabrication et les propriétés optiques de deux types de microfils de trisulfure d'arsenic (As_2Se_3) sont présentés: l'un revêtu de polycarbonate (PC) et l'autre de polymère de cyclooléfines (COP). Ces deux types de microfils hautement non-linéaires sont optimisés pour les longueurs d'ondes se situant entre $1.85 \mu\text{m}$ et $2.20 \mu\text{m}$. Tout comme les microfils d' As_2Se_3 revêtus de poly(méthacrylate de méthyle) (PMMA), ceux revêtus de PC et de COP bénéficient d'un grand paramètre de non-linéarité de guide d'ondes ainsi qu'un niveau réglable de dispersion chromatique sans la lacune d'absorption dans la bande de $1.85 \mu\text{m}$ à $2.20 \mu\text{m}$ introduit par le PMMA. De plus, les résultats des expériences effectuées à l'intérieur de cette gamme de longueurs d'ondes démontrant les effets d'automodulation de phase, de mélange à quatre ondes et de diffusion Raman sont présents pour des microfils revêtus de COP et de PMMA de longueurs d'ondes et de paramètres de non-linéarité de guide d'ondes identiques. Dans la deuxième partie, les résultats des expériences de transmission optique effectuées avec des microfils d' As_2Se_3 revêtus du fluoropolymère CYTOP sont présentés et comparés aux propriétés de microfils conventionnels qui sont revêtus de polymères à base d'hydrogène. Dans le régime linéaire, les microfils revêtus de CYTOP transmettent la lumière dans la gamme de longueurs d'ondes allant de $1.3 \mu\text{m}$ jusqu'à-delà de $2.5 \mu\text{m}$ sans aucune trace des traits d'absorption présents pour les revêtements de polymères à base d'hydrogène. Quand les microfils sont opérés dans le régime non-linéaire, des ordres multiples de mélange à quatre ondes ainsi qu'un supercontinuum allant de $1.0 \mu\text{m}$ jusqu'à-delà de $4.3 \mu\text{m}$ sont générés. Grâce à une transparence qui s'étend sur une grande plage de fréquences ainsi que de propriétés hautement non-linéaires, les microfils d' As_2Se_3 -CYTOP présentent une solution attrayante pour le traitement non-linéaire de signaux optiques situés dans l'infrarouge moyen. La dernière partie démontre la conversion de longueur d'onde sur une grande plage de fréquences effectuée à l'aide d'un système entièrement à base de fibres optiques et de microfils d' As_2Se_3 . Dans une première expérience, une onde est générée et réglée à l'intérieur d'une bande allant de $2.351 \mu\text{m}$ jusqu'à-delà de $2.500 \mu\text{m}$ à l'aide d'un mélange à quatre ondes qui se produit dans un microfil de 0.5 cm de longueur. Dans une deuxième expérience, des bandes latérales réglables sont créées à l'aide d'une instabilité modulationnelle à l'intérieur d'un microfil d'une longueur de 10 cm . La conversion de fréquence paramétrique qui en résulte atteint un niveau allant jusqu'à 49.3 THz , ce qui est le plus grand niveau démontré pour un microfil composé d'un matériau du groupe des verres fluors, des verres de chalcogénures et des composés de tellurite.

Acknowledgments

Most importantly, my deepest gratitude goes to my supervisor Professor Martin Rochette for his constant guidance and unlimited support. He taught me how to do the experiments, write papers and present achievements. He provided me invaluable opportunities to attend the conferences for knowledge enhancement and skills improvement. The progress of my PhD project is very slow during the first three years, Prof. Rochette's invaluable encouragements help me to overcome the limitations and to move forward. All of my knowledge about the field of nonlinear optics is from him.

I would love to express my sincere gratitude to all the people who helped me during my PhD project. I want to thank Raja Ahmed showing me how to make the preform, hybrid fiber and hybrid microwire. I want to thank Alaa Al-Kadry showing me how to generate supercontinuum. I want to thank Nurmemet Abdukerim for collaboration and inspiring discussions.

I would like to thank Profs. David Plant, Odile Liboiron-Ladouceur, and Martin Rochette for being on my PhD committee.

My biggest gratitude goes to my parents who provide unstopped support and encouragement since I was born. At the same time, my biggest gratitude goes to my wife for her unlimited support and understanding she gave during my study. Also, my sincere gratitude goes to my sisters and brother-in-laws.

Contents

1	Introduction	1
1.1	ChG microwire	1
1.1.1	Air-cladded ChG microwire	2
1.1.2	PMMA-cladded ChG microwire	3
1.1.3	Other ChG microwires	4
1.2	Motivation	5
1.3	Main contributions	5
1.4	Thesis organization	6
2	Optical parameters and nonlinear effects in ChG microwires	11
2.1	Eigenvalue equation	11
2.2	Optical parameters	13
2.2.1	Refractive index	13
2.2.2	Chromatic dispersion	13
2.2.3	Confinement factor	14
2.2.4	Attenuation	14
2.2.5	Effective mode area	14
2.2.6	Nonlinear refractive index	15
2.2.7	Waveguide nonlinearity parameter	15
2.3	The generalized nonlinear Schrödinger equation	16
2.4	Nonlinear effects	17
2.4.1	Self-phase modulation	17
2.4.2	Cross-phase modulation	18
2.4.3	Modulation instability	19

2.4.4	Four-wave mixing	20
2.4.5	Raman effect	24
3	Design, fabrication and characterization of PC-, COP- and PMMA-cladded ChG microwires	26
3.1	Introduction	26
3.2	The polymer cladding	27
3.2.1	Chemical structure	28
3.2.2	Absorption of polymer	29
3.3	Hybrid microwires fabrication	33
3.3.1	Polymer preparation	34
3.3.2	Microwires fabrication	36
3.4	Modeling	42
3.5	Experimental results	46
3.6	Conclusion	51
4	ChG optical microwires cladded with fluorine-based CYTOP	52
4.1	Introduction	52
4.2	The polymer cladding	53
4.3	Design	56
4.4	Microwire fabrication	59
4.5	Results and discussion	62
4.6	Conclusion	67
5	Mid-infrared wavelength conversion from As₂Se₃ microwires	68
5.1	Introduction	68
5.2	Theory	69
5.3	FWM experiment	74
5.4	MI experiment	77
5.5	Conclusion	79
6	Conclusion	80
	References	83

List of Figures

1.1	Schematic of an air-cladded ChG microtaper.	2
1.2	Schematic of a PMMA-cladded ChG microtaper.	3
1.3	Schematic of a ChG-cladded ChG microtaper.	4
2.1	(a) Schematic of a step-index ChG microwire. (b) Schematic of light propagation in a microwire. (c) Cross section of a microwire. (d) Refractive index profile of a microwire.	12
2.2	Schematic of degenerate FWM and non-degenerate FWM.	21
2.3	Schematic of stimulated Raman scattering from a quantum-mechanical viewpoint.	24
2.4	The measured Raman gain spectrum of As_2Se_3	25
3.1	Chemical structure of COP, PC and PMMA.	29
3.2	Loss mechanisms.	30
3.3	Calculated absorption of fundamental vibration and its overtones of a C-H bond.	32
3.4	Logarithmic plot of viscosity of As_2Se_3 , PC, COP and PMMA at different temperatures.	33
3.5	(a) Vacuum oven used to dry polymer and ChG. (b) Preform without bubble. (c) Preform with bubbles.	35
3.6	(a) Schematic of the polymer-cladded As_2Se_3 preform fabrication setup. (b) Photograph of an extruded preform. (c) Schematic of a hybrid fiber fabrication setup. (d) Reflection optical micrograph of a hybrid fiber.	37
3.7	Polishing setup.	38
3.8	(a) Reflection optical micrograph of cross section of a hybrid fiber. (b) Reflection optical micrograph of the As_2Se_3 -COP core-cladding.	38

3.9	(a) Schematic of the polymer-cladded As_2Se_3 microtaper fabrication setup. The microwire is the thin central section of the microtaper. (b) Schematic of the polymer-cladded As_2Se_3 microtaper coupled to SMF-28 fiber. (c) Photograph of a microtaper.	39
3.10	Schematic of the coupling setup. (a) Input SMF-28 fiber and ChG microtaper alignment. (b) ChG microtaper and output SMF-28 fiber alignment and subsequent UV curing.	40
3.11	(a) Schematic of lateral misalignment. (b) Schematic of longitudinal misalignment. (c) Schematic of angle misalignment.	41
3.12	(a) Refractive index of As_2Se_3 versus wavelength. (b) Refractive index of PC, COP and PMMA versus wavelength.	43
3.13	Calculated coupling efficiency as a function of the COP-cladded As_2Se_3 hybrid fiber core diameter.	44
3.14	(a) Chromatic dispersion β_2 . (b) Waveguide nonlinearity parameter γ . (c) Confinement factor Γ . (d) Effective mode area A_{eff} of the PC-, COP 480R- and PMMA-cladded microwires as a function of the As_2Se_3 core diameter at an operation wavelength of $1.94 \mu\text{m}$.	45
3.15	(a) Schematic of the PC-, COP- and PMMA-cladded As_2Se_3 microtaper. (b) Setup for optical transmission measurement.	47
3.16	(a) Transmission spectra of PC, COP 1020R and PMMA. (b) SMF-28 to SMF-28 transmittance of the PC-, COP 480R-, COP 1020R- and PMMA-cladded microwires with diameter $\phi_{\text{AsSe}} = 1.5 \mu\text{m}$ and length $L_w = 10 \text{ cm}$.	48
3.17	Setup for Raman-enhanced FWM generation. MLFL: mode-locked fiber laser; TDFA: thulium-doped fiber amplifier; BPF: bandpass filter; OSA: optical spectrum analyzer.	49
3.18	Nonlinearly broadened spectra of COP 480R- and PMMA-cladded microwires with length $L_w = 10 \text{ cm}$ and $\gamma = 21.7 \text{ W}^{-1}\text{m}^{-1}$. The peak pump power is 14.1 W and is centered at a wavelength of $1.94 \mu\text{m}$. Transmission spectra are also given for reference.	50
4.1	Chemical structure of fluorine-based polymer CYTOP, hydrogen-based polymer COP and PMMA.	55
4.2	Calculated fundamental and overtones vibrational absorption of a C-F bond and a C-H bond.	56

4.3	Refractive index of As_2Se_3 and CYTOP.	57
4.4	Calculated coupling efficiency as a function of the CYTOP-cladded As_2Se_3 hybrid fiber core diameter.	58
4.5	Optical parameters of CYTOP-cladded As_2Se_3 microwires as a function of wavelength and core diameter: (a) β_2 ; (b) γ ; (c) Γ ; (d) A_{eff}	59
4.6	Fabrication of a polymer-cladded As_2Se_3 fiber. (a) Schematic of the rod-in-tube method used to prepare the extrusion assembly. (b) Schematic of the CYTOP-cladded preform fabrication setup (left) and a photograph of extruded preform (right). (c) Schematic of the CYTOP-cladded fiber fabrication setup (left), photograph of fiber drawing (middle) and an optical reflection photograph of cross section (right).	61
4.7	Schematic of the CYTOP-cladded As_2Se_3 microtaper (not to scale). (b) Photograph of a microtaper with wire section length of 5 cm.	62
4.8	(a) Schematic of the CYTOP-cladded As_2Se_3 microtaper. (b) Setup for transmission loss measurement.	63
4.9	Transmission loss spectra of CYTOP-, COP 1020R-, and PMMA-cladded As_2Se_3 microwires.	64
4.10	Setup for Raman-enhanced FWM generation. MLFL: mode-locked fiber laser; TDFA: thulium-doped fiber amplifier; BPF: bandpass filter; OSA: optical spectrum analyzer.	64
4.11	Nonlinearly broadened spectra of CYTOP-cladded As_2Se_3 microwire at various pump powers. The legend presents corresponding coupled peak (average) powers.	65
4.12	Setup for SC generation. MLFL: mode-locked fiber laser; TDFA: thulium-doped fiber amplifier; BPF: bandpass filter; FTIR: Fourier Transform Infrared Spectrometer.	66
4.13	SC spectra at various coupled pump powers for a CYTOP-cladded microwire with an As_2Se_3 core diameter of 1.55 μm	66
4.14	SC spectra of CYTOP- and COP-cladded microwires at a peak (average) pump power of 1044 W (100 mW).	67
5.1	Schematic of the As_2Se_3 -CYTOP microtaper.	70
5.2	(a) β_2 as a function of wavelength and As_2Se_3 microwire core diameter. (b) β_4 as a function of wavelength and As_2Se_3 microwire core diameter. (c) β_6 as a function of wavelength and As_2Se_3 microwire core diameter.	72

5.3	Phase-matched parametric wavelengths as a function of As_2Se_3 microwire core diameter. The pump wavelength is set at $1.939 \mu\text{m}$ and the peak pump power is set at 32 W, 46 W and 95 W. The dotted line indicates the zero dispersion diameter at the pump wavelength. The microwire design includes a CYTOP cladding.	73
5.4	Schematic of the pump-probe FWM setup. MLFL: mode-locked fiber laser; BPF: bandpass filter; FC: fiber coupler; PC: polarization controller; OSA: optical spectrum analyzer.	74
5.5	(a) Measured output spectra. The legend presents corresponding probe wavelengths. The inset graph shows the zoomed-in spectra of the output idlers. (b) Conversion efficiency versus idler wavelength.	75
5.6	(a) The output peak idler power as a function of input probe power at a fixed peak pump power $P_0=3.5 \text{ W}$ and a fixed input probe wavelength of $1.587 \mu\text{m}$. (b) The output peak idler power as a function of peak pump power at a fixed input probe wavelength and power of $1.587 \mu\text{m}$ and 0.54 mW , respectively.	76
5.7	Experimental setup. MLFL: mode-locked fiber laser; TDFA: thulium-doped fiber amplifier; FTIR: Fourier Transform Infrared Spectrometer.	77
5.8	(a) Measured output spectra of MI of an As_2Se_3 microwire with a core diameter of $1.625 \mu\text{m}$ and a length of 10 cm. (b) Measured and calculated parametric wavelengths as a function of peak pump power.	78

List of Tables

3.1	Common C-H based polymers and their physical parameters	28
3.2	Vibrational wavelengths of different chemical bonds	32
3.3	Glass transition temperature and refractive index at 1.94 μm of ChG and polymers	34
3.4	Drying temperature and drying time of different polymers	35
3.5	Cauchy coefficients of PC, COP and PMMA	42
3.6	Dispersion, nonlinearity and confinement properties of PMMA-, PC-, and COP 480R-cladded microwires at an operation wavelength of 1.94 μm . γ_{max} : maximum γ ; $d_{\gamma_{\text{max}}}$: diameter corresponding to maximum γ	46
4.1	Common fluorine-based polymers and their physical parameters	54
4.2	Vibrational wavelengths of different chemical bonds	56
4.3	Glass transition temperature, refractive index ($\lambda=1.94 \mu\text{m}$) and viscosity ($T=210 \text{ }^\circ\text{C}$) of As_2Se_3 , CYTOP and PMMA	60

List of Acronyms

ChG	Chalcogenide
C-H	Carbon hydrogen single bond
C-F	Carbon fluorine single bond
C-C	Carbon carbon single bond
C-O	Carbon oxygen single bond
C=O	Carbon oxygen double bond
PMMA	Polymethyl methacrylate
PC	Polycarbonate
COP	Cyclo Olefin Polymer
CYTOP	Cyclized Transparent Optical Polymer
ZDW	Zero dispersion wavelength
SMF	Single mode fiber
SPM	Self-phase modulation
XPM	Cross-phase modulation
MI	Modulation instability
FWM	Four-wave mixing
SRS	Stimulated Raman scattering
SC	Supercontinuum
OPO	Optical parametric oscillator
CE	Conversion efficiency
MLFL	Mode-locked fiber laser
BPF	Bandpass filter
FC	Fiber coupler
PC	Polarization controller

OSA	Optical spectrum analyzer
TDEFA	Thulium-doped fiber amplifier
FTIR	Fourier transform infrared spectrometer

Chapter 1

Introduction

1.1 ChG microwire

Mid-infrared devices based on nonlinear effects are in strong demand for many applications. For practical considerations, it is desirable to use a nonlinear medium with large waveguide nonlinearity parameter $\gamma = k_0 n_2 / A_{\text{eff}}$, where k_0 is the wavenumber, n_2 is the nonlinear refractive index, and A_{eff} is the effective mode area. A large γ enables compact nonlinear devices with low power consumption. One approach towards enhancing γ is to choose a material with a large n_2 . Chalcogenide glasses are excellent candidates to serve as nonlinear engines because their n_2 is up to a factor of 1000 larger than that value of the widespread silica glass [1]. Moreover, the wide transparency of ChG glasses is ideal for applications in the mid infrared (MIR): Arsenic selenide (As_2Se_3) transmits light from 1 to 12 μm [2]; Arsenic sulfide (As_2S_3) transmits light from 1 to 8 μm [3]. ChG glasses also have negligible two-photon absorption and free carrier absorption in the MIR [4, 5]. Another approach towards enhancing γ is to choose a waveguide structure with a small A_{eff} , such as the microwire [6]. The microwire squeezes the mode down to a diameter in the order of the operation wavelength and thus minimizes A_{eff} . As a result, the nonlinear waveguide parameter of ChG microwires is increased by more than 5 orders of magnitude in comparison with silica fibers [7]. The zero dispersion wavelengths of bulk ChG glasses (As_2Se_3 and As_2S_3) are in the MIR, i.e. $\sim 7 \mu\text{m}$ for As_2Se_3 [8, 9] and $\sim 5 \mu\text{m}$ for As_2S_3 [10]. Chromatic dispersion engineering can be easily achieved in ChG waveguides by properly choosing a waveguide geometry to compensate the large and normal material dispersion of ChG glasses. As a result, the zero-dispersion wavelength could be shifted down to the telecommunication bands. At those wavelengths, many compact semiconductor lasers and fiber lasers are available, thus providing accesses to taking advantage of

nonlinear effects [11, 12].

1.1.1 Air-cladded ChG microwire

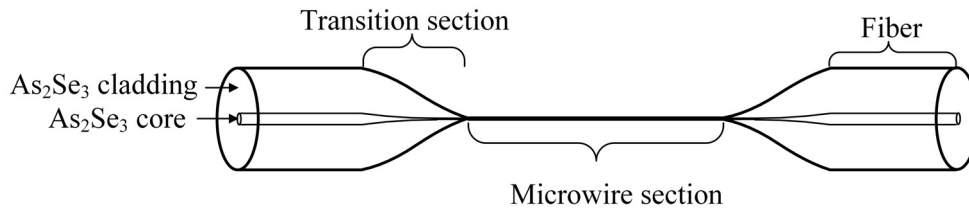


Fig. 1.1 Schematic of an air-cladded ChG microtaper.

The first demonstration of ChG microwire was an air-cladding microwire leading to high nonlinearity and engineerable chromatic dispersion [13]. Figure 1.1 shows the schematic of an air-cladded ChG microtaper. Using air-cladded ChG microwires, a number of supercontinuum (SC) generations have been demonstrated. In As_2Se_3 microwires, Yeom et al. firstly demonstrated a SC from $1.15 \mu\text{m}$ to $1.70 \mu\text{m}$ using a microwire with a diameter of $0.95 \mu\text{m}$ and a wire section length of 3 cm pumped by a $1.55 \mu\text{m}$ pulsed laser with a pulse duration of 250 fs and a peak pump power of 7.8 W [11]. Al-Kadry et al. demonstrated a SC that spans from $1.26 \mu\text{m}$ to $2.20 \mu\text{m}$ using a microwire with a diameter of $1.28 \mu\text{m}$ and a wire section length of 10 cm pumped by a $1.77 \mu\text{m}$ Raman soliton source with a pulse duration of 90 fs and a peak pump power of 156 W [5]. Al-Kadry et al. also demonstrated a SC that covers two octaves spanning from $1.1 \mu\text{m}$ to $4.4 \mu\text{m}$ using a microwire with a diameter of $1.6 \mu\text{m}$ and a wire section length of 10 cm pumped by a $1.94 \mu\text{m}$ mode-locked fiber laser with a pulse duration of 3 ps and a peak pump power of 167 W [14]. Duhant et al. demonstrated a SC that spans from $1.3 \mu\text{m}$ to $2.6 \mu\text{m}$ using a microstructure microwire with a diameter of $0.8 \mu\text{m}$ and a wire section length of 5 cm pumped by a $1.96 \mu\text{m}$ mode-locked fiber laser with a pulse duration of 4 ps and a peak pump power of 150 W [15]. In As_2S_3 microwires, Marandi et al. demonstrated a SC that spans from $2.2 \mu\text{m}$ to $5.0 \mu\text{m}$ using a microwire with a diameter of $2.3 \mu\text{m}$ and a wire section length of 2.1 mm pumped by a $3.1 \mu\text{m}$ optical parametric oscillator (OPO) with a pulse duration of sub-100 fs and a peak pump power of 2.5 kW [16]. Hudson et al. demonstrated a SC spanning from $0.97 \mu\text{m}$ to $>2 \mu\text{m}$ using a microwire with a diameter of $1.3 \mu\text{m}$ and a wire section length of 5 cm pumped by a $1.55 \mu\text{m}$ mode-locked fiber laser with a pulse duration of 0.25 ps and a peak pump power of 824 W [12]. C. W. Ruby et al. demonstrated a SC spanning from $1.0 \mu\text{m}$ to $3.7 \mu\text{m}$ using a microwire with a

diameter of $1.95\ \mu\text{m}$ and a wire section length of $2.1\ \text{mm}$ pumped by a $2.04\ \mu\text{m}$ mode-locked fiber laser with a pulse duration of sub-100 fs and a peak pump power of $\sim 3\ \text{kW}$ [17]. Finally, Markos et al. demonstrated nonlinear modulation instability (MI)-based fiber optical biosensor with sensitivity of $\sim 18\ \text{nm/nm}$ using a microwire with a diameter of $0.6\ \mu\text{m}$ and a wire section length of $1.2\ \text{cm}$ pumped by a $1.064\ \mu\text{m}$ Nd:YAG pulsed laser with a peak pump power of $0.5\ \text{W}$ [18].

Despite the successful demonstrations of supercontinuum generation and biosensing using air-cladded ChG microwires, they have unfortunately limited usefulness because of their extreme mechanical fragility due to their thin geometries.

1.1.2 PMMA-cladded ChG microwire

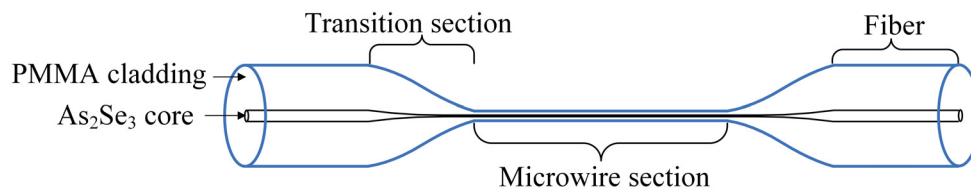


Fig. 1.2 Schematic of a PMMA-cladded ChG microtaper.

To enhance the mechanical strength of air-cladded ChG microwires, Baker et al. have successfully fabricated the first hybrid ChG microwire, which consists of a ChG core coated with PolyMethyl MethAcrylate (PMMA) [19]. Fig. 1.2 shows the schematic of a PMMA-cladded ChG microtaper. The PMMA cladding provides mechanical strength to the ChG microwire and protects it from environmental contamination and degradation. Being now a practical component, the hybrid ChG microwire has been used for several applications at telecommunication wavelengths: Ahmad et al. demonstrated the first ChG microwire based parametric oscillator with oscillation at the output wavelength of $1.502\ \mu\text{m}$ (Anti-stokes) and $1.605\ \mu\text{m}$ (Stokes) [20]. The oscillator has a low peak power threshold of $145\ \text{mW}$ and a conversion efficiency of $>19\%$. Ahmad et al. demonstrated the first ChG microwire based Fabry-Perot Raman laser with output wavelength of $1.605\ \mu\text{m}$ [21]. The Raman laser has a peak power threshold of $470\ \text{mW}$ and a conversion efficiency of $\sim 0.25\%$. Ahmad et al. demonstrated broadband four-wave mixing (FWM) in ChG microwires with conversion bandwidth up to $190\ \text{nm}$ and conversion efficiency up to $21\ \text{dB}$ at the peak pump power as low as $70\ \text{mW}$ [22]. Ahmad et al. demonstrated Raman parametric laser, wavelength converter and wavelength amplifier in a single microwire with a low threshold peak pump power of $207\ \text{mW}$

and a slope efficiency of $>2\%$ [23]. Ahmad et al. demonstrated Bragg grating writing in ChG microwires [24]. The writing of Bragg grating in the $1.55\ \mu\text{m}$ band was demonstrated with an extinction ratio of 40 dB in transmission. Al-Kadry et al. demonstrated an all-normal dispersion supercontinuum generation spans from $0.96\ \mu\text{m}$ to $>2.5\ \mu\text{m}$ in a ChG microwire with a diameter of $0.58\ \mu\text{m}$ and a wire section length of 3 mm pumped by a $1.55\ \mu\text{m}$ mode-locked fiber laser with a peak pump power of 248 W [25]; Dot et al. converted one photon into two via FWM in a microwire with a diameter of $0.555\ \mu\text{m}$ and a wire section length of 10 cm with a peak pump power of 800 mW and a conversion efficiency of 1.1×10^{-3} [26]; Meyer-Scott et al. have produced photon pairs with coincidences-to-accidentals ratios of 2.13 via degenerate FWM in a ChG microwire with a diameter of $0.55\ \mu\text{m}$ and a wire section length of 12 cm with a low peak pump power of 10 mW [27]; Beugnot et al. have demonstrated the PMMA cladding has served to reduce and control stimulated Brillouin scattering [28]. Godin et al. demonstrated normal dispersion MI with output wavelength of $2.0\ \mu\text{m}$ (Anti-stokes) and $3.5\ \mu\text{m}$ (Stokes) in a microwire with a diameter of $3.6\ \mu\text{m}$ and a wire section length of 14 cm pumped by a solid-state OPO with a peak pump power of 10 W [29]. Finally, Al-Kadry et al. demonstrated several oscillation modes in a self-pulsating fiber laser cavity based on an As_2S_3 -PMMA microwire with a diameter of $1.7\ \mu\text{m}$ and a length of 10 cm [30].

Although PMMA-cladded ChG microwires have been successfully used as nonlinear media in many demonstrations at telecommunication bands, the PMMA cladding however becomes absorptive beyond $1.55\ \mu\text{m}$ due to the first order vibrational overtone of carbon hydrogen (C-H) bonds and limits the usefulness of PMMA-cladded ChG microwires in the MIR region [31].

1.1.3 Other ChG microwires

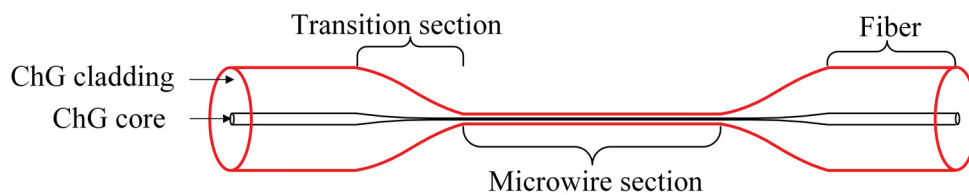


Fig. 1.3 Schematic of a ChG-cladded ChG microtaper.

Sun et al. demonstrated MIR-transparent As_2S_3 -cladded As_2Se_3 microwires [32]. Fig. 1.3 shows the schematic of an As_2S_3 -cladded As_2Se_3 microtaper. However, the zero dispersion wavelength

of this material combination can only be $>3.7 \mu\text{m}$ because the waveguide dispersion of such a microwire can not compensate the normal material dispersion for a pump wavelength $<3.7 \mu\text{m}$ due to the low refractive index contrast between As_2Se_3 core and As_2S_3 cladding. As a result, nonlinear processes requiring anomalous or zero dispersion (e.g. parametric amplification, self-phase modulation-based solitons) in the wavelength range of $1.5\text{-}3.7 \mu\text{m}$ can not be triggered. Liao et al. demonstrated tellurite-cladded As_2S_3 microstructure microwires [33]. Unfortunately, this kind of microwire can not be fabricated using rod-in-tube method [34] and can be fabricated via only stack-and-draw method [35]. Another alternative to PMMA cladding is the use of silica cladding [36]. Unfortunately, the softening temperature of silica is more than 1000°C higher than that value of ChG glasses [2, 37]. As a result, the silica-cladded ChG microwires can not be fabricated through the conventional thermal drawing technique.

1.2 Motivation

The mid-infrared (MIR) range ($2\text{-}5 \mu\text{m}$) raises a great deal of interest due to their potential applications in military defense systems, medical applications and communication technologies [38–47]. This spectral range is of significant importance for many important military applications, such as missile countermeasures [48, 49], eye safe laser radar [50], and infrared illuminator [51]. Aside from military applications, this spectral range is of interest for invasive diagnostic [52], precise surgical procedures [53], and medical tissue ablation due to its high water absorption [53]. In addition, this spectral range has been identified as essential to spectroscopic and sensing-based applications because of characteristic molecular vibrational frequencies within this wavelength range [38, 54, 55]. Within the available approaches to build compact MIR sources, light sources that depend on nonlinear parametric gain, such as parametric oscillators [56] and SC sources [57] are of great importance due to their large spectrum coverage. For each of those parametric processes-based nonlinear devices, the nonlinear gain medium should be characterized by a significant nonlinear refractive index, a good MIR transparency and an easy access to zero chromatic dispersion. For this purpose, MIR transparent materials that have a low refractive index and are mechanically robust are needed to clad ChG microwires.

1.3 Main contributions

The main contributions of this thesis are:

Polycarbonate (PC) and Cyclo Olefin Polymer (COP)-cladded As₂Se₃ microwires

I demonstrate the design principles and fabrication procedures of PC- and COP-cladded As₂Se₃ microwires. The transmission wavelength ranges and transmission losses of those microwires are characterized within 1.45-2.20 μm and compared with values of PMMA-cladded microwires. Also, Raman-enhanced cascaded four wave mixing is demonstrated in a COP-cladded As₂Se₃ microwire and shows an increased gain and wider gain bandwidth, compared with PMMA-cladded microwires.

Fluorine-based Cyclic Transparent Optical Polymer (CYTOP)-cladded As₂Se₃ microwires

I demonstrate and present the first MIR transparent polymer-cladded As₂Se₃ optical microwires. The polymer cladding is fluorine-based CYTOP. The transmission losses of CYTOP-cladded As₂Se₃ microwires is provided in the spectral range from 1.3 μm up to $>2.5 \mu\text{m}$ without trace of absorption peaks such as those observed using hydrogen-based polymer claddings. Also, Raman-enhanced cascaded FWM is shown from low pump power. A SC generation spanning from 1.0 μm up to 4.3 μm is demonstrated using a CYTOP-cladded microwire.

Mid infrared wavelength conversion from As₂Se₃ microwires for fiber-based sources

I present the first demonstration of all-fiber far-detuned and widely tunable MIR wavelength converters. Both pump-probe scheme and pump-only scheme are investigated. In the case of pump-probe scheme, the theoretical and experimental conversion efficiency are compared. In the case of pump-only scheme, tunable parametric sidebands are generated via MI. The pump power dependence of parametric wavelengths is demonstrated and in good agreement with calculated results. The resulting parametric frequency conversion reaches up to 49.3 THz, the largest ever reported in soft glass materials.

1.4 Thesis organization

The organization of the thesis is summarized as follows:

Chapter 2 introduces optical parameters and nonlinear effects in As₂Se₃ microwires. The introduced optical parameters include refractive index n , transmission loss α , chromatic dispersion β_m , nonlinear waveguide parameter γ , confinement factor Γ , and effective mode area A_{eff} . The in-

roduced nonlinear effects include self-phase modulation (SPM), cross-phase modulation (XPM), FWM, MI, and Raman effect.

Chapter 3 presents the optical performance of PC- and COP-cladded As_2Se_3 optical microwires. Firstly, factors affecting the design and fabrication of PC- and COP-cladded As_2Se_3 microwires have been investigated. Secondly, the optical parameters, including chromatic dispersion β_2 , nonlinear waveguide parameter γ , confinement factor Γ , and effective mode area A_{eff} , are simulated. Thirdly, the transmission losses of PC- and COP-cladded microwires are characterized. Finally, the efficiency of nonlinear processes between a COP 480R-cladded and a PMMA-cladded As_2Se_3 microwire is compared.

Chapter 4 presents the optical performance of fluorine-based CYTOP-cladded As_2Se_3 microwires. Firstly, the physical and optical properties of fluorine-based CYTOP has been introduced. Secondly, the optical parameters, including chromatic dispersion β_2 , nonlinear waveguide parameter γ , confinement factor Γ , and effective mode area A_{eff} , are simulated. Thirdly, The transmission loss of a CYTOP-cladded microwire is investigated. Fourthly, Raman-enhanced FMW in a CYTOP-cladded microwire is demonstrated. Finally, A SC generation in a CYTOP-cladded microwire is demonstrated.

Chapter 5 presents the all-fiber far-detuned and widely tunable MIR wavelength conversion from CYTOP-cladded As_2Se_3 microwires. Firstly, the relationship between phase-matched parametric wavelengths and microwire core diameters is calculated. Secondly, the pump-probe scheme is applied to achieve stimulated FWM in a 0.5 cm long microwire. Finally, the pump-only scheme is applied to achieve normal dispersion MI in a 10 cm long microwire.

Chapter 6 concludes the thesis and suggests some future works.

List of publications

Journal publications

Journal publication 1

L. Li, A. Al-Kadry, N. Abdukerim and M. Rochette, Design, fabrication and characterization of PC, COP and PMMA-cladded As_2Se_3 microwires, *Opt. Mater. Express* 6(3), 912-921 (2016).

Contributions:

L. Li: Performed experiment and prepared manuscript.

A. Al-Kadry: Shared ideas and technical support

N. Abdukerim: Shared ideas and technical support

M. Rochette: Prepared manuscript and supervised the project.

Journal publication 2

L. Li, N. Abdukerim, and M. Rochette, Chalcogenide optical microwires cladded with fluorine-based CYTOP, *Opt. Express* 24(17), 18931-18937 (2016).

Contributions:

L. Li: Performed experiment and prepared manuscript.

N. Abdukerim: Shared ideas and technical support

M. Rochette: Prepared manuscript and supervised the project.

Journal publication 3

L. Li, N. Abdukerim, and M. Rochette, Mid infrared wavelength conversion from As_2Se_3 microwires, *Opt. Lett.* 42(3), 639-642 (2017).

Contributions:

L. Li: Performed experiment and prepared manuscript.

N. Abdukerim: Shared ideas and technical support

M. Rochette: Prepared manuscript and supervised the project.

Other journal publications

A. Al-Kadry, L. Li, M. El Amraoui, T. North, Y. Messaddeq, and M. Rochette, Broadband supercontinuum generation in all-normal dispersion chalcogenide microwires, *Opt. Lett.* 40(20), 4687-4690 (2015).

N. Abdukerim, L. Li and M. Rochette, Chalcogenide-based optical parametric oscillator at 2 μm , *Opt. Lett.* 41(18), 4364-4367 (2016).

N. Abdukerim, L. Li, M. El Amraoui, Y. Messaddeq, and M. Rochette, 2 μm Raman fiber laser based on a multimaterial chalcogenide microwire, Accepted by *Appl. Phys. Lett.*, 2017.

E. Meyer-Scott, A. Dot, R. Ahmad, L. Li, M. Rochette, and T. Jennewein, "Power-efficient production of photon pairs in a tapered chalcogenide microwire," *Appl. Phys. Lett.* 106, 081111 (2015).

Conference publications

L. Li, A. Al-Kadry, and M. Rochette, "Design, fabrication and characterization of polymer-coated As_2Se_3 microwires," at Photonics North, Materials-10-31-2, Ottawa, Ontario, June 2015.

L. Li, N. Abdukerim and M. Rochette, Fabrication and characterization of an As_2Se_3 optical microwire cladded with perfluorinated CYTOP, at the IEEE/OSA Conference for Lasers and Electro-Optics (CLEO), SW4R.4, San Jose, California, June 2016.

Other conference publications

N. Abdukerim, L. Li, and M. Rochette, "Mid-infrared raman fiber laser in chalcogenide microwire," at Photonics North, Nonlinear-4-29-6, Ottawa, Ontario, June 2015.

A. Al-Kadry, L. Li, T. North, M. El Amraoui, Y. Messaddeq, and M. Rochette, "Broadband su-

percontinuum generation in all-normal dispersion chalcogenide microwires,” at Photonics North, Materials-10-31-4, Ottawa, Ontario, June 2015.

E. Meyer-Scott, A. Dot, R. Ahmad, L. Li, T. Jennewein, and M. Rochette, ”Producing photon pairs with ultralow pump powers,” at Photonics North, Nonlinear-10-14-1, Ottawa, Ontario, June 2015.

E. Meyer-Scott, A. Dot, R. Ahmad, L. Li, M. Rochette and T. Jennewein, Can four-wave mixing be pumped by a single photon?, at Single Photon Workshop (SPW2015), Th47, Geneva, Switzerland, July 2015.

D. M. Chow, J. C. Tchahame, A. Denisov, J.-C. Beugnot, T. Sylvestre, L. Li, R. Ahmad, M. Rochette, K. H. Tow, M. A. Soto, L. Thevenaz, Mapping the uniformity of optical microwires using phase-correlation brillouin distributed measurements, at Frontiers of Optics (FIO), San Jose, California, October 2015.

N. Abdukerim, L. Li and M. Rochette, Chalcogenide-based optical parametric oscillator, at the IEEE/OSA Conference for Lasers and Electro-Optics (CLEO), STh1O.4, San Jose, California, June 2016.

Chapter 2

Optical parameters and nonlinear effects in ChG microwires

In this chapter, the theory to model pulse propagation in a ChG microwire is introduced. Section 2.1 introduces the step-index microwire structure, the well-known eigenvalue equation governing the propagating modes and the important optical parameters, including chromatic dispersion β_m , confinement factor Γ , effective mode area A_{eff} , waveguide nonlinearity parameter γ and their frequency dependence. Section 2.2 introduces a number of nonlinear effects, including SPM, XPM, MI, FWM, and Raman effect. The generalized nonlinear Schrödinger equation including chromatic dispersion, attenuation, Kerr effect, self-steepening effect and Raman effect is also introduced.

2.1 Eigenvalue equation

A polymer-cladded ChG microwire consists of a ChG core with refractive index n_1 surrounded by a polymer cladding layer with refractive index n_2 , lower than n_1 . Figure 2.1 (a), (b), (c) and (d) schematize a step-index ChG microwire, light propagation in a microwire, cross section of a microwire and refractive index profile of a microwire, respectively. Eigenvalue equation is derived from Maxwell's equations by matching the boundary conditions at the core-cladding interface of a microwire, and used to determine the propagation constant β and field distributions of a propagation mode [58]. To derive β_2 , Γ , A_{eff} , and γ , the effective refractive index and the electric and magnetic field distribution of the fundamental mode in a microwire need to be calculated by solving the eigenvalue equation without making any approximation due to the high refractive index

contrast between the ChG core and polymer cladding.

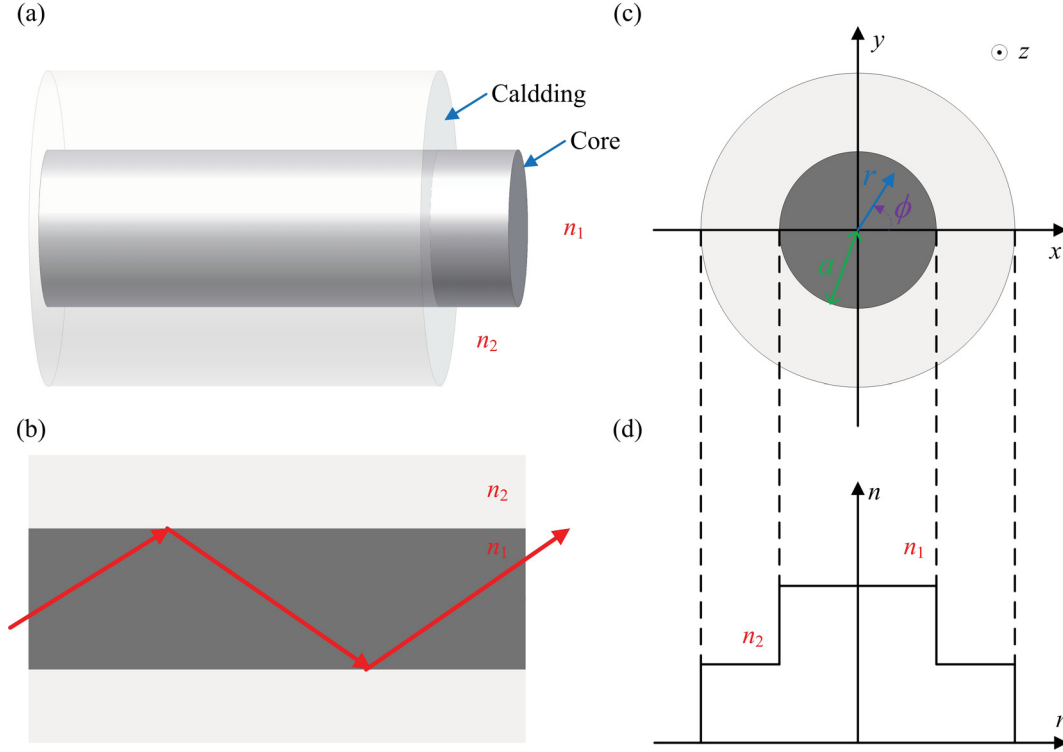


Fig. 2.1 (a) Schematic of a step-index ChG microwire. (b) Schematic of light propagation in a microwire. (c) Cross section of a microwire. (d) Refractive index profile of a microwire.

The well-known eigenvalue equation is defined as [59]

$$\left[\frac{J'_m(pa)}{pJ_m(pa)} + \frac{K'_m(qa)}{qK_m(qa)} \right] \left[\frac{J'_m(pa)}{pJ_m(pa)} + \frac{n_2^2 K'_m(qa)}{n_1^2 qK_m(qa)} \right] = \left(\frac{m\beta k_0(n_1^2 - n_2^2)}{an_1 p^2 q^2} \right)^2 \quad (2.1)$$

where $J_m(x)$ is the Bessel function, $J'_m(x)$ is the differentiation of $J_m(x)$, $K_m(x)$ is the modified Bessel function, $K'_m(x)$ is the differentiation of $K_m(x)$, k_0 is the wavenumber, n_1 is the refractive index of ChG core, n_2 is the refractive index of polymer cladding, a is the radius of ChG core, p is defined as $p=(n_1^2 k_0^2 - \beta^2)^{\frac{1}{2}}$, q is defined as $q=(\beta^2 - n_2^2 k_0^2)^{\frac{1}{2}}$, propagation constant β is the only unknown parameter in the eigenvalue equation, and can be found by solving the Eq. 2.1.

2.2 Optical parameters

2.2.1 Refractive index

The refractive indices of the ChG core and polymer cladding are frequency dependent. When the operation wavelength is far away from the medium resonances, the relationship between the refractive index and the operation wavelength is approximated by the Sellmeier equation [60]

$$n^2(\omega) = 1 + \sum_{j=1}^m \frac{A_j^2 \omega_j^2}{\omega_j^2 - \omega^2} \quad (2.2)$$

where ω_j is the resonance frequency and A_j is the strength of j th resonance. Equivalently,

$$n^2(\lambda) = 1 + \sum_{j=1}^m \frac{A_j^2 \lambda^2}{\lambda^2 - \lambda_j^2} \quad (2.3)$$

where λ_j is the resonance wavelength.

2.2.2 Chromatic dispersion

Chromatic dispersion is a critical parameter used to describe the pulse propagation inside a microwire because different frequency components of the involved pulse travel at different velocities depending on the frequency dependence of the refractive index $n(\omega)$. Substituting the frequency dependent n into the eigenvalue equation Eq. 2.1, the propagation constant β and effective refractive index n_{eff} of the fundamental mode are obtained. The propagation constant β might be expanded in a Taylor series around the frequency $\omega = \omega_0$ [59]

$$\beta(\omega) = n_{\text{eff}}(\omega) \frac{\omega}{c} = \beta_0 + \beta_1(\omega - \omega_0) + \frac{1}{2}\beta_2(\omega - \omega_0)^2 + \frac{1}{6}\beta_3(\omega - \omega_0)^3 + \dots \quad (2.4)$$

where

$$\beta_m = \left(\frac{d^m \beta}{d\omega^m} \right)_{\omega=\omega_0} \quad (m = 0, 1, 2, \dots) \quad (2.5)$$

β_0 is the propagation constant at the frequency ω_0 , β_1 is the group velocity, the higher coefficients $\beta_2, \beta_3, \dots, \beta_m$ are the second, third, ..., m th order dispersion coefficients.

2.2.3 Confinement factor

As light propagates inside a microwire, some fraction of light propagates in the cladding of a microwire as evanescent waves. The confinement factor Γ describes the fraction of total optical power enclosed inside the core of a microwire and is defined as [61]

$$\Gamma = \frac{P_c}{P_t} = \frac{\int_0^a \int_0^{2\pi} \text{Re}(\vec{E} \times \vec{H}^*) \cdot \hat{z} r dr d\phi}{\int_0^\infty \int_0^{2\pi} \text{Re}(\vec{E} \times \vec{H}^*) \cdot \hat{z} r dr d\phi} \quad (2.6)$$

where P_c is the optical power enclosed inside the ChG core, P_t is the total optical power inside the microwire structure, a is the radius of ChG core, \vec{E} is the electric field vector, \vec{H} is the magnetic field vector, r , ϕ , and z are the cylindrical coordinates, as shown in Fig. 2.1(c).

2.2.4 Attenuation

The attenuation coefficient describes the fraction of incident light that is absorbed after passing through unit length of a microwire. The attenuation coefficient of a microwire is defined as

$$\alpha_{\text{total}} = \alpha_{\text{core}} \times \Gamma_{\text{core}} + \alpha_{\text{cladding}} \times \Gamma_{\text{cladding}} \quad (2.7)$$

where α_{total} is the attenuation coefficient of the microwire, α_{core} is the attenuation coefficient of ChG core material, α_{cladding} is the attenuation coefficient of polymer cladding material, Γ_{core} is the confinement factor of microwire core section, Γ_{cladding} is the confinement factor of microwire cladding section.

2.2.5 Effective mode area

The effective mode area is an important parameter for describing the optical performance of a microwire. It strongly depends on the refractive index contrast between core material and cladding material of a microwire. When the refractive index contrast is small, the effective mode area A_{eff} is derived using scalar analysis [59] and defined as

$$A_{\text{eff}} \approx \frac{\left[\iint_{-\infty}^{\infty} |F(x, y)|^2 dx dy \right]^2}{\iint_{-\infty}^{\infty} |F(x, y)|^4 dx dy} \quad (2.8)$$

where $F(x, y)$ is the scalar electric field distribution.

When the refractive index contrast is large, the effective mode area A_{eff} must be derived using vector analysis [62, 63] and is defined as

$$A_{\text{eff}} = \frac{|\iint_{\infty} [\vec{E} \times \vec{H}^*] \cdot \hat{z} dA|^2}{\iint_{\infty} |[\vec{E} \times \vec{H}^*] \cdot \hat{z}|^2 dA} \quad (2.9)$$

where \vec{E} and \vec{H} are the electric and magnetic field vectorial distribution, respectively. \hat{z} is the propagation direction. A is the cross section area.

2.2.6 Nonlinear refractive index

Combined two-level bond orbital approximation method [64] and the dispersion of the Kerr coefficient for crystalline solids based on Kramers-Kronig relation [65], the nonlinear refractive index n_2 of As_2Se_3 is calculated by the following equation [1]

$$n_2 = \frac{1.7 \times 10^{-20} (n_0^2 + 2)^3 (n_0^2 - 1) d^2}{n_0^2 E_s^2} G_2 \left(\frac{\hbar\omega}{E_g} \right) \quad (2.10)$$

where the unit of n_2 is $\text{m}^2 \cdot \text{W}^{-1}$, n_0 is the linear refractive index, $d=0.243$ nm, $\hbar=6.58 \times 10^{-16}$ eV·s, $E_g=1.77$ eV, $E_s=3.8$ eV. The dispersion function is described by $G_2(x, x) = g(x) + g(-x)$, where $g(x)$ is defined as [66]

$$g(x) = -\frac{8}{x^4} - \frac{10}{x^5} (1-x)^{\frac{3}{2}} + \frac{8}{x^5} (1-2x)^{\frac{3}{2}} + \frac{17}{x^4} (1-x)^{\frac{1}{2}} - \frac{2}{x^3} (1-x)^{-\frac{1}{2}} - \frac{1}{4x^2} (1-x)^{-\frac{3}{2}} \quad (2.11)$$

2.2.7 Waveguide nonlinearity parameter

The waveguide nonlinearity parameter γ is an important parameter used to evaluate the efficiency of nonlinear effects in a microwire. γ depends not only on nonlinear refractive index n_2 , but also on effective mode area A_{eff} . Using scalar analysis [59], γ is defined as

$$\gamma \approx \frac{k_0 n_2}{A_{\text{eff}}} \quad (2.12)$$

where k_0 is the wavenumber, n_2 is the nonlinear refractive index, and A_{eff} is the effective mode area described in Eq. 2.8. However, the vector analysis [67–69], instead of scalar analysis, must be applied for obtaining the optical parameters of polymer-cladded ChG microwires due to the high

refractive index contrast between the ChG core and polymer cladding. Using vector analysis, the waveguide nonlinearity parameter γ is defined as [62, 63]

$$\gamma = \frac{k_0 \bar{n}_2}{A_{\text{eff}}} \quad (2.13)$$

where A_{eff} is given by Eq. 2.9 and \bar{n}_2 is effective material nonlinearity given by [62, 63]

$$\bar{n}_2 = \frac{\varepsilon_0}{\mu_0} \frac{\iint_{\infty} n_0^2(x, y) n_2(x, y) (2|\vec{E}|^4 + |\vec{E}^2|^2) dA}{3 \iint_{\infty} |[\vec{E} \times \vec{H}^*] \cdot \hat{z}|^2 dA} \quad (2.14)$$

where ε_0 is the electric permittivity of vacuum; μ_0 is the magnetic permeability of vacuum; n_0 is the linear refractive index; n_2 is the nonlinear refractive index; \vec{E} and \vec{H} are the electric and magnetic field vectorial distribution, respectively; \hat{z} is the propagation direction; A is the cross section area.

2.3 The generalized nonlinear Schrödinger equation

Assuming the light polarized along the x-axis, the electric field of the fundamental mode HE_{11} in the microwire is given by [59]

$$\mathbf{E}(\mathbf{r}, t) = \frac{1}{2} \hat{x} \{ F(x, y) A(z, t) \exp[i(\beta z - \omega_0 t)] + \text{c.c.} \} \quad (2.15)$$

where $\mathbf{r} = (x, y, z)$, \hat{x} is the polarization unit vector, $F(x, y)$ is the transverse field distribution, $A(z, t)$ is the pulse envelope, and β is the propagation constant. The changes in pulse envelope A as the pulse propagates along the microwire axis z is described by the generalized nonlinear Schrödinger equation [70, 71]

$$\begin{aligned} \frac{\partial A}{\partial z} = & i \sum_{m=1}^{\infty} \frac{i^m \beta_m}{m!} \frac{\partial^m A}{\partial t^m} - \frac{1}{2} \left(\alpha(\omega_0) + i \alpha_1 \frac{\partial}{\partial t} \right) A \\ & + i \left(\gamma(\omega_0) + i \gamma_1 \frac{\partial}{\partial t} \right) \left(A(z, t) \int_0^{\infty} R(t') |A(z, t - t')|^2 dt' \right) \end{aligned} \quad (2.16)$$

where β_m is defined in Eq. 2.5, $\alpha(\omega_0)$ is the attenuation coefficient at frequency ω_0 , $\alpha_1 = \frac{d\alpha}{d\omega}$, is the slope of the attenuation coefficient evaluated at ω_0 , $\gamma(\omega_0)$ is the waveguide nonlinearity at frequency ω_0 , $\gamma_1 = \frac{d\gamma}{d\omega} \approx \frac{\gamma}{\omega_0}$, is the slope of γ evaluated at ω_0 , $R(t)$ is the nonlinear response function

given by [72]

$$R(t) = (1 - f_R)\delta(t) + f_R h_R(t) \quad (2.17)$$

where f_R is the fractional contribution of the delayed Raman response. For As_2Se_3 , $f_R=0.1$. $\delta(t)$ is the Dirac delta function and $h_R(t)$ is the Raman response function given by

$$h_R(t) = \frac{\tau_1^2 + \tau_2^2}{\tau_1\tau_2} \exp(-t/\tau_2) \sin(t/\tau_1)\Theta(t) \quad (2.18)$$

where $\tau_1=23$ fs, and $\tau_2=195$ fs for As_2Se_3 . $\Theta(t)$ is the Heaviside step function.

For pulses with pulse width >100 fs, assuming $\alpha_1=0$, $\gamma_1=\frac{\gamma}{\omega_0}$, and using the following Taylor-series expansion $|A(z, t - t')|^2 \approx |A(z, t)|^2 - t' \frac{\partial}{\partial t} |A(z, t)|^2$, the generalized nonlinear Schrödinger equation Eq. 2.16 is approximated by [72]

$$\frac{\partial A}{\partial z} = i \sum_{m \geq 2} \frac{i^m \bar{\beta}_m}{m!} \frac{\partial^m A}{\partial T^m} - \frac{\alpha}{2} A + i\gamma \left(|A|^2 A + \frac{i}{\omega_0} \frac{\partial}{\partial T} (|A|^2 A) - T_R A \frac{\partial |A|^2}{\partial T} \right) \quad (2.19)$$

where $T=t - z/v_g$, where v_g is the group velocity. The first term on the right side of Eq. 2.19 describes the effect of chromatic dispersion; The second term describes the effect of attenuation; The third term describes the Kerr effect; The fourth term describes the effect of self-steepening; the fifth term describes the Raman effect, where $T_R = \int_0^\infty t R(t) dt$.

2.4 Nonlinear effects

2.4.1 Self-phase modulation

It is well-known that the refractive index n of a nonlinear medium is intensity-dependent due to the Kerr effect. As a result, a nonlinear phase shift is introduced in the frequency domain, and is associated to a spectral broadening. A pure SPM effect is studied by neglecting dispersion, loss, self-steepening, and the Raman effect. In this situation, Eq. 2.19 leads to [59]

$$\frac{\partial A}{\partial z} = i\gamma A |A|^2 \quad (2.20)$$

The general solution is

$$A(z, T) = A(0, T) \exp[i\gamma |A(0, T)|^2 z] = A(0, T) \exp[i\phi(z, T)] \quad (2.21)$$

where $A(0, T)$ is the field amplitude at $z=0$ and $\phi(z, T)$ is given by

$$\phi(z, T) = |A(0, T)|^2 (L_{\text{eff}}/L_{\text{NL}}) \quad (2.22)$$

where L_{eff} and L_{NL} are the effective length and nonlinear length, respectively, and given by

$$L_{\text{eff}} = \frac{1 - \exp(-\alpha L)}{\alpha} \quad (2.23)$$

$$L_{\text{NL}} = (\gamma P_0)^{-1} \quad (2.24)$$

where α is the attenuation coefficient, L is the physical length, γ is the waveguide nonlinearity parameter, and P_0 is the peak power of the propagating signal.

The SPM effect induces a time-dependent phase-shift. As a result, the frequency chirp is also time-dependent and given by

$$\delta\omega(T) = -\frac{\partial\phi}{\partial T} = -\left(\frac{L_{\text{eff}}}{L_{\text{NL}}}\right) \frac{\partial}{\partial T} |A(0, T)|^2 \quad (2.25)$$

The time-dependent frequency chirp induces a red shift ($\delta\omega < 0$) near the leading edge of the pulse and a blue shift ($\delta\omega > 0$) near the trailing edge of the pulse.

2.4.2 Cross-phase modulation

When two or more optical fields propagate in a nonlinear medium simultaneously, the phase of each optical field is not only affected by its own intensity, but also affected by other optical fields' intensities. As a result, XPM effect leads to spectral broadening of optical pulses and temporal pulse shape modification under interactions with dispersion effects. This phenomena is known as XPM. Considering two optical fields propagating simultaneously, the XPM effect is modeled by coupled nonlinear Schrödinger equations

$$\frac{\partial A_1}{\partial z} + \frac{1}{v_{g1}} \frac{\partial A_1}{\partial t} + \frac{i}{2} \beta_{21} \frac{\partial^2 A_1}{\partial t^2} = i\gamma_1 (|A_1|^2 + 2|A_2|^2) A_1 \quad (2.26)$$

$$\frac{\partial A_2}{\partial z} + \frac{1}{v_{g2}} \frac{\partial A_2}{\partial t} + \frac{i}{2} \beta_{22} \frac{\partial^2 A_2}{\partial t^2} = i\gamma_2 (|A_2|^2 + 2|A_1|^2) A_2 \quad (2.27)$$

where A_1 and A_2 are the amplitudes of two optical fields. v_{g1} and v_{g2} are the group velocities of two optical fields. β_{21} and β_{22} are second order dispersion coefficients of two optical fields. γ_1

and γ_2 are the waveguide nonlinearity parameters of two optical fields. The Eqs.2.26-2.27 include XPM effect, SPM effect, second order dispersion effect and walk-off effect. Two optical fields propagate at different group velocities leading to pulses separation and limit the XPM interaction. This phenomenon is described by the walk-off length L_W defined as

$$L_W = \frac{T_0}{|d_{12}|} \quad (2.28)$$

where T_0 is the pulse width at 1/e-intensity point and d_{12} is the walk-off parameter and defined as

$$d_{12} = \frac{1}{v_g(\lambda_1)} - \frac{1}{v_g(\lambda_2)} \quad (2.29)$$

where λ_1 and λ_2 are the central wavelengths of two pulses.

2.4.3 Modulation instability

MI is a direct consequence of an interplay between the nonlinear effects and dispersive effects. If chromatic dispersion effect and Kerr effect are taken into account, the propagation equation of a light wave is given by [59, 73]

$$i \frac{\partial A}{\partial z} = \frac{\beta_2}{2} \frac{\partial^2 A}{\partial T^2} - \gamma |A|^2 A \quad (2.30)$$

this equation is the well-known nonlinear Schrödinger equation, $A(z, T)$ is the amplitude of the field envelope. The first term on the right side of Eq. 2.30 describes the chromatic dispersion effect, where β_2 is the second order chromatic dispersion coefficient. The second term on the right side of Eq. 2.30 describes the SPM effect, where γ is the waveguide nonlinearity parameter. In the case of CW propagation, the steady-state solution of Eq. 2.30 is given by

$$A = \sqrt{P_0} \exp(i\phi_{NL}) \quad (2.31)$$

where P_0 is the incident power and $\phi_{NL}=\gamma P_0 z$ is the nonlinear phase shift induced by SPM. A small perturbation is induced to verify whether the steady-state solution Eq. 2.31 is stable in presence of small perturbations. Now, the amplitude of the field envelope A is given by

$$A = (\sqrt{P_0} + a) \exp(i\phi_{NL}) \quad (2.32)$$

the evolution of the perturbation $a(z, T)$ is investigated by substituting Eq. 2.32 into Eq. 2.30 and linearizing in a

$$i \frac{\partial a}{\partial z} = \frac{\beta_2}{2} \frac{\partial^2 a}{\partial T^2} - \gamma P_0 (a + a^*) \quad (2.33)$$

The solution of this equation is given by

$$a(z, T) = a_1 \exp[i(Kz - \Omega T)] + a_2 \exp[-i(Kz - \Omega T)] \quad (2.34)$$

where K and Ω are the wave number and the frequency of perturbation, respectively. This solution is valid, subject to condition

$$K = \pm \frac{1}{2} |\beta_2 \Omega| [\Omega^2 + \text{sgn}(\beta_2) \Omega_c^2]^{\frac{1}{2}} \quad (2.35)$$

where $\text{sgn}(\beta_2) = \pm 1$ depending on the sign of β_2 , Ω_c is defined as

$$\Omega_c^2 = \frac{4\gamma P_0}{|\beta_2|} \quad (2.36)$$

when the pump wavelength is set into anomalous dispersion ($\beta_2 < 0$), the perturbation $a(z, T)$ grows exponentially with propagation distance z since K becomes imaginary for $|\Omega| < \Omega_c$. Note that MI can also occur when the pump wavelength is set into normal dispersion ($\beta_2 > 0$) given $\beta_4 < 0$. In practice, this kind of dispersion profile is easily realized in tapered ChG microwires. In a microwire with positive second order chromatic dispersion ($\beta_2 > 0$) and negative fourth order chromatic dispersion ($\beta_4 < 0$), the frequency shift Ω_s between pump and Stokes/anti-Stokes waves is

$$\Omega_s^2 = \frac{6}{|\beta_4|} (\sqrt{\beta_2^2 + 2|\beta_4|\gamma P_0/3} + \beta_2) \quad (2.37)$$

2.4.4 Four-wave mixing

FWM is an important nonlinear effect to achieve wavelength converter, SC generation, and OPOs. FWM are classified as degenerate and non-degenerate FWM depending on the number of pumps. Figure 2.2 shows an energy diagram representing the energy exchange in degenerate and non-degenerate FWM. For degenerate FWM, a single pump with angular frequency ω_1 and a signal with angular frequency ω_3 are launched into a microwire. When the phase-matching condition is satisfied, an idler with angular frequency ω_4 is generated under the condition $2\omega_1 = \omega_3 + \omega_4$. For non-degenerate FWM, two pumps with angular frequencies ω_1 and ω_2 , respectively, combined with a

signal with angular frequency ω_3 are launched into a microwire. When the phase-matching condition is satisfied, an idler with angular frequency ω_4 is generated under the condition $\omega_1 + \omega_2 = \omega_3 + \omega_4$.

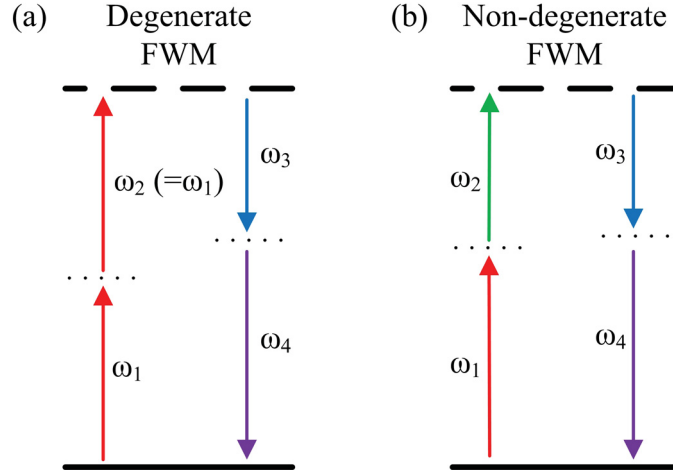


Fig. 2.2 Schematic of degenerate FWM and non-degenerate FWM.

Coupled amplitude equations

In the case of non-degenerate FWM, the evolution of the amplitude $A_j(z)$ inside an optical fiber is governed by four coupled equations [59]

$$\frac{dA_1}{dz} = \frac{in_2\omega_1}{c} \left[\left(f_{11}|A_1|^2 + 2 \sum_{k \neq 1} f_{1k}|A_k|^2 \right) A_1 + 2f_{1234}A_2^*A_3A_4e^{i\Delta kz} \right] - \frac{1}{2}\alpha_1A_1 \quad (2.38)$$

$$\frac{dA_2}{dz} = \frac{in_2\omega_2}{c} \left[\left(f_{22}|A_2|^2 + 2 \sum_{k \neq 2} f_{2k}|A_k|^2 \right) A_2 + 2f_{2134}A_1^*A_3A_4e^{i\Delta kz} \right] - \frac{1}{2}\alpha_2A_2 \quad (2.39)$$

$$\frac{dA_3}{dz} = \frac{in_2\omega_3}{c} \left[\left(f_{33}|A_3|^2 + 2 \sum_{k \neq 3} f_{3k}|A_k|^2 \right) A_3 + 2f_{3412}A_1A_2A_4^*e^{-i\Delta kz} \right] - \frac{1}{2}\alpha_3A_3 \quad (2.40)$$

$$\frac{dA_4}{dz} = \frac{in_2\omega_4}{c} \left[\left(f_{44}|A_4|^2 + 2 \sum_{k \neq 4} f_{4k}|A_k|^2 \right) A_4 + 2f_{4312}A_1A_2A_3^*e^{-i\Delta kz} \right] - \frac{1}{2}\alpha_4A_4 \quad (2.41)$$

where the wave-vector mismatch Δk is given by

$$\Delta k = \beta_3 + \beta_4 - \beta_1 - \beta_2 = (n_3\omega_3 + n_4\omega_4 - n_1\omega_1 - n_2\omega_2)/c \quad (2.42)$$

β_j is the propagation constant at the frequency ω_j and n_j is the effective refractive index at the frequency ω_j . The overlap integral f_{jk} is defined as

$$f_{jk} = \frac{\iint_{-\infty}^{\infty} |F_j(x, y)|^2 |F_k(x, y)|^2 dx dy}{(\iint_{-\infty}^{\infty} |F_j(x, y)|^2 dx dy)(\iint_{-\infty}^{\infty} |F_k(x, y)|^2 dx dy)} \quad (2.43)$$

The overlap integral f_{ijkl} is given by

$$f_{ijkl} = \frac{\langle F_i^* F_j^* F_k F_l \rangle}{[\langle |F_i|^2 \rangle \langle |F_j|^2 \rangle \langle |F_k|^2 \rangle \langle |F_l|^2 \rangle]^{\frac{1}{2}}} \quad (2.44)$$

where angle brackets denote integration over the transverse coordinates x and y . A numerical method is necessary to exactly solve the set of coupled equations since they include attenuation, SPM, XPM, and pump depletion effects.

Approximate solution

Assuming the pump is much more intense than the signal and idler during the FWM process, the pump is considered as an undepleted pump. All overlap integrals are nearly the same $f_{ijkl} \approx f_{ij} \approx 1/A_{\text{eff}}$ ($i, j, k, l = 1, 2, 3, 4$) given the frequency differences of the involved four waves are negligible, and all waveguide nonlinearity parameter are the same, $\gamma_j = n_2 \omega_j / (c A_{\text{eff}}) \approx \gamma$, Eqs. 2.38-2.41 for non-degenerate FWM are simplified as [59]

$$\frac{dA_1}{dz} = i\gamma [(|A_1|^2 + 2(|A_2|^2 + |A_3|^2 + |A_4|^2)) A_1 + 2A_2^* A_3 A_4 e^{i\Delta k z}] - \frac{1}{2} \alpha_1 A_1 \quad (2.45)$$

$$\frac{dA_2}{dz} = i\gamma [(|A_2|^2 + 2(|A_1|^2 + |A_3|^2 + |A_4|^2)) A_2 + 2A_1^* A_3 A_4 e^{i\Delta k z}] - \frac{1}{2} \alpha_2 A_2 \quad (2.46)$$

$$\frac{dA_3}{dz} = i\gamma [(|A_3|^2 + 2(|A_1|^2 + |A_2|^2 + |A_4|^2)) A_3 + 2A_4^* A_1 A_2 e^{-i\Delta k z}] - \frac{1}{2} \alpha_3 A_3 \quad (2.47)$$

$$\frac{dA_4}{dz} = i\gamma [(|A_4|^2 + 2(|A_1|^2 + |A_2|^2 + |A_3|^2)) A_4 + 2A_3^* A_1 A_2 e^{-i\Delta k z}] - \frac{1}{2} \alpha_4 A_4 \quad (2.48)$$

The procedures to solve the above set of coupled equations have been well described in [59]. The general solution is described as [59]

$$B_3(z) = A_3 \exp[-2i\gamma(P_1 + P_2)z] = (a_3 e^{gz} + b_3 e^{-gz}) \exp(-i\kappa z/2) \quad (2.49)$$

$$B_4^*(z) = A_4 \exp[2i\gamma(P_1 + P_2)z] = (a_4 e^{gz} + b_4 e^{-gz}) \exp(i\kappa z/2) \quad (2.50)$$

where a_3, b_3, a_4, b_4 are coefficients determined from boundary conditions, P_1 and P_2 are the incident pump powers at $z = 0$. The effective phase mismatch κ and parametric gain g are defined as

$$\kappa = \Delta k + \gamma(P_1 + P_2) \quad (2.51)$$

$$g = \sqrt{(\gamma P_0 r)^2 - (\kappa/2)^2} \quad (2.52)$$

where the parameter r and P_0 are defined as

$$r = 2(P_1 P_2)^{1/2}/P_0, P_0 = P_1 + P_2 \quad (2.53)$$

The signal power $P_3(z)$ takes the form

$$P_3(z) = P_3(0)[1 + (1 + \kappa^2/4g^2)\sinh^2(gz)] \quad (2.54)$$

The idler power $P_4(z)$ takes the form

$$P_4(z) = P_3(0)(1 + \kappa^2/4g^2)\sinh^2(gz) \quad (2.55)$$

The amplification factor is defined as output signal power over input signal power

$$G_s = P_3(L)/P_3(0) = 1 + (\gamma P_0 r/g)^2 \sinh^2(gL) \quad (2.56)$$

When $\kappa \gg \gamma P_0 r$, the gain expression Eq. 2.56 is described as

$$G_s \approx 1 + (\gamma P_0 r L)^2 \frac{\sin^2(\kappa L/2)}{(\kappa L/2)^2} \quad (2.57)$$

As shown in Eq. 2.57, the amplification factor has a quadratic dependence with the pump power P_0 . When phase matching is perfect ($\kappa=0$) and $gL \gg 1$, the gain expression Eq. 2.56 is described as

$$G_s \approx \frac{1}{4} \exp(2\gamma P_0 r L) \quad (2.58)$$

As shown in Eq. 2.58, the amplification factor has an exponential relationship with the pump power P_0 .

2.4.5 Raman effect

The Raman effect is one of the important nonlinear phenomena which arises from the interaction of an intense light beam with the vibrational modes of molecules composing a material. Figure 2.3 shows the schematic of stimulated Raman scattering process from a quantum-mechanical viewpoint. In this scattering process, a photon with energy $h\omega_p$ is scattered to result into a red shifted photon of energy $h\omega_s$ plus an optical phonon. The energy of the phonon equals the difference in energy between the pump and scattered photons, and is representative of the material.

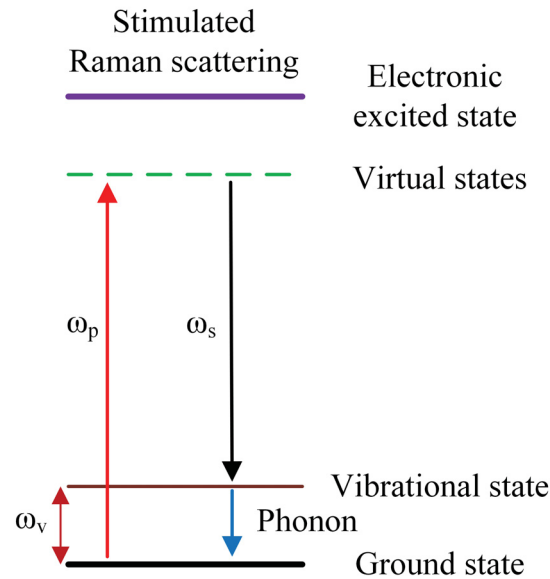


Fig. 2.3 Schematic of stimulated Raman scattering from a quantum-mechanical viewpoint.

Figure 2.4 shows the measured Raman gain spectrum of As_2Se_3 [74]. The Raman gain bandwidth of As_2Se_3 is $\sim 60 \text{ cm}^{-1}$. The Raman shift of As_2Se_3 is $\sim 240 \text{ cm}^{-1}$.

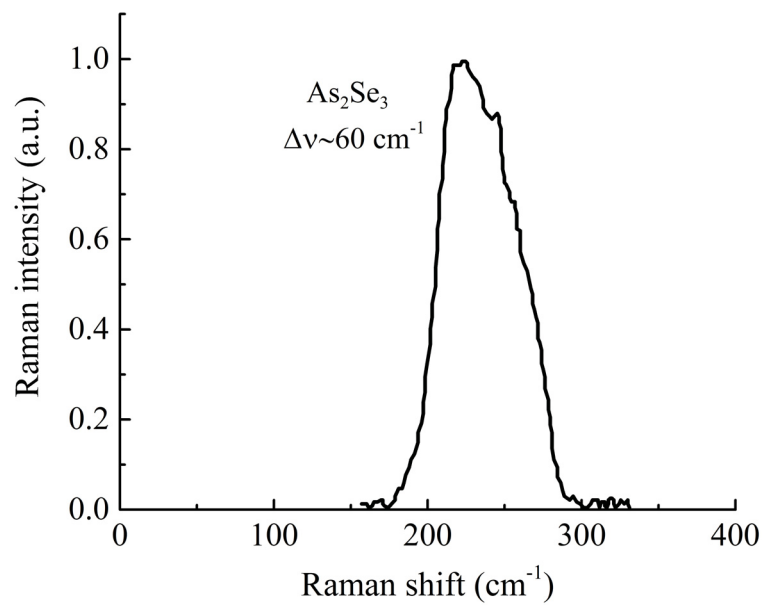


Fig. 2.4 The measured Raman gain spectrum of As_2Se_3 .

Chapter 3

Design, fabrication and characterization of PC-, COP- and PMMA-cladded ChG microwires

3.1 Introduction

The wavelength range of 2 μm is of broad interest for several applications including LIDAR, gas sensing systems, free-space communications and medical applications [75, 76]. Semiconductor lasers and Thulium-doped fibers provide gain in the wavelength range of 2 μm , thus providing access to compact laser sources [77–81]. The operation of a 2 μm laser depends on the availability of a variety of components compatible with this wavelength range. Of most importance, a nonlinear medium enables the laser to be operated in a pulsed regime [82, 83]. A nonlinear medium could also be used for wavelength conversion [84–86].

Compact and highly nonlinear media compatible with the wavelength range of 2 μm include high modal confinement waveguides such as optical fiber microwires and photonic crystal fibers [6, 87]. The large intrinsic nonlinearity (n_2) and transparency are the two most important properties that a material must have to serve as a compact nonlinear medium. ChG glasses are excellent candidates to play this role because their n_2 is up to a factor of 1000 times larger than for the widespread silica glass [1]. Moreover, the transparency spectrum of ChG glasses is ideal for applications over a broad wavelength range: Arsenic selenide (As_2Se_3) transmits light from 1 to 12 μm [2], and Arsenic sulfide (As_2S_3) transmits light from 1 to 8 μm [3]. ChG glasses also have

negligible two-photon absorption and free carrier absorption in the 2 μm wavelength range [4, 5].

In its simplest form, the waveguide structure of the ChG microwire consists of a ChG core surrounded by a cladding of ambient air [13]. With a wire diameter in the order of the wavelength, the air-cladding ChG microwire unfortunately has a limited usefulness because of its extreme mechanical fragility and quick degradation when exposed to dust of a non-controlled environment. In order to overcome these limitations, Baker et al. have successfully fabricated the first polymer-cladded ChG microwire [7, 19], which consists of a ChG microwire cladded with PMMA [19]. The PMMA cladding provides mechanical strength to the ChG microwire and protects it from environmental contamination and degradation. Being now a practical component, the hybrid PMMA/ChG microwire has been used for several applications at telecommunication wavelengths: Optical amplification and laser oscillation based on Raman and parametric gains [20–22], wavelength conversion [23], SC generation [25], they have served as nonlinear engines in a self-pulsating fiber laser cavity [30] and served to reduce and control stimulated Brillouin scattering [28]. For quantum cryptography, the hybrid ChG microwires have been used to convert one photon into two [26], as well as producing photon pairs with unprecedented efficiency [27].

Despite the many successful demonstrations of the PMMA/ChG microwire, the limited transparency of PMMA at wavelengths beyond 1.55 μm attenuates the propagating signal. This attenuation comes from the evanescent part of the guided mode in a PMMA-cladded ChG microwire, and is characteristic of microwires of several centimeters long.

In this chapter, we investigate the use of alternative polymers to clad the As_2Se_3 microwire with a goal to operate them in the 1.85 μm to 2.20 μm wavelength range. The cladding compositions under study include PC, COP 480R, COP 1020R, and PMMA as the reference polymer.

3.2 The polymer cladding

Polymers can be classified based on their molecular structure difference as amorphous and crystalline polymers. The molecular structure of an amorphous polymer is randomly ordered, resulting in gradual softening with increasing temperature. In contrast, the molecular structure of a crystalline polymer is highly ordered leading to a sharp state transition, from solid to liquid, with increasing temperature. Table 3.1 lists a few physical parameters of amorphous and crystalline C-H based polymers, including PMMA, PC, COP 480R, Cyclic Olefin Copolymer (COC), Polysulfone (PSU), Polyetherimide (PEI), Polyethersulfone (PES), Polyimide (PI), Polyethylene terephthalate (PET), and Polyethylene (PE). The physical properties include the classification of amorphous

(Amor.) and crystalline (Cryst.) state, melting temperature T_m ($^{\circ}\text{C}$), glass transition temperature T_g ($^{\circ}\text{C}$), refractive index n at $1.55\ \mu\text{m}$, and transmission T at $\lambda > 1.7\ \mu\text{m}$.

Table 3.1 Common C-H based polymers and their physical parameters

Name	Type	T_m ($^{\circ}\text{C}$)	T_g ($^{\circ}\text{C}$)	n	T ($\lambda > 1.7\ \mu\text{m}$)
PMMA	Amor.	160 [88]	105 [89]	1.48 [90]	Medium up to $2.1\ \mu\text{m}$ [91]
PC	Amor.	265 [92]	147 [93]	1.53 [94]	Good up to $2.1\ \mu\text{m}$ [95]
COP E48R	Amor.	275 [96]	138 [97]	1.51 [98]	Good up to $2.3\ \mu\text{m}$ [95]
COC	Amor.	Not observed [99]	136 [100]	1.52 [101]	Medium up to $2.2\ \mu\text{m}$ [102]
PSU	Amor.	310-390 [103]	185 [104]	1.60 [105]	Medium up to $2.1\ \mu\text{m}$ [106]
PEI	Amor.	380 [107]	218 [108]	1.66 [94]	Medium up to $2.1\ \mu\text{m}$ [95]
PES	Amor.	350 [109]	220 [104]	1.61 [94]	Medium up to $2.1\ \mu\text{m}$ [106]
PI	Amor.	Not observed [110]	>300 [111]	1.76 [112]	Medium up to $2.1\ \mu\text{m}$ [112]
PET	Cryst.	260 [113]	74.5 [114]	1.55 [115]	No good [116]
PE	Cryst.	117 [117]	-125 [118]	1.49 [119]	No good [120]

Amorphous polymers, instead of crystalline polymers, should be selected as the cladding materials since ChG materials are amorphous. Crystalline polymers are not compatible with ChG materials due to the large scattering loss compared with that of amorphous polymers. All of those polymers shown in table 3.1 have been considered to serve as claddings to ChG microwires, taking into account the physical properties listed in table 3.1, PC and COP are selected and investigated in this study since they are amorphous, have a compatible glass transition temperature (T_g) with As_2Se_3 material, and have a good transmittance.

3.2.1 Chemical structure

Polymers are composed of different chemical bonds. Figure 3.1 shows the chemical structure of COP, PC and PMMA. COP is composed of C-H bonds and carbon-carbon (C-C) bonds [121, 122]. PC and PMMA are composed of C-H bonds, carbon-oxygen (C-O) single bonds, carbon-oxygen (C=O) double bonds and C-C bonds [123, 124].

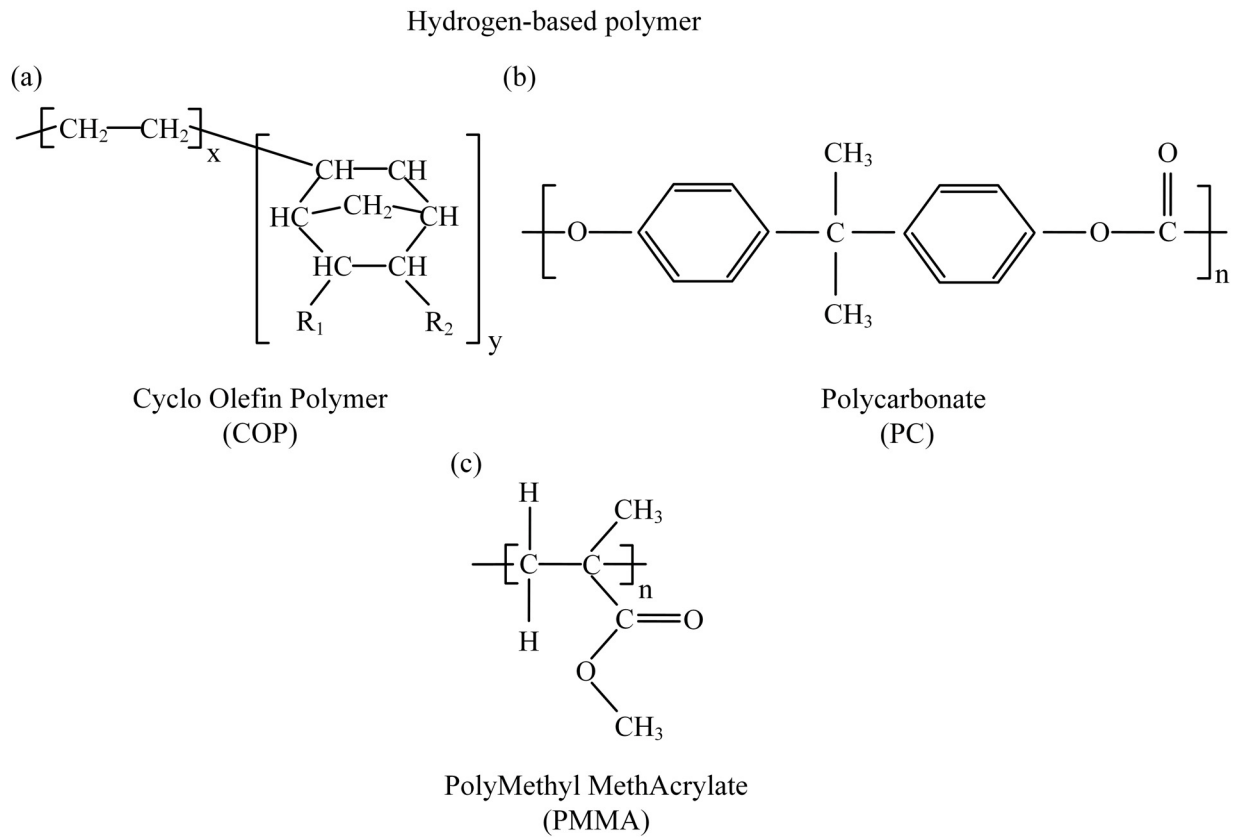


Fig. 3.1 Chemical structure of COP, PC and PMMA.

3.2.2 Absorption of polymer

The optical losses caused by a polymer cladding come from two parts: intrinsic and extrinsic losses. Figure 3.2 summarizes the intrinsic and extrinsic loss factors in polymer. The intrinsic losses include absorption and scattering. The intrinsic absorption mechanisms include fundamental vibration and its overtones and electronic transitions. Vibrational overtones are due to the stretching and bending of chemical bonds such as C-H bonds and typically present as absorption peaks at wavelengths $> 0.8 \mu\text{m}$. On the other hand, electronic transition absorption is due to the presence of conjugated double bonds and typically present at wavelengths $< 0.8 \mu\text{m}$. The intrinsic scattering mechanism, Rayleigh scattering, occurs when the light transmitting inside the ChG core interacts with the atoms inside the polymer cladding. Rayleigh scattering results from the electric polarizability of particles.

Extrinsic losses include absorption and scattering. Extrinsic absorption in the polymer is due

to the impurities of the polymer, such as water and organic contaminants. The extrinsic scattering losses arise from a number of sources, including dusts, micro-voids, micro-cracks, delamination and core-cladding interface roughness. These imperfections are developed during the fabrication of polymer-cladded ChG preform, hybrid fiber and microwire. As a result, the transmission losses could be significantly increased by light scattering.

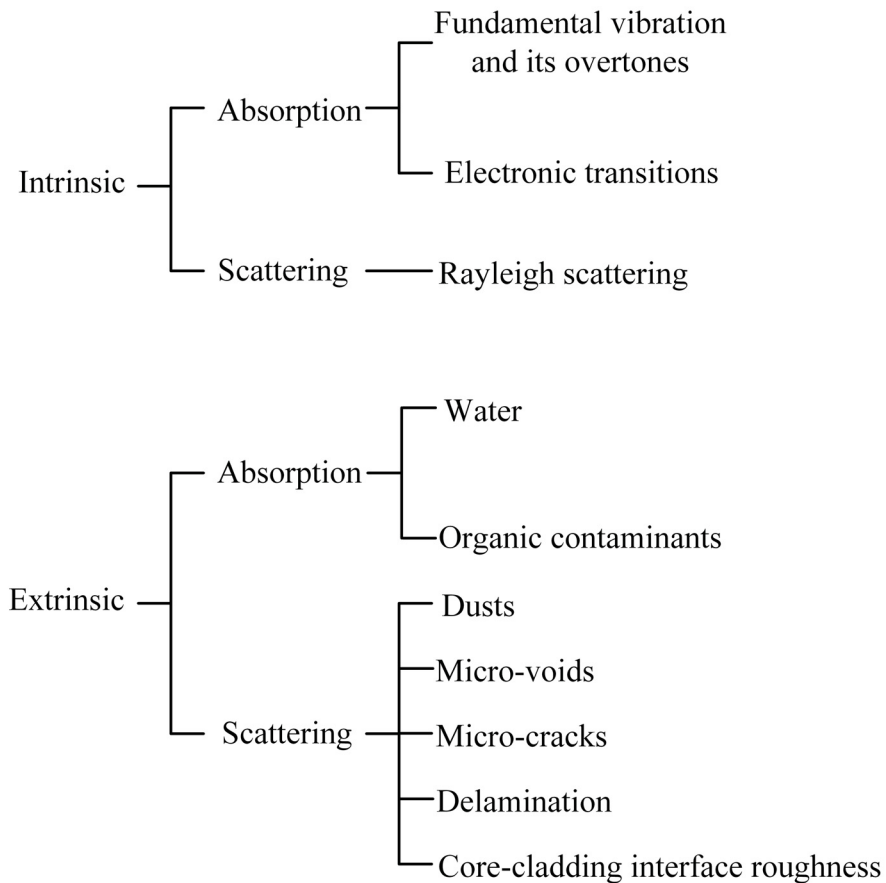


Fig. 3.2 Loss mechanisms.

Fundamental vibration and its overtones

The transmission losses of the polymer arise from intrinsic and extrinsic mechanisms. The intrinsic mechanisms of the transmission losses at target wavelengths ($>1.5 \mu\text{m}$) is mainly vibrational transitions [125]. Vibrational transitions are typically present as absorption peaks caused by stretching and bending of chemical bonds. The resonant frequencies of these vibrational transitions are largely determined by the force constant and the reduced mass of the two nuclei. The fundamental vibrational frequency is modeled with the following equation [126]

$$v = \frac{1}{2\pi c} \sqrt{\frac{k}{\mu}} \quad (3.1)$$

where v is the fundamental vibrational frequency in cm^{-1} , k is the force constant, μ is the reduced mass. The reduced mass is given by

$$\mu = \frac{m_1 m_2}{m_1 + m_2} \quad (3.2)$$

where m_1 and m_2 are the component masses for the chemical bond under consideration.

The n th order vibrational frequency can be calculated by [127]

$$f_n = \frac{v_1 n - v_1 \chi n(n+1)}{1 - 2\chi} \quad (3.3)$$

where f_n is the n th order vibrational frequency. v_1 is the fundamental vibration frequency, χ is the anharmonicity constant.

The molecular vibrational absorption loss α_{mv} due to the overtone vibration of C-H bonds is described by [127]

$$\alpha_{mv} = 3.2 \times 10^8 \frac{\rho}{M} N^{\text{CH}} \left(\frac{E_v^{\text{CH}}}{E_1^{\text{CH}}} \right) \quad (3.4)$$

where ρ is the density, M is the molecular weight of the monomer, N^{CH} is the number of C-H bonds in monomer unit, v is the vibrational quantum number, $E_v^{\text{CH}}/E_1^{\text{CH}}$ is the energy ratio of the v th order vibrational overtone of a C-H bond to the fundamental vibration of a C-H bond [127]. Figure 3.3 shows the calculated absorption loss due to the fundamental vibration and its overtones of a C-H bond.

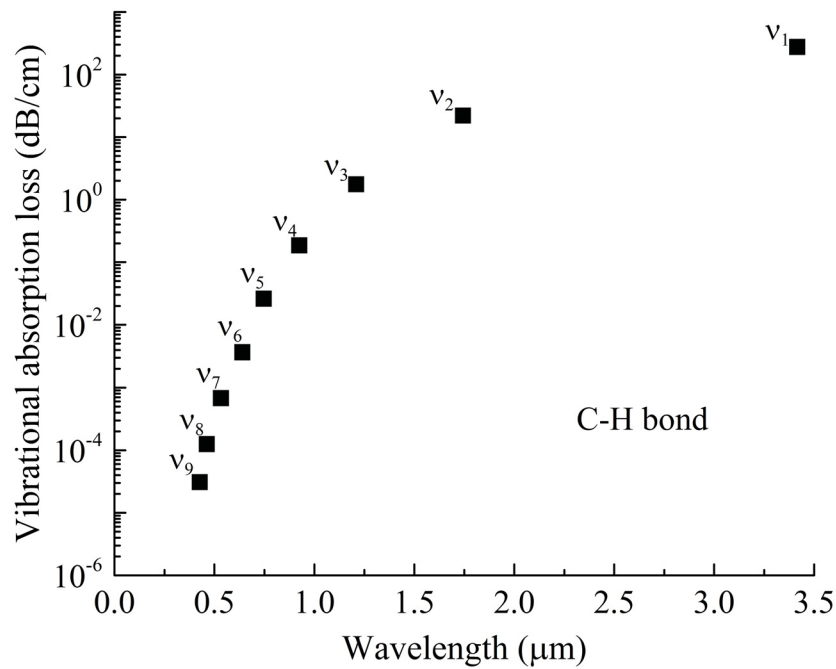


Fig. 3.3 Calculated absorption of fundamental vibration and its overtones of a C-H bond.

Table 3.2 summarizes the first order and second order vibrational wavelengths of C-H bonds, C=O bonds, C-C bonds and C-O bonds. The transparency in the short MIR wavelengths of a hydrogen-based polymer is influenced by the presence of C-H bonds. Vibrational wavelengths of a C-H bond are 3.4 μm (1st order) and 1.7 μm (2nd order) [125]. Vibrational wavelengths of a C=O bond are 5.4 μm (1st order) and 2.7 μm (2nd order) [128]. The vibrational wavelengths of C-C and C-O bonds occur at 8.9 μm (1st order) and 9.1 μm (1st order) [128], respectively, and thus the lowest vibrational wavelength is determined by the presence of C-H bonds.

Table 3.2 Vibrational wavelengths of different chemical bonds

Bond	1 st order vibrational wavelength (μm)	2 nd order vibrational wavelength (μm)
C-H	3.4	1.7
C-C	8.9	-
C-O	9.1	-
C=O	5.4	2.7

3.3 Hybrid microwires fabrication

Several factors must be considered in the design and fabrication of hybrid microwires to ensure that the As_2Se_3 glass and the polymer cladding are, as much as possible, compatible optically and mechanically. These factors include: (1) the transmission wavelength range of the cladding material; (2) the refractive index of the cladding material, as shown in Table 3.3; (3) the glass transition temperature (T_g) of As_2Se_3 glass and polymer, as shown in Table 3.3; and (4) the temperature-dependent viscosity of As_2Se_3 glass and polymer. Figure 3.4 shows the logarithmic plot of viscosity of As_2Se_3 [129–131], PC [132, 133], COP [134] and PMMA [135, 136] at different temperatures. For a hybrid microwire to operate at wavelengths beyond $1.85 \mu\text{m}$, the chosen cladding material must be relatively low-loss at the target transmission wavelength. The refractive index of the cladding material should also be as low as possible, below the refractive index of As_2Se_3 , to ensure the optical mode is strongly confined in the As_2Se_3 material, and thus limiting the penetration depth of the evanescent wave in the polymer. Mechanically, the As_2Se_3 and cladding material must be compatible by sharing close values of T_g , as shown in Table 3.3, and viscosity, as shown in Fig. 3.4, to ensure they can be heated and stretched together from a hybrid preform, to a hybrid fiber, and finally to a hybrid microwire [19].

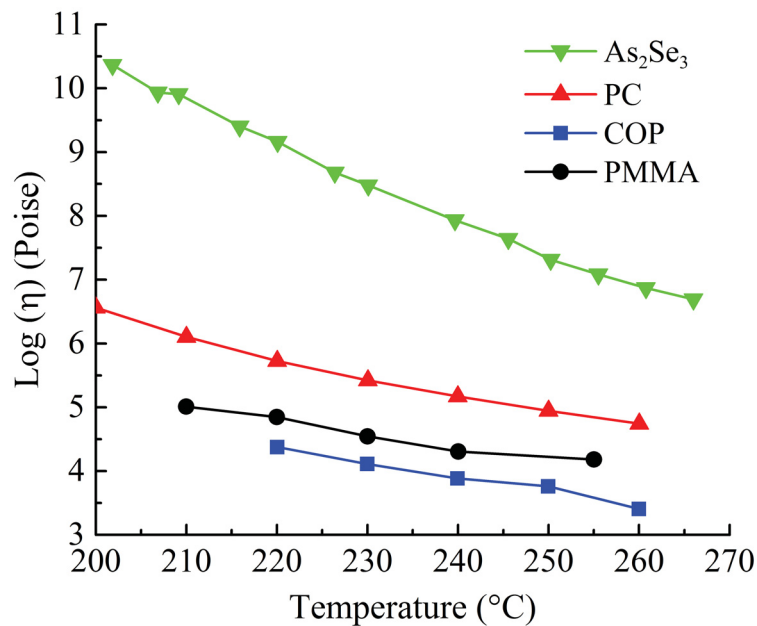


Fig. 3.4 Logarithmic plot of viscosity of As_2Se_3 , PC, COP and PMMA at different temperatures.

Table 3.3 Glass transition temperature and refractive index at 1.94 μm of ChG and polymers

	Glass transition temperature T_g ($^{\circ}\text{C}$)	Calculated refractive index
As_2Se_3	167 [2]	2.81
PMMA	105 [137]	1.47
PC	150 [138]	1.56
COP 480R	138 [139]	1.51
COP 1020R	105 [140]	1.49

3.3.1 Polymer preparation

Drying polymer is a necessary step to successfully fabricate the polymer-cladded ChG preform. Hygroscopic polymers, such as PMMA and PC, absorb water from the surrounding atmosphere. The water molecule will be attached to the polymer chain. COP has extremely low moisture absorption rate ($<0.01\%$ for 24 hours) due to its symmetric molecular structure [141]. However, the moisture will be attached to the surface of COP. Those absorbed water molecules will become bubbles when the polymer is heated up during the fabrication of polymer-cladded ChG preform. To overcome this limitation, the polymers must be dried. Figure 3.5(a) shows the vacuum oven (Across International L.L.C., Model: VO-16020) used for drying the polymer. Figure 3.5(b) and (c) show the preform without bubbles fabricated using dried polymer and the preform with bubbles fabricated using a polymer without drying. Two factors must be taken into account during the polymer drying process: (1) drying temperature and (2) drying time. The drying temperature should be slightly lower than the glass transition temperature of a polymer to ensure that the polymer is well heated, as well as it is not heat-softened. The drying time should be long enough to ensure that the polymer is completely dried and no bubbles appear during the preform fabrication process. Table 3.4 shows the drying temperature and drying time of PMMA, PC, COP 480R, and COP 1020R tubes with an inner diameter of 250 μm and an outer diameter of 600 μm . PMMA, PC, COP 480R, and COP 1020R are dried using the vacuum oven shown in Fig. 3.5(a) at a temperature of 95 $^{\circ}\text{C}$, 120 $^{\circ}\text{C}$, 105 $^{\circ}\text{C}$, 95 $^{\circ}\text{C}$, respectively, for >24 hours.

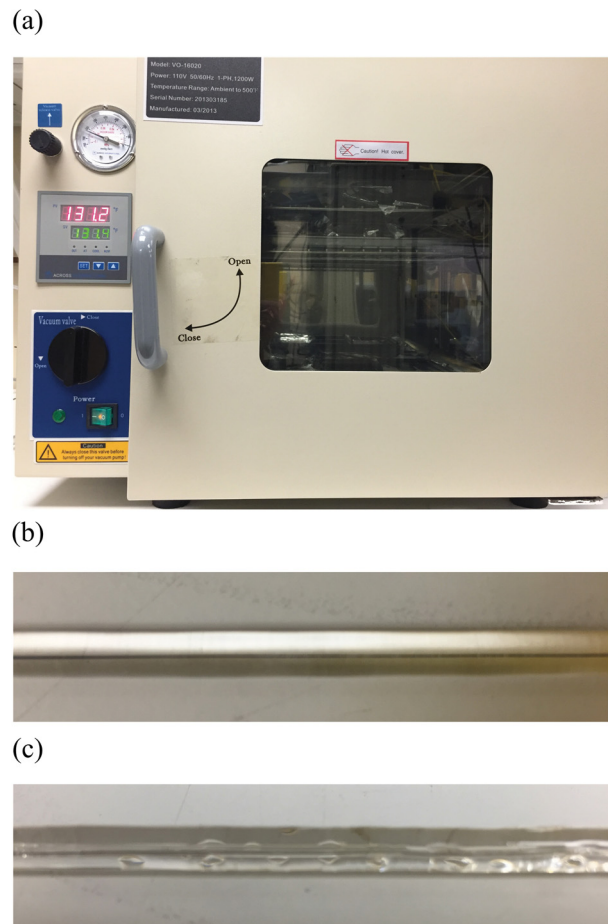


Fig. 3.5 (a) Vacuum oven used to dry polymer and ChG. (b) Preform without bubble. (c) Preform with bubbles.

Table 3.4 Drying temperature and drying time of different polymers

	Drying temperature ($^{\circ}\text{C}$)	Drying time (h)
PMMA	~ 95	> 24
PC	~ 120	> 24
COP 480R	~ 105	> 24
COP 1020R	~ 95	> 24

3.3.2 Microwires fabrication

PC and COP are good candidates to replace PMMA because they provide an improved optical transmission beyond $1.85 \mu\text{m}$ with respect to PMMA, as well as being mechanically compatible with As_2Se_3 . Figure 3.6(a) shows a schematic of the rod-in-tube method used to fabricate polymer-cladded As_2Se_3 hybrid preform [142]. It consists of a three-layer structure leading to a waveguide with an As_2Se_3 core, a polymer (PC, COP, or PMMA) cladding, and a PMMA coating. The microwire fabrication is performed in multiple steps. The first step consists in making a hybrid preform, then the hybrid preform is stretched into a hybrid fiber, and finally the hybrid fiber is stretched into a microwire.

Preform and fiber fabrication

Figure 3.6(a) shows a schematic of the hybrid preform fabrication setup. A cylinder of bulk As_2Se_3 is inserted into a PC or COP capillary tube, and the assembly is inserted into a PMMA tube. The assembly is pushed at a constant feed velocity V_f into a heated funnel. Under heat and pressure, the PMMA tube and the polymer capillary tube collapse together on the As_2Se_3 cylinder in an air-free composite cylinder. The multimaterial composite is extruded at the bottom of the funnel and drawn at a constant speed V_d to obtain a hybrid preform with a uniform diameter. Figure 3.6(b) shows the photograph of an extruded preform.

Figure 3.6(c) shows a schematic of the hybrid fiber fabrication setup. In a second step, the hybrid preform is heated and stretched to reduce further its diameter down to obtain a hybrid fiber with an As_2Se_3 core diameter $\phi_{\text{As}_2\text{Se}_3}$, leading to maximum coupling efficiency with e.g. SMF-28 fiber. Figure 3.6(d) shows the optical micrograph of a hybrid fiber.

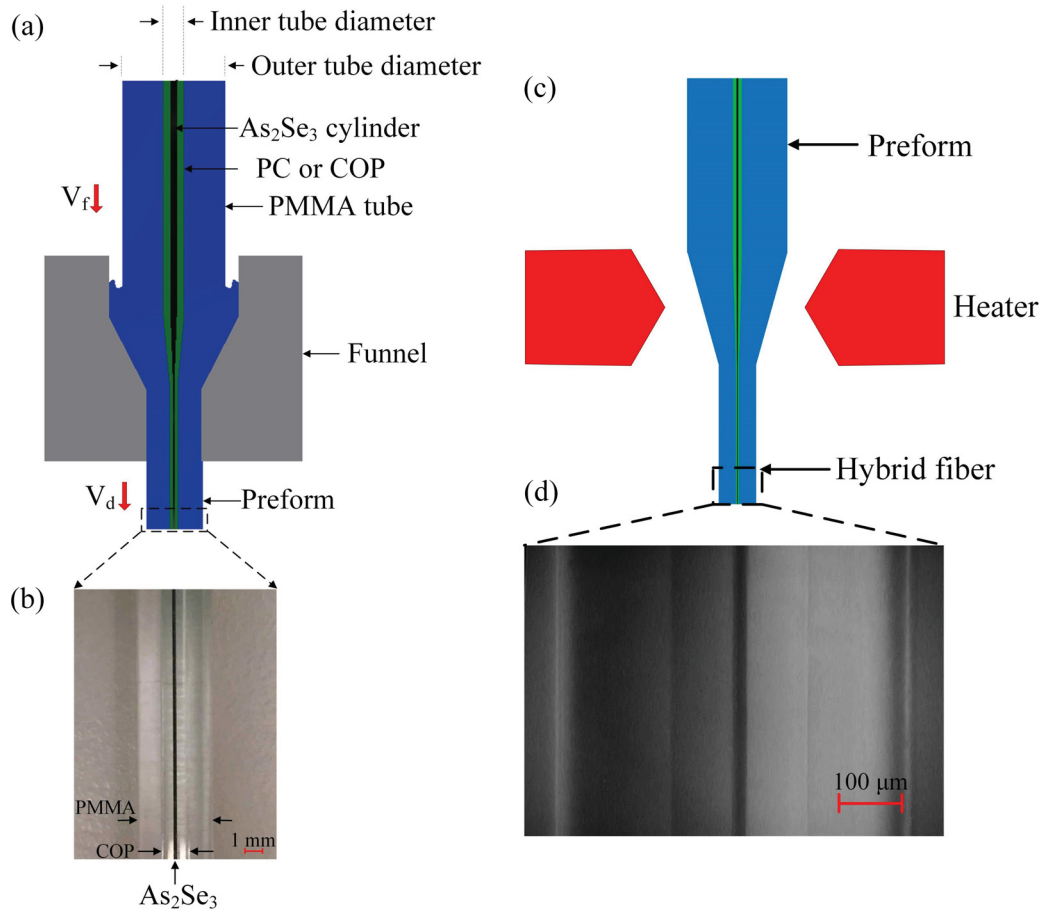


Fig. 3.6 (a) Schematic of the polymer-cladded As₂Se₃ preform fabrication setup. (b) Photograph of an extruded preform. (c) Schematic of a hybrid fiber fabrication setup. (d) Reflection optical micrograph of a hybrid fiber.

Polishing Process

Figure 3.7 shows the polishing setup. A segment of uniform hybrid fiber is cut-off and both ends are polished. Figure 3.8(a) and (b) show the reflection optical micrograph of cross section of a hybrid fiber with diameter $\phi_{\text{PMMA}}=770.0 \mu\text{m}$ and As₂Se₃-COP core-cladding with diameter $\phi_{\text{AsSe}}=18.2 \mu\text{m}$ and $\phi_{\text{COP}}=190.2 \mu\text{m}$. The hybrid fiber is designed to be optically compatible with the waveguide that it interfaces e.g. SMF-28, therefore minimizing the insertion and extraction coupling losses.

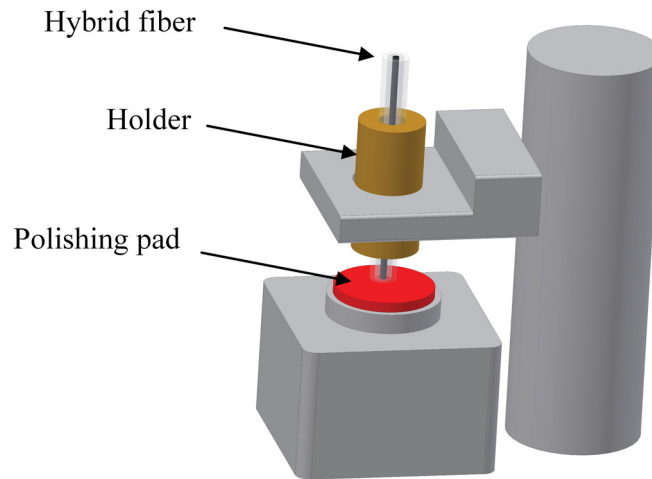


Fig. 3.7 Polishing setup.

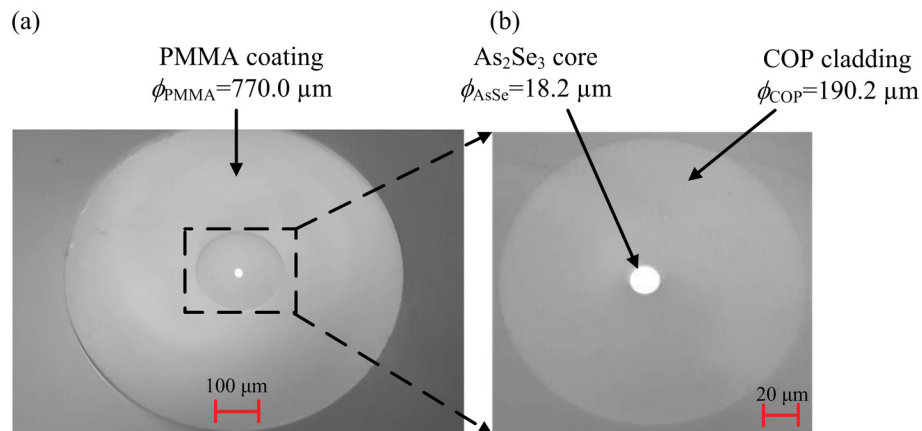


Fig. 3.8 (a) Reflection optical micrograph of cross section of a hybrid fiber. (b) Reflection optical micrograph of the As_2Se_3 -COP core-cladding.

Microwire fabrication

The hybrid microwire is fabricated from heating and stretching a sample of the hybrid fiber based on a heat-brush technique [19]. Figure 3.9(a) shows a schematic of polymer-cladded As_2Se_3 microtaper fabrication setup. Both ends of a piece of hybrid fiber are fixed and pulled towards opposite direction by two translation stages while a resistant heater placed in another translation stage is used to heat the hybrid fiber. The versatile platform can be used for fabricating microtapers,

couplers and combiners. Figure 3.9(b) shows the various sections of a microtaper. The microwire is the thin central section of the microtaper. Figure 3.9(c) shows the photograph of a microtaper with microwire section length of 10 cm.

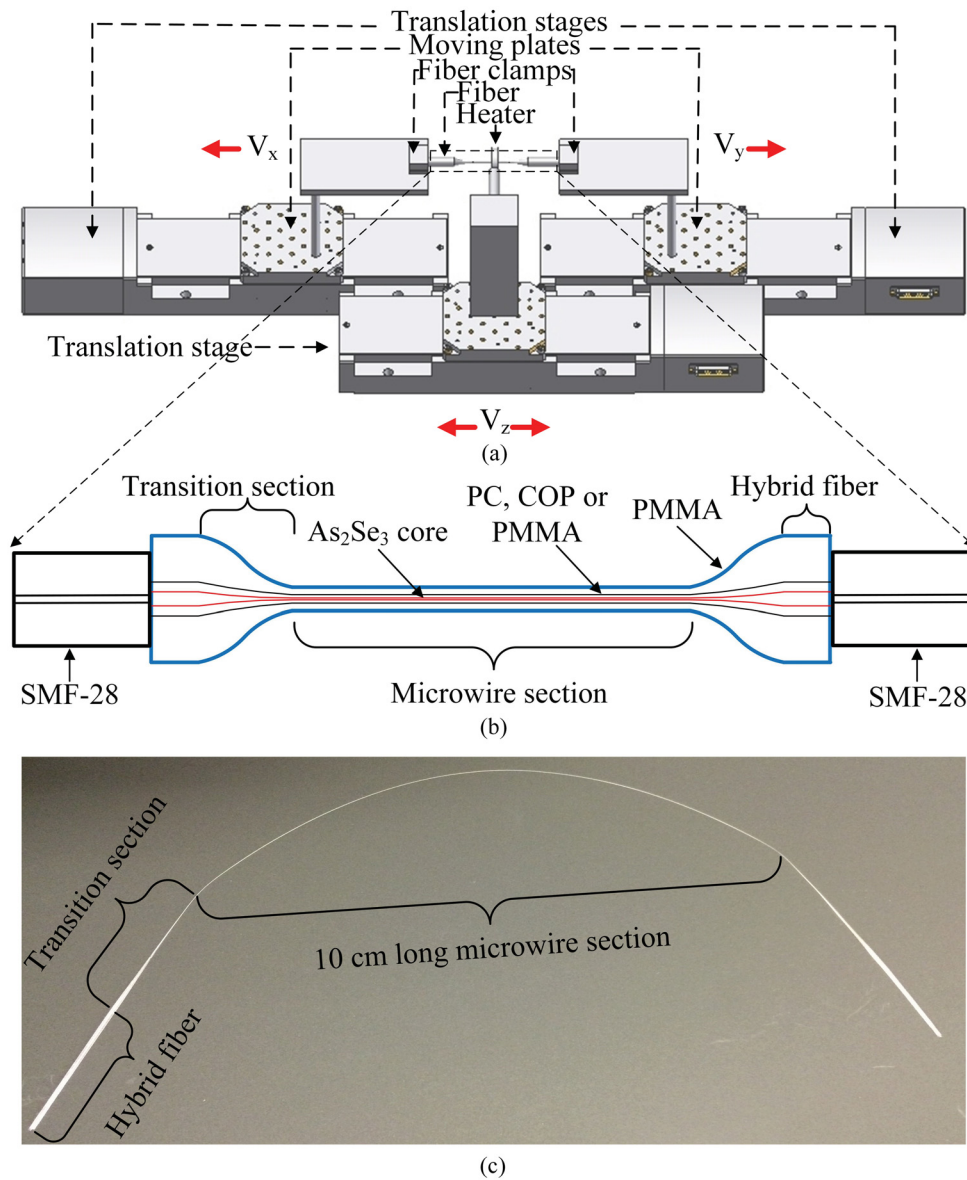


Fig. 3.9 (a) Schematic of the polymer-cladded As_2Se_3 microtaper fabrication setup. The microwire is the thin central section of the microtaper. (b) Schematic of the polymer-cladded As_2Se_3 microtaper coupled to SMF-28 fiber. (c) Photograph of a microtaper.

Coupling process

The robust microwire is manually removed from the tapering setup and transferred to a coupling setup; Figure 3.10 shows the coupling setup. The coupling process is performed in two steps. The first step is using a translation stage (Luminos I5000) to align the input SMF-28 fiber to the input end of a microtaper. Figure 3.10(a) shows the setup used to align the input SMF-28 fiber and the input end of a microtaper. The second step is aligning the output end of a microtaper to receiving SMF-28 fiber. Figure 3.10(b) shows the setup used to align the output end of a microtaper and receiving SMF-28 fiber. Then, both ends of a microtaper are permanently butt-coupled to SMF-28 fibers using UV-cured epoxy.

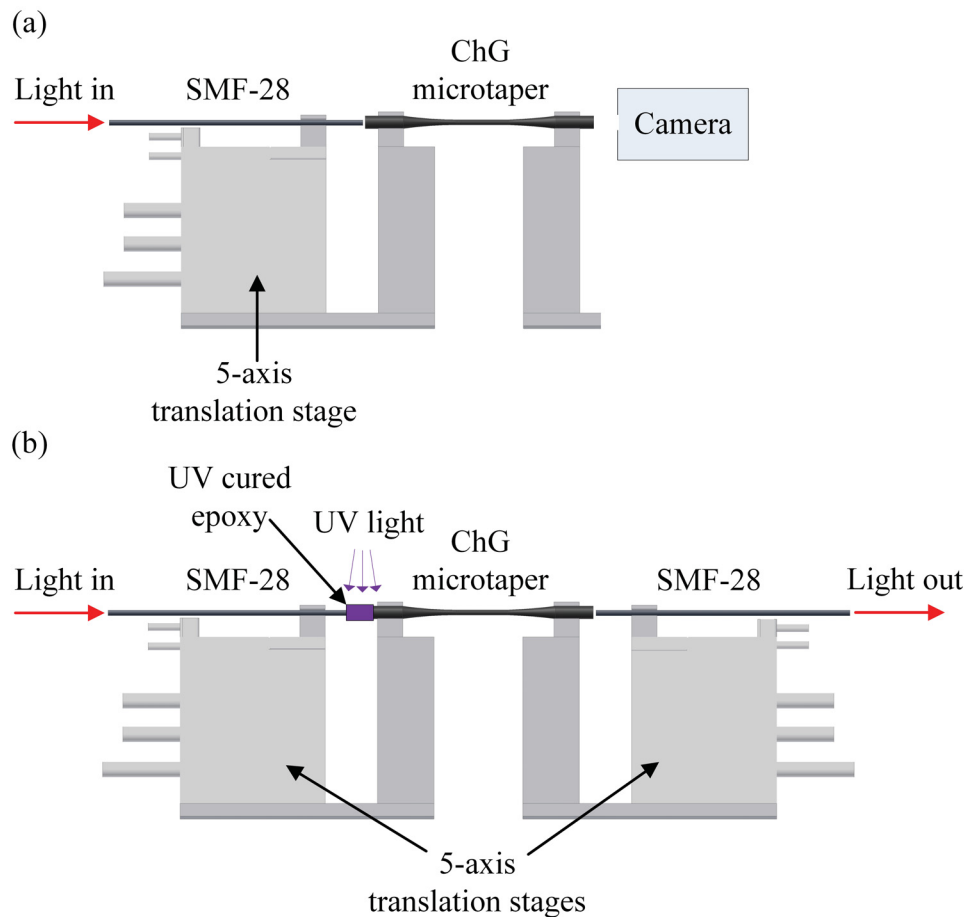


Fig. 3.10 Schematic of the coupling setup. (a) Input SMF-28 fiber and ChG microtaper alignment. (b) ChG microtaper and output SMF-28 fiber alignment and subsequent UV curing.

Alignment between SMF-28 fiber and ChG microtaper is an important step to achieve high coupling efficiency. The main loss factors in coupling process is fiber to microtaper and microtaper to fiber end facet misalignments. There are three types of misalignments, including lateral misalignment, longitudinal misalignment, and angle misalignment. Figure 3.11(a), (b), and (c) show schematic of lateral misalignment, longitudinal misalignment, and angle misalignment, respectively.

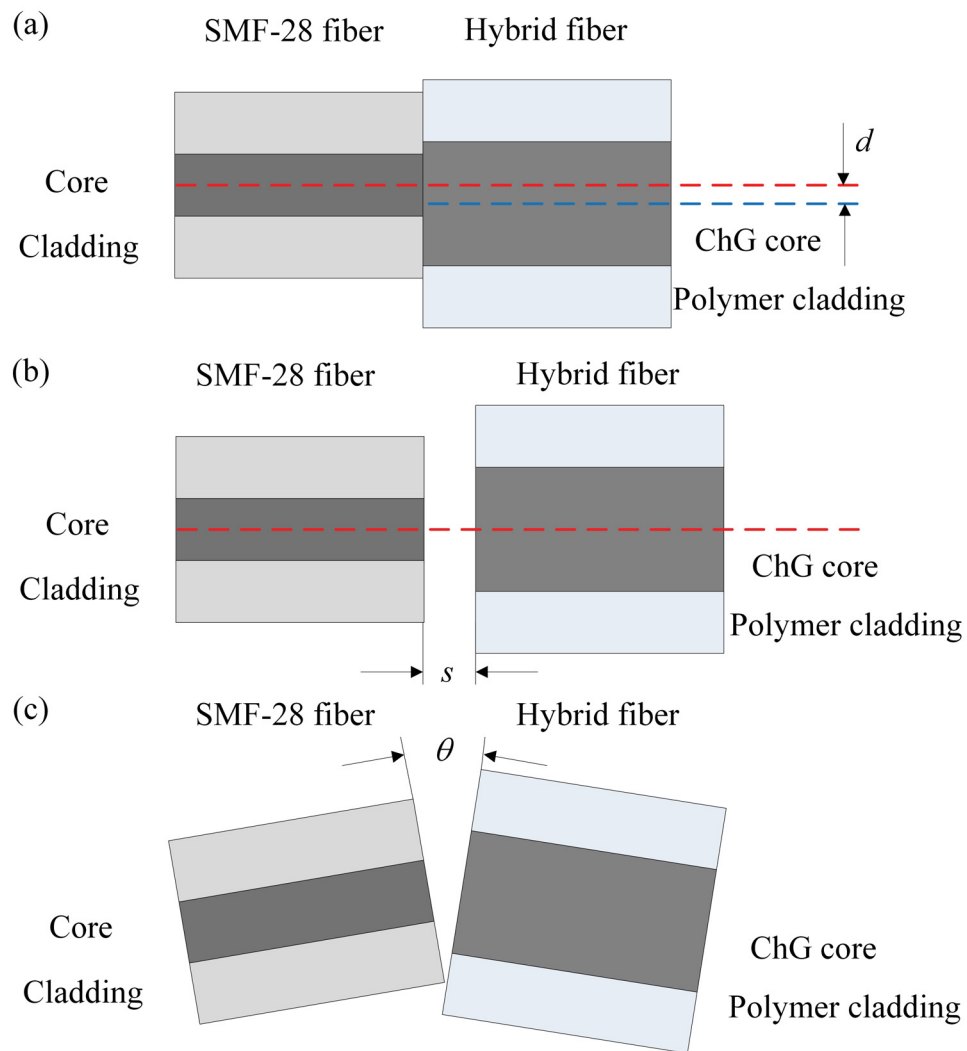


Fig. 3.11 (a) Schematic of lateral misalignment. (b) Schematic of longitudinal misalignment. (c) Schematic of angle misalignment.

3.4 Modeling

The wavelength-dependent refractive index of As_2Se_3 is calculated from the sellmeier equation Eq. 2.3. The sellmeier coefficients are $A_1=2.234921$, $A_2=0.347441$, $A_3=1.308575$, $\lambda_1=0.24164 \mu m$, $\lambda_2=19 \mu m$, and $\lambda_3=0.48328 \mu m$ [2]. The refractive indices of PMMA, PC and COP are calculated from the Cauchy equation

$$n^2(\lambda) = B_1 + B_2\lambda^2 + B_3\lambda^{-2} + B_4\lambda^{-4} + B_5\lambda^{-6} + B_6\lambda^{-8} \quad (3.5)$$

Table 3.5 Cauchy coefficients of PC, COP and PMMA

	PC	COP	PMMA
B_1	+2.430734	+2.482396	+2.399964
B_2	-1.343233×10^{-3}	$+6.959910 \times 10^{-2}$	-8.308636×10^{-2}
B_3	$+2.714995 \times 10^{-2}$	-1.597726×10^{-1}	-1.919569×10^{-1}
B_4	$+3.244405 \times 10^{-4}$	$+7.383333 \times 10^{-2}$	$+8.720608 \times 10^{-2}$
B_5	$+7.013408 \times 10^{-5}$	-1.398485×10^{-2}	-1.666411×10^{-2}
B_6	$+5.615956 \times 10^{-6}$	$+9.728455 \times 10^{-4}$	$+1.169519 \times 10^{-3}$

Table 3.5 summarizes the Cauchy coefficients of PC, COP and PMMA [143, 144]. Figure 3.12 (a) and (b) show the refractive index of As_2Se_3 , PC, COP, and PMMA, respectively, as a function of wavelength. The refractive index of As_2Se_3 (2.81 at $1.94 \mu m$) is much higher than that value of PC (1.56 at $1.94 \mu m$), COP (1.52 at $1.94 \mu m$) and PMMA (1.48 at $1.94 \mu m$) leading to a high refractive index contrast between the As_2Se_3 core and polymer cladding. This high refractive index contrast ensures that the propagation mode is strongly confined inside the As_2Se_3 core.

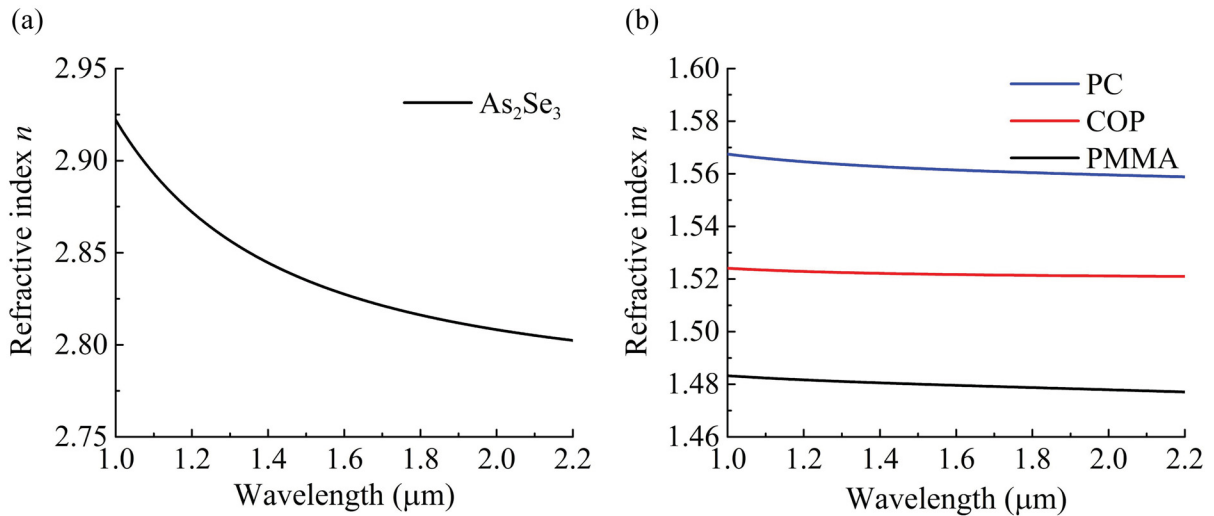


Fig. 3.12 (a) Refractive index of As₂Se₃ versus wavelength. (b) Refractive index of PC, COP and PMMA versus wavelength.

Maximizing coupling efficiency between polymer-cladded As₂Se₃ hybrid fiber and SMF-28 fiber is an important design criterion. The coupling efficiency is calculated by the overlap integral [145]

$$\eta = \frac{4\beta_i\beta_t}{(\beta_i + \beta_t)^2} \frac{\left[\iint \vec{E}_t \cdot \vec{E}_i^* dx dy \right]^2}{\left[\iint \vec{E}_t \cdot \vec{E}_t^* dx dy \right] \left[\iint \vec{E}_i \cdot \vec{E}_i^* dx dy \right]} \quad (3.6)$$

where β and \vec{E} are the propagation constant and the electric field distribution of the HE₁₁ mode. The subscripts i and t stand for the incident and transmitted light. Fig. 3.13 shows the coupling efficiency as a function of the COP-cladded ChG hybrid fiber core diameter. The maximum coupling efficiency of 85% is obtained when the core diameter of COP-cladded ChG hybrid fiber is 18 μm. As a result, the coupling loss is 0.7 dB for each end facet, including 0.5 dB of Fresnel reflection loss at the fiber interfaces, and the rest due to mode-mismatch losses. In practice, the coupling loss might be larger than 0.7 dB. The extra loss could come from core-cladding surface roughness, core diameter fluctuation, scratched fiber end facets and misalignment.

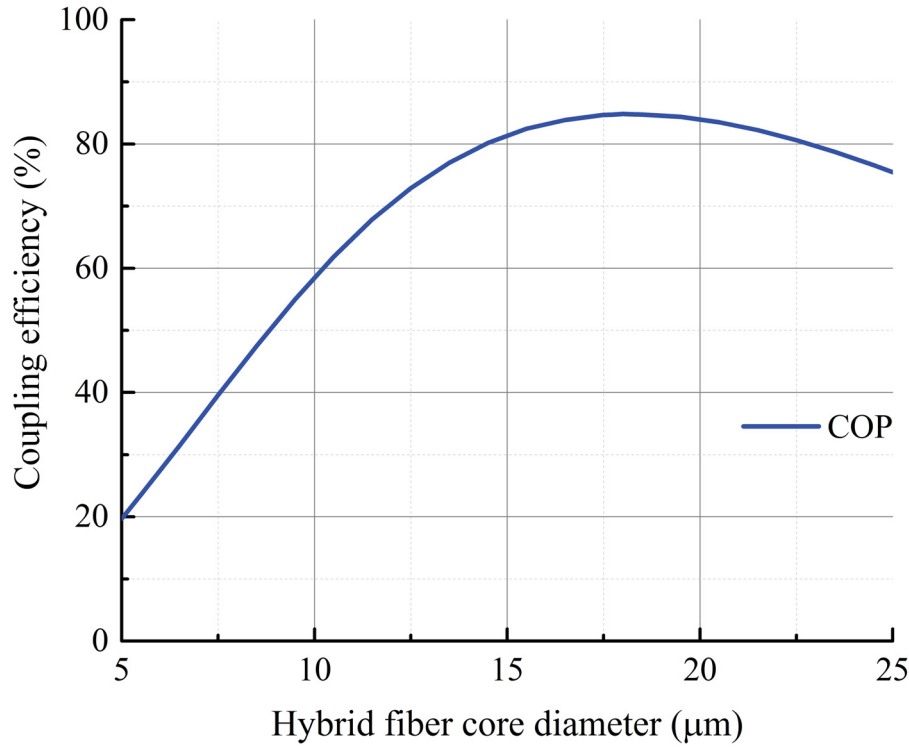


Fig. 3.13 Calculated coupling efficiency as a function of the COP-cladded As_2Se_3 hybrid fiber core diameter.

Chromatic dispersion β_2 , nonlinearity parameter γ , and confinement factor $\Gamma = P_{\text{core}}/P_{\text{total}}$, where P_{core} is the modal power enclosed in the core and P_{total} is the total mode power, and effective mode area A_{eff} are four fundamental parameters of a microwire. Their values depend on the microwire diameter and materials composition. Solving the characteristic equation of a cylindrical waveguide leads to the propagation constant β and the electric and magnetic fields distribution E and H for the fundamental HE_{11} mode, themselves leading to β_2 , γ , Γ and A_{eff} [59]. Figure 3.14(a) and (b) present β_2 and γ of the PC-, COP 480R-, and PMMA-cladded As_2Se_3 microwires as a function of core diameter at an operation wavelength of $1.94 \mu\text{m}$. Every polymer-cladded microwire has two zero dispersion diameters (ZDD), which are defined as ZDD_1 and ZDD_2 in the order of increasing wire diameter. When the diameter increases, β_2 asymptotically converges towards the value of bulk As_2Se_3 . The advantage of a double ZDD microwire is that it enables to select which ZDD should be used based on the application requirements. At ZDD_1 , the microwire has high γ , but the slope of β_2 ($= \beta_3$) is large, the microwire has relatively low confinement factor, and thus the attenuation caused by the evanescent wave in an absorbing cladding is comparatively high. At ZDD_2 , the

microwire has a slightly reduced γ , but the slope of β_2 is small. As well the confinement factor is higher than at ZDD₁, and thus an absorbing cladding has less impact at ZDD₂ than at ZDD₁.

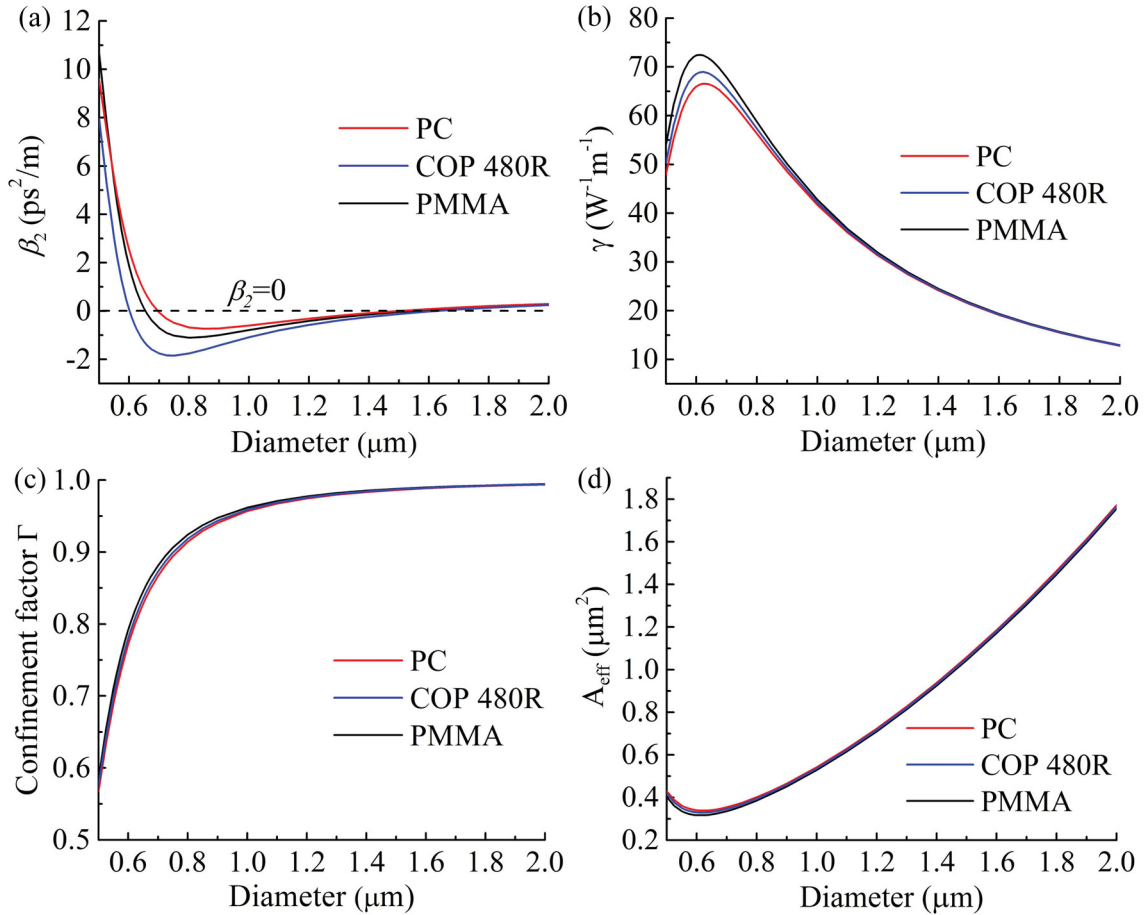


Fig. 3.14 (a) Chromatic dispersion β_2 . (b) Waveguide nonlinearity parameter γ . (c) Confinement factor Γ . (d) Effective mode area A_{eff} of the PC-, COP 480R- and PMMA-cladded microwires as a function of the As₂Se₃ core diameter at an operation wavelength of 1.94 micrometers.

Figure 3.14(c) and (d) show the Γ and A_{eff} of the PC-, COP 480R-, and PMMA-cladded microwires as a function of the As₂Se₃ core diameter at an operation wavelength of 1.94 micrometers. The mode confinement increases with increasing core diameter. The attenuation coefficient α_{total} resulting from the modal propagation in a waveguide is given by $\alpha_{\text{total}} = \alpha_{\text{core}} \times \Gamma + \alpha_{\text{clad}} \times (1 - \Gamma)$, where α_{core} is the attenuation coefficient of the core material, and α_{clad} is the attenuation coefficient of the cladding material. Table 3.4 summarizes β_2 , γ and Γ at relevant diameters of As₂Se₃-PMMA,

As₂Se₃-PC, and As₂Se₃-COP 480R microwires.

Table 3.6 Dispersion, nonlinearity and confinement properties of PMMA-, PC-, and COP 480R-cladded microwires at an operation wavelength of 1.94 μm. γ_{\max} : maximum γ ; $d_{\gamma_{\max}}$: diameter corresponding to maximum γ

	PMMA	PC	COP 480R
ZDD ₁ (μm)	0.655	0.696	0.602
γ at ZDD ₁ (W ⁻¹ m ⁻¹)	71.1	64.0	68.7
Γ at ZDD ₁	0.847	0.861	0.788
ZDD ₂ (μm)	1.549	1.497	1.625
γ at ZDD ₂ (W ⁻¹ m ⁻¹)	20.5	21.5	18.8
Γ at ZDD ₂	0.989	0.986	0.990
γ_{\max} (W ⁻¹ m ⁻¹)	72.5	66.6	68.9
$d_{\gamma_{\max}}$ (μm)	0.616	0.628	0.616
Γ at $d_{\gamma_{\max}}$	0.808	0.802	0.806
β_2 at $d_{\gamma_{\max}}$ (ps ² /m)	1.16	1.47	-0.49

3.5 Experimental results

For the experiment, polymer-cladded microwires with PC, COP and PMMA claddings have been designed with a diameter of 1.5 μm and a length of 10 cm. The diameter size has been selected because of the following aspects: This diameter is close to ZDD₂ and thus desirable for practical applications when normal, anomalous or zero dispersion is needed. Secondly, γ is significantly large at this point, thus being useful for nonlinear applications with compact size and low power consumption. Finally and most importantly, we should observe the absorption features of the various polymers via evanescent wave coupling, if there is any, as expected from Γ . As well, the microwire section length of the polymer-cladded microtapers was chosen 10 cm long in order to highlight the absorption features in those microwires. The total absorption of the microwire increases exponentially with increasing length. However take note that in many practical applications, a microwire shorter than 10 cm provides enough nonlinearity to be functional, limiting the negative impact of an absorptive cladding [5]. The optical transmission of polymer-cladded As₂Se₃ microwires has been measured in the spectral window in between 1.45 μm and 2.20 μm using a combination of erbium and thulium amplified spontaneous emission (ASE) source, and a Yokogawa AQ6375 optical spectrum analyzer (OSA) at either side of the device under test. Figure 3.15(a) and (b) show the schematic of PC-, COP-, and PMMA-cladded As₂Se₃ microtaper and

the setup for optical transmission measurement, respectively. PC-, COP 480R-, COP 1020R-, and PMMA-cladded As_2Se_3 microwires with core diameter $\phi_{\text{As}_2\text{Se}_3}=1.5 \mu\text{m}$ and length $L_w=10 \text{ cm}$ have been fabricated and tested.

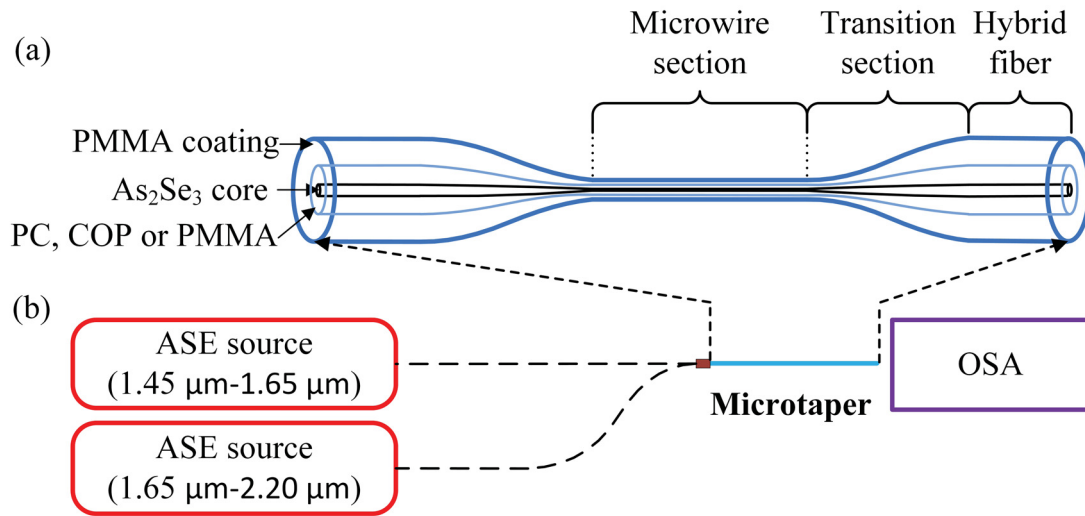


Fig. 3.15 (a) Schematic of the PC-, COP- and PMMA-cladded As_2Se_3 microtaper. (b) Setup for optical transmission measurement.

Figure 3.16(a) shows the measured transmission spectra of PC [95], COP 1020R [95] and PMMA [95] sheet with the same thickness of 3.2 mm. Figure 3.16(b) shows the normalized transmission spectrum of each polymer-cladded As_2Se_3 microwire. The typical SMF-28 to SMF-28 insertion loss of the microwires is 4 dB at a wavelength of 1.55 μm . At wavelengths in between 1.85 μm and 2.20 μm , the transmittance spectrum of microwires with PC, COP 480R and COP 1020R claddings is increased with respect to microwires made solely out of PMMA. Especially when the operating wavelength is above 1.9 μm , PC and COP claddings transmit significantly better than PMMA. All of these polymers have absorption peaks around 1.7 μm , caused by the first order overtone of C-H bonds.

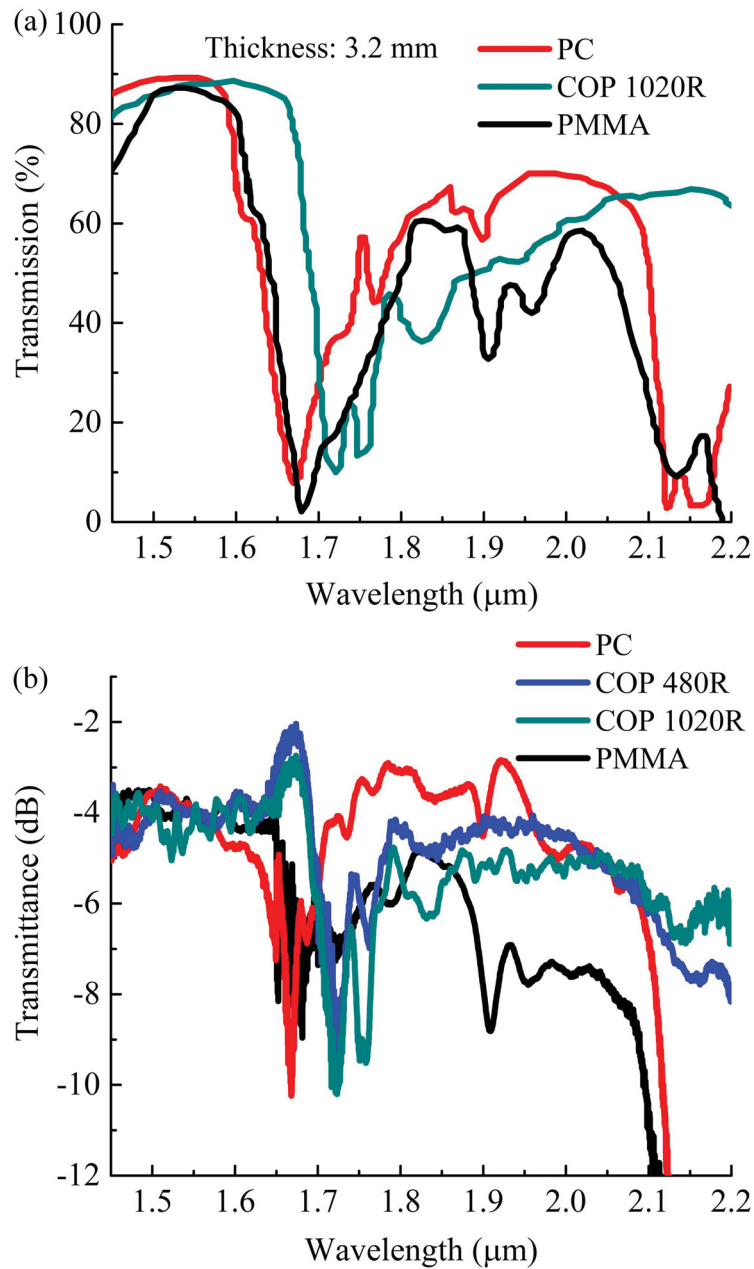


Fig. 3.16 (a) Transmission spectra of PC, COP 1020R and PMMA. (b) SMF-28 to SMF-28 transmittance of the PC-, COP 480R-, COP 1020R- and PMMA-cladded microwires with diameter $\phi_{\text{As}_2\text{Se}_3} = 1.5 \mu\text{m}$ and length $L_w = 10 \text{ cm}$.

PC- and PMMA-cladded As_2Se_3 microwires transmit light with an abrupt cut at $2.1 \mu\text{m}$. COP 480R- and COP 1020R-cladded As_2Se_3 microwires transmit light up to at least $2.2 \mu\text{m}$, limited by

the experimental transmission measurement. The transmission spectrum of each polymer-cladded As_2Se_3 microwire, as shown in Fig. 3.16(b), is consistent with the transmission spectrum of bulk polymer, as shown in Fig. 3.16(a).

Next, we compare the efficiency of nonlinear processes between COP 480R- and PMMA-cladded As_2Se_3 microwires. To get equal waveguide nonlinear parameters, the corresponding core diameters of COP- and PMMA-cladded microwires are $1.49 \mu\text{m}$ and $1.50 \mu\text{m}$, respectively, leading to $\gamma=21.7 \text{ W}^{-1}\text{m}^{-1}$ in both cases. As well, pump pulses centered at a wavelength of $1.94 \mu\text{m}$ and with a duration of 3 ps are being launched into the microwires. The average input power delivered into the microwire section is 1.3 mW, corresponding to a peak pulse power of 14.1 W. The transmission loss of the 10 cm long COP 480R- and PMMA-cladded As_2Se_3 microwires at a wavelength of $1.94 \mu\text{m}$ is 0.33 dB/cm and 0.59 dB/cm, respectively, leading to an effective length $L_{\text{eff}}=(1-\exp(-\alpha L))/\alpha$ of 7.00 cm and 5.46 cm, respectively. Figure 3.17 shows the experimental setup for Raman-enhanced FWM generation.

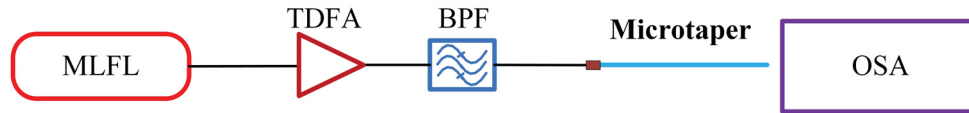


Fig. 3.17 Setup for Raman-enhanced FWM generation. MLFL: mode-locked fiber laser; TDFA: thulium-doped fiber amplifier; BPF: bandpass filter; OSA: optical spectrum analyzer.

Figure 3.18 shows the resulting spectra of COP 480R- and PMMA-cladded microwires pumped by 3 ps pulses centered at a wavelength of $1.94 \mu\text{m}$. Transmission spectra are also given for reference. As the peak pump power is increased up to 14.1 W, nonlinear scattering bands are observed along with spectral broadening of the pump signal. For COP 480R- and PMMA-cladded As_2Se_3 microwires, the theoretical nonlinear phase shift $\varphi_{\text{NL}}=\gamma P_0 L_{\text{eff}}$ is 6.82π and 5.32π , respectively, which agrees well with the measured nonlinear phase shift φ_{NL} extracted from spectra in Fig. 3.18. Taking the pump wavelength as a reference, the nonlinear scattering towards longer wavelengths includes Raman scattering and FWM; the nonlinear scattering in the shorter wavelength direction includes only FWM. $S_{\pm n}^m$ means n th order nonlinear scattering, \pm signs stand for a nonlinear scattering at longer/shorter wavelengths with respect to the pump. The superscript m designates the cladding material of the microwire (p for PMMA, c for COP 480R). The peak value of S_1^c is 10.3 dB higher than that value of S_1^p shown in Fig. 3.18 since the transmission loss of COP 480R-cladded As_2Se_3 microwire is more than 2.5 dB lower than that value of PMMA-cladded As_2Se_3

microwire at the corresponding wavelength. Also, the bandwidth of S_1^c is 16 nm wider than that value of S_1^p . With same pump peak power of 14.1 W, COP 480R-cladded As_2Se_3 microwire has second order nonlinear scattering S_2^c in longer wavelength direction. In contrast, PMMA-cladded As_2Se_3 microwire does not have second order nonlinear scattering since the transmission loss of PMMA-cladded As_2Se_3 microwire is more than 6 dB larger than that value of COP 480R-cladded As_2Se_3 microwire above 2.1 μm . The peak value of S_{-1}^c is 4.3 dB higher than that value of S_{-1}^p . The bandwidth of S_{-1}^c is 4.9 nm wider than that value of S_{-1}^p . The peak value of S_2^c is slightly lower than that value of S_2^p . Also, the bandwidth of S_2^c is narrower than that value of S_2^p since COP has two absorption peaks located at 1.73 μm and 1.76 μm , which increase the transmission loss, and reduce the nonlinear scattering.

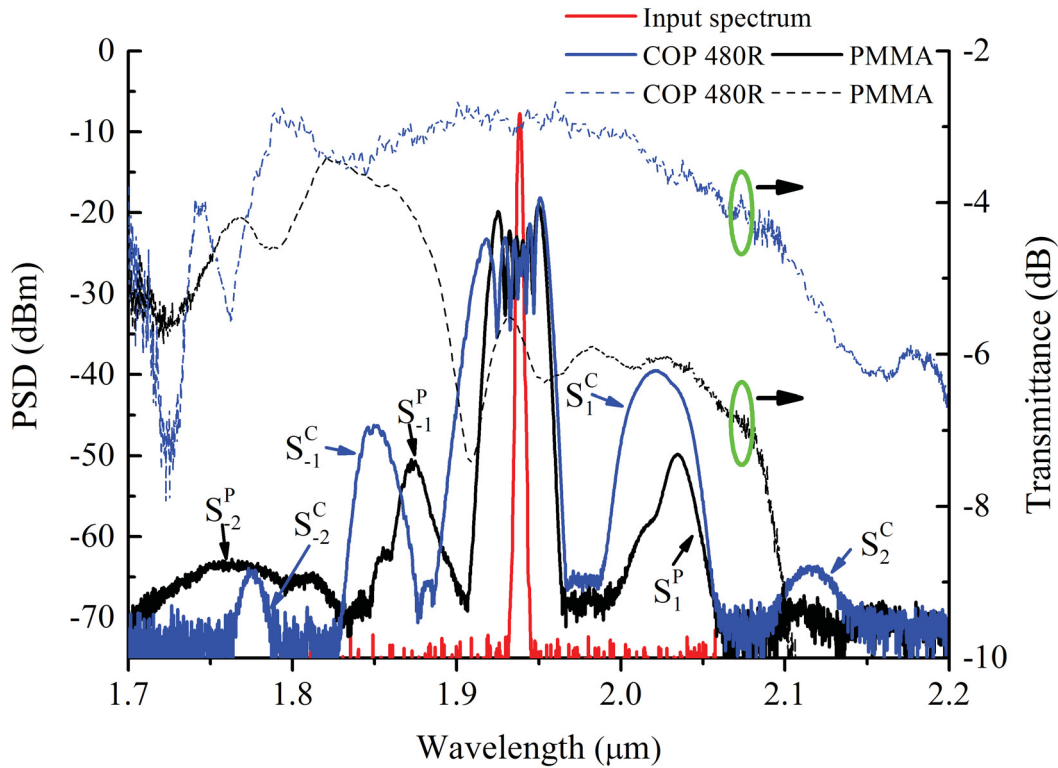


Fig. 3.18 Nonlinearly broadened spectra of COP 480R- and PMMA-cladded microwires with length $L_w=10$ cm and $\gamma=21.7$ $W^{-1}m^{-1}$. The peak pump power is 14.1 W and is centered at a wavelength of 1.94 μm . Transmission spectra are also given for reference.

3.6 Conclusion

In summary, PC-, COP 480R-, COP 1020R-, and PMMA-cladded As_2Se_3 microwires have been designed, fabricated and characterized. Microwires with PC cladding have better transmission than that with PMMA cladding at wavelengths from 1.85 μm to 2.10 μm . Microwires with COP 480R cladding have better transmission than that with PMMA cladding at wavelengths from 1.85 μm to >2.20 μm . Due to the strong absorption of C-H bonds, the transmission of PC-cladded As_2Se_3 microwires with length of 10 cm is limited to an upper bound of 2.12 μm . The COP 480R- and COP 1020R-cladded As_2Se_3 microwires with length of 10 cm transmit light up to at least 2.20 μm . The transmission window of these microwires can be further extended by reducing the wire length. Compared with PMMA-cladded microwires, COP 480R-cladded microwires provide an increased nonlinear gain and wider gain bandwidth from 1.85 μm to >2.20 μm .

Chapter 4

ChG optical microwires cladded with fluorine-based CYTOP

4.1 Introduction

The MIR range (2-12 μm) of the optical spectrum is intimately associated with vibrational motion in molecules, enabling many applications related to spectroscopy and chemical sensing [38, 42, 43]. Among the approaches utilized to generate MIR light, light sources that depend on nonlinear parametric gain, such as parametric oscillators and SC sources raise a great deal of interest due to their broadband operation [56, 57, 59]. Parametric processes in a MIR optical source are supported given that the gain medium possesses a sufficiently large nonlinearity coefficient, a good transparency in the MIR, and allows the access to a group velocity dispersion that is close to zero at the pump wavelength.

ChG glasses are such materials compatible with the MIR, covering the spectral range of 1-12 μm for As_2Se_3 and the range of 1-8 μm for As_2S_3 [2, 3]. ChG glasses are also highly nonlinear media given their intrinsic nonlinear refractive index (n_2) up to three orders of magnitude larger than the n_2 of silica glass [1]. Nonlinear effects can also be enhanced from a high-confinement waveguide geometry such as the fiber microwire and the photonic crystal fiber [6, 146].

Resulting from the combination of ChG glass and a high-confinement waveguide geometry, ChG microwires are promising components for the fabrication of MIR light sources from parametric processes [13]. With waist diameters at sub-wavelength scale, ChG microwires must be coated to provide mechanical strength and optical insensitivity to environment [7, 19].

Hydrogen-based polymers, including PMMA, PC and COP, were successfully used as cladding materials for As_2Se_3 microwires [147]. However, the transmission loss of hydrogen-based polymers increases abruptly at wavelengths beyond $1.55 \mu\text{m}$, thereby limiting their use. This absorption is caused by molecular resonances at fundamental and overtone transitions of C-H bonds [126]. A material free from C-H bonds is thus desirable to avoid the absorption peaks of hydrogen-based polymers and enables optical transmission at wavelengths beyond $1.55 \mu\text{m}$ and further into the MIR.

An alternative to C-H based polymers is the use of another MIR-transparent ChG glass such as As_2S_3 [148]. Unfortunately, the combination of As_2Se_3 core with an As_2S_3 cladding (or any known ChG-ChG combination) provides a refractive index contrast that is too low to bring the zero dispersion wavelength of a microwire below $3.7 \mu\text{m}$, imposing a normal dispersion to all wavelengths $<3.7 \mu\text{m}$. As a result, parametric amplification with such compositions can not be generated from a pump wavelength $\leq 3.7 \mu\text{m}$.

In this chapter, we use fluorine-based CYTOP as a cladding material for As_2Se_3 microwires and demonstrate that CYTOP enables excellent transmission and nonlinear functionalities of the microwire at wavelengths of $1.5 \mu\text{m}$ up to $>4.3 \mu\text{m}$. Not only transmission losses remain low in this wavelength range but also the group-velocity dispersion at these wavelengths can be engineered as normal, anomalous or zero value. We use the high nonlinearity of the CYTOP-cladded microwire to demonstrate multiple orders of FWM and SC generation. The transparency of CYTOP-cladded microwire is also compared to those of COP- and PMMA-cladded microwires.

4.2 The polymer cladding

Table 4.1 summarizes the common amorphous and crystalline perfluorinated and partial fluorinated polymers, including CYTOP, Teflon AF 1600 and 2400, Polytetrafluoroethylene (PTFE), Fluorinated Ethylene Propylene (FEP), Ethylene Tetrafluoroethylene (ETFE), Polyvinylidene Difluoride (PVDF), Polyvinyl Fluoride (PVF). Table 4.1 also introduces the physical properties of those polymers, including the classification of amorphous and crystalline state, melting temperature T_m ($^\circ\text{C}$), glass transition temperature T_g ($^\circ\text{C}$), and refractive index n at $1.55 \mu\text{m}$. CYTOP, Teflon AF 1600 and 2400 are amorphous perfluorinated polymers. Among these polymers, CYTOP and Teflon AF 1600 are good choice for cladding ChG material since their glass transition temperatures are compatible with that value of ChG material. PTFE and FEP are crystalline perfluorinated polymers. The melting temperatures of those polymers are much higher than the glass transition tempera-

ture of ChG material. The scattering losses of those polymers are large due to their crystalline structure. ETFE, PVDF, and PVF are partial fluorinated polymers. Besides carbon-fluorine (C-F) bonds, those polymers also contain C-H bonds. The fundamental vibrational wavelength of a C-H bond is 3.4 μm . The second order vibrational wavelength of a C-H bond is 1.7 μm , which will cause relatively large absorption loss above 1.7 μm .

Table 4.1 Common fluorine-based polymers and their physical parameters

Name	Type	T_m ($^{\circ}\text{C}$)	T_g ($^{\circ}\text{C}$)	n
CYTOP	Amorphous	Not observed [149]	108 [150]	1.33 [151]
Teflon AF 1600	Amorphous	Not observed [152]	160 [153]	1.30 [154]
Teflon AF 2400	Amorphous	Not observed [152]	240 [153]	1.28 [155]
PTFE	Crystalline	342 [156]	127 [157]	1.35 [158]
FEP	Crystalline	265 [159]	54 [160]	1.34 [112]
ETFE	Crystalline	250 [161]	119 [162]	1.39 [112]
PVDF	Crystalline	168 [163]	-45 [163]	1.38 [164]
PVF	Crystalline	200 [165]	40.8 [166]	1.47 [112]

Figure 4.1 shows the chemical structure of fluorine-based polymer CYTOP, hydrogen-based polymers COP and PMMA. As described in chapter 3, the vibrational frequency is inversely related to the reduced mass, substituting fluorine element for the hydrogen element in C-H bonds will greatly increase the reduced mass, thus increasing the wavelengths of fundamental and overtone vibrational transitions.

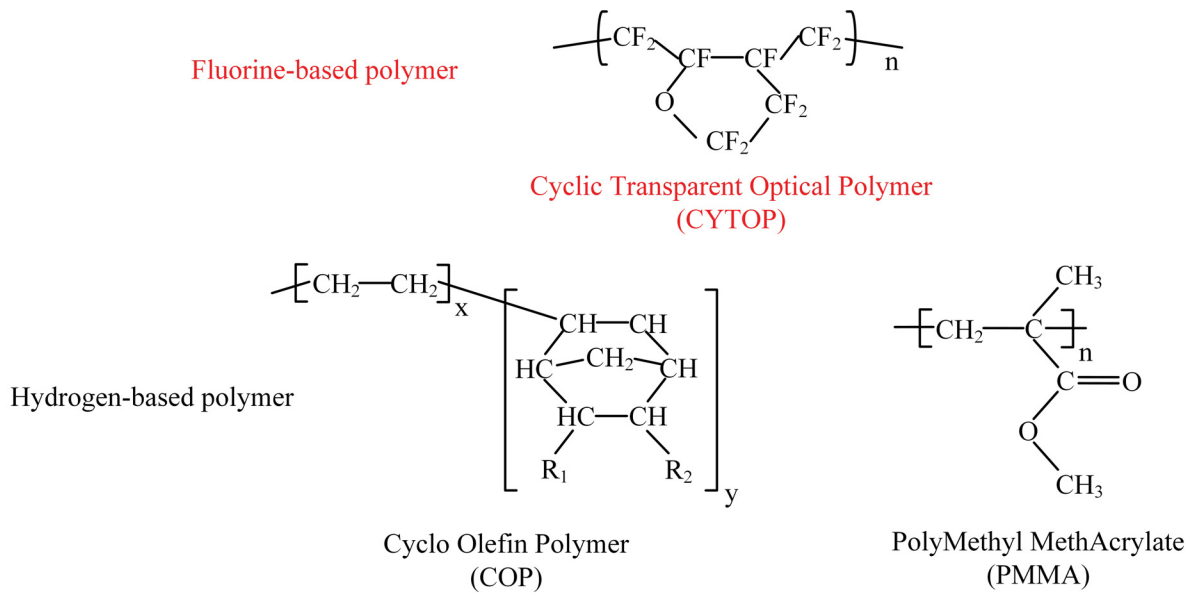


Fig. 4.1 Chemical structure of fluorine-based polymer CYTOP, hydrogen-based polymer COP and PMMA.

Fluorine-based CYTOP (Asahi Glass) is a polymer composed of C-F, C-C, and C-O bonds [167]. This differs from widespread hydrogen-based polymers such as COP and PMMA which possess C-H bonds, in addition to C-C and C-O bonds. The transparency in the short MIR wavelengths of a fluorine based polymer versus a hydrogen based polymer is influenced by the presence of C-F bonds rather than C-H bonds. Table 4.2 summarizes vibrational wavelengths of different chemical bonds in CYTOP, COP and PMMA. Vibrational wavelengths of a C-F bond are 8.0 μm (1st order) and 4.0 μm (2nd order) whereas the vibrational wavelengths of a C-H bond are 3.4 μm (1st order) and 1.7 μm (2nd order). The vibrational wavelengths of C-C and C-O bonds occur at 8.9 μm (1st order) and 9.1 μm (1st order), respectively, and thus the lowest vibrational wavelength is determined by the presence of C-F or C-H bonds. The fluorine-based polymers thus have absorption peaks at longer wavelengths with respect to the hydrogen-based polymers. Another advantageous property of CYTOP is the low refractive index of 1.33 (at $\lambda=1.55 \mu\text{m}$), leading to a high refractive index contrast when used to clad an As₂Se₃ core. This large refractive index contrast provides flexibility in adjusting the zero dispersion wavelength from the zero dispersion wavelength of bulk As₂Se₃ ($\sim 7 \mu\text{m}$) down to $\sim 1 \mu\text{m}$.

Table 4.2 Vibrational wavelengths of different chemical bonds

Bond	1 st order vibrational wavelength (μm)	2 nd order vibrational wavelength (μm)
C-F	8.0	4.0
C-H	3.4	1.7
C-C	8.9	-
C-O	9.1	-
C=O	5.4	2.7

The absorption loss due to the fundamental vibration and its overtones of a C-F bond could be calculated from Eq. 3.4. Figure 4.2 shows the calculated absorption loss due to the fundamental vibration and its overtones of a C-F bond and a C-H bond.

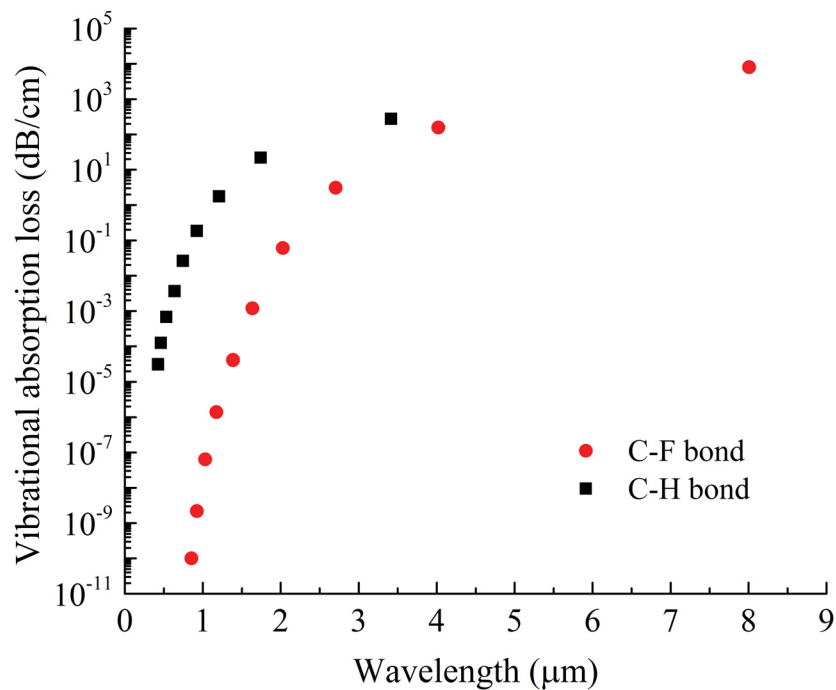


Fig. 4.2 Calculated fundamental and overtones vibrational absorption of a C-F bond and a C-H bond.

4.3 Design

Figure 4.3 shows the refractive index of As_2Se_3 and CYTOP. The refractive index of As_2Se_3 is calculated using the Sellmeier equation Eq. 2.3 and Sellmeier coefficients described in Chapter 3.

The refractive index of CYTOP is calculated using the Sellmeier equation Eq. 2.3 and Sellmeier coefficients $A_1^2=0.33409$, $A_2^2=0.4528$, $A_3^2=0.53494$, $\lambda_1=81.2$, $\lambda_2=77.4$, and $\lambda_3=12300$ [168]. The unit of λ is nm. As shown in Fig. 4.3, the refractive index of As_2Se_3 (2.81 at $1.94 \mu\text{m}$) is much higher than that value of CYTOP (1.33 at $1.94 \mu\text{m}$) leading to a high confinement factor.

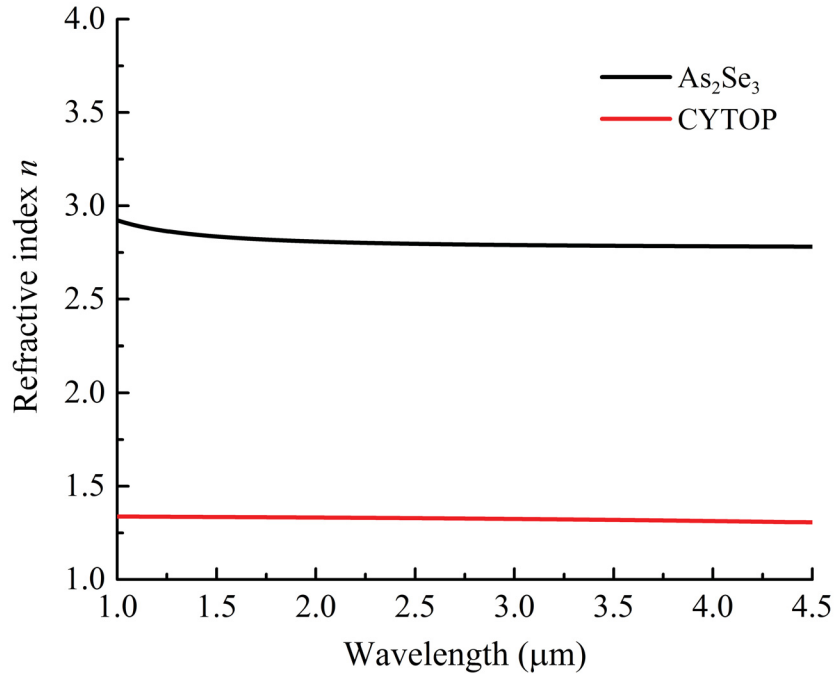


Fig. 4.3 Refractive index of As_2Se_3 and CYTOP.

It is important to maximize coupling efficiency between polymer-cladded As_2Se_3 hybrid fiber and SMF-28 fiber. The coupling efficiency is calculated by Eq. 3.6. Figure 4.4 shows the coupling efficiency versus the hybrid fiber core diameter. The optimal coupling efficiency of 85% is achieved when the core diameter of CYTOP-cladded As_2Se_3 hybrid fiber is $18 \mu\text{m}$.

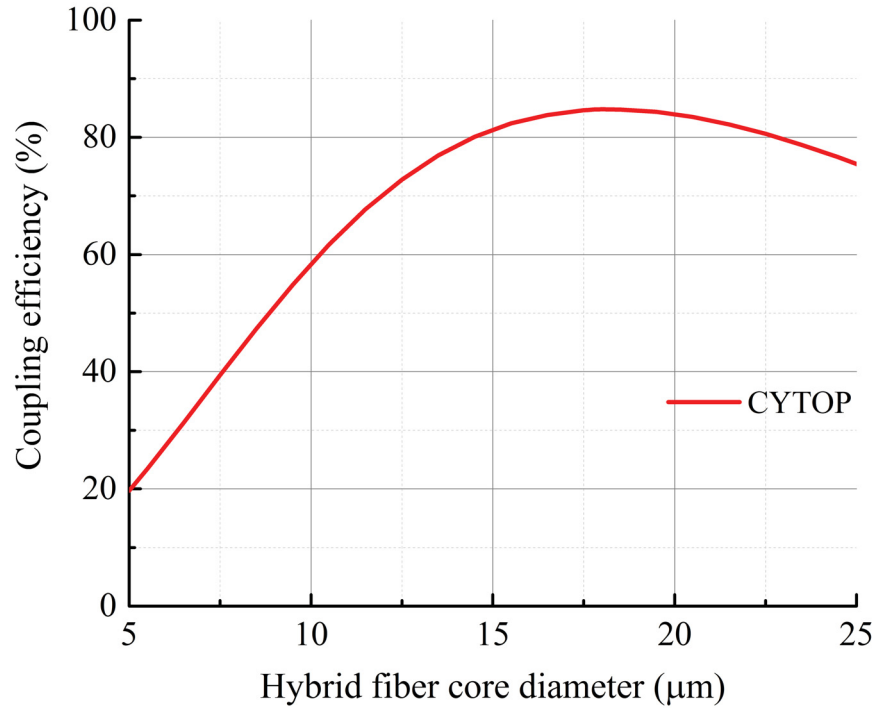


Fig. 4.4 Calculated coupling efficiency as a function of the CYTOP-cladded As_2Se_3 hybrid fiber core diameter.

The core diameter and core/cladding composition determine the optical parameters of the microwires: Group-velocity dispersion parameter β_2 , waveguide nonlinearity parameter γ , effective mode area A_{eff} , and confinement factor $\Gamma = P_{\text{core}}/P_{\text{total}}$, where P_{core} is the modal power enclosed within the core and P_{total} is the total modal power. Those parameters are evaluated from solving the characteristic equation of a cylindrical waveguide with high refractive index contrast and derived from the effective refractive index n_{eff} , the propagation constant β , and the electric and magnetic fields distribution E and H of the fundamental HE_{11} mode [4]. The waveguides characteristic equation is solved for a two-layer fiber structure, i.e. As_2Se_3 core, CYTOP cladding, as the PMMA coating carries a negligible amount of evanescent power [169].

Figure 4.5 presents β_2 , γ , Γ and A_{eff} of CYTOP-cladded As_2Se_3 microwires as a function of core diameter in the 1.5-4.5 μm wavelength range. The CYTOP-cladded microwire has two zero dispersion wavelengths (ZDW) for a given microwire core diameter, defined ZDW_1 and ZDW_2 in order of increasing wavelength. In a practical design, ZDW_1 is generally most useful to increase the gain bandwidth of parametric processes because the dispersion profile around ZDW_1 is flatter than that around ZDW_2 . As well, ZDW_1 provides a larger γ than ZDW_2 in the wavelength range

and microwire core diameter of interest. As shown in Fig. 4.5(c), the mode confinement decreases with increasing wavelengths for a given core diameter, corresponding to an expansion of the guided mode. As shown in Fig. 4.5(d), this results into an increase of A_{eff} and thus more of the modes evanescent wave propagating into the CYTOP cladding. The attenuation coefficient α_{total} arising from light transmission in the microwire is given by $\alpha_{\text{total}} = \alpha_{\text{AsSe}} \times \Gamma + \alpha_{\text{polymer}} \times (1 - \Gamma)$, where α_{AsSe} is the attenuation coefficient of As_2Se_3 , and α_{polymer} is the attenuation coefficient of the polymer. The impact of an absorbing cladding is thus reduced when operating the microwire at ZDW_1 rather than at ZDW_2 .

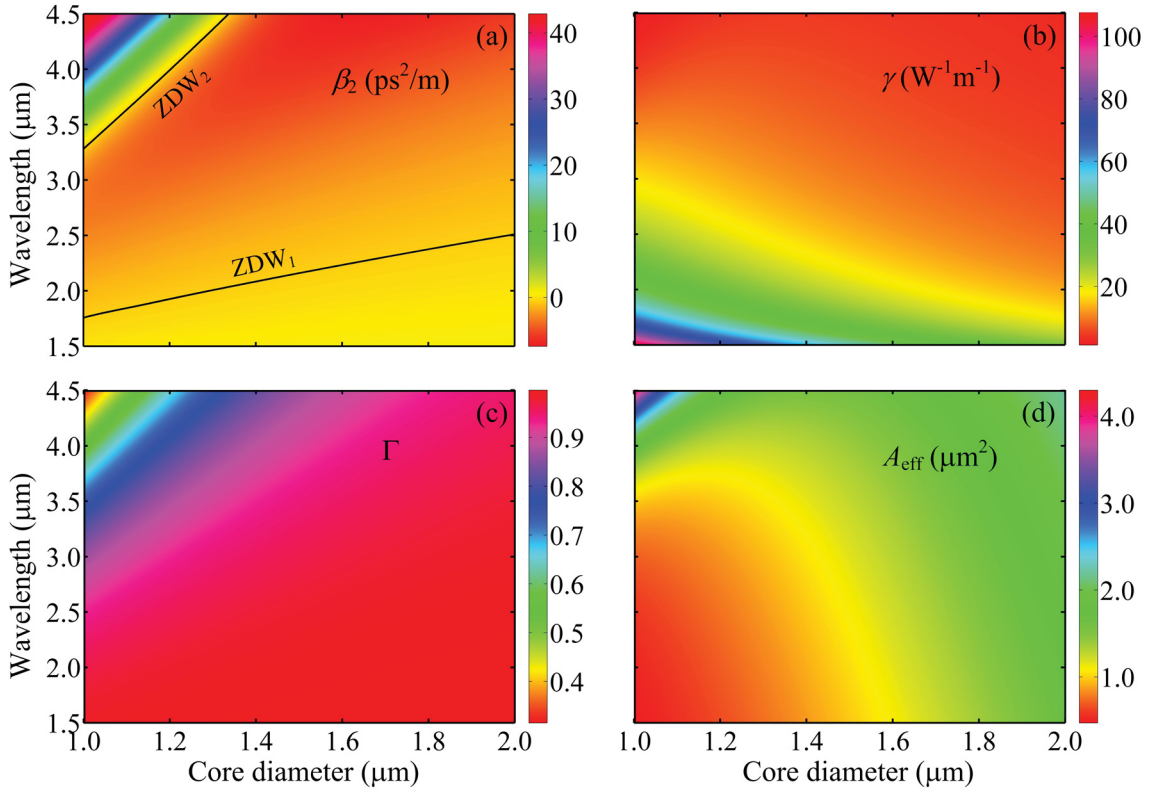


Fig. 4.5 Optical parameters of CYTOP-cladded As_2Se_3 microwires as a function of wavelength and core diameter: (a) β_2 ; (b) γ ; (c) Γ ; (d) A_{eff} .

4.4 Microwire fabrication

The fabrication of optical microwires with ChG core and polymer cladding requires the fulfilling of a few compatibility criteria. First, the polymer cladding must be transparent at the optical

wavelengths to be transmitted. Second, the refractive index of the polymer cladding should be as low as possible to ensure a large confinement factor and strong waveguide nonlinearity. Third, the glass transition temperature (T_g) and the temperature-dependent viscosity values should be as close as possible to facilitate mechanical compatibility [147]. Table 4.3 presents glass transition temperature, refractive index and viscosity of As_2Se_3 , CYTOP and PMMA.

Table 4.3 Glass transition temperature, refractive index ($\lambda=1.94 \mu m$) and viscosity ($T=210 \text{ }^\circ C$) of As_2Se_3 , CYTOP and PMMA

	Glass transition temperature T_g ($^\circ C$)	n	Viscosity (Poise)
As_2Se_3	167 [2]	2.81	$\sim 7.24 \times 10^9$ [129]
CYTOP	108 [167]	1.33	$\sim 1.33 \times 10^5$ [170]
PMMA	104 [137]	1.47	$\sim 2.12 \times 10^5$ [171]

CYTOP is a good material to clad As_2Se_3 -based microwires because it provides a significantly improved optical transmission in the MIR wavelengths with respect to hydrogen-based polymers. It also has a lower refractive index than ChG glasses and hydrogen-based polymers, leading to higher refractive index contrast, as well as it is being mechanically compatible with As_2Se_3 as required for the microwire fabrication.

The CYTOP-cladde d As_2Se_3 microwire is fabricated in four steps: Extrusion assembly, preform fabrication, fiber fabrication and microwire fabrication. Figure 4.6 illustrates the fabrication steps of the fiber. Figure 4.6(a) shows a schematic of the rod-in-tube method used to make the preform [142]. An As_2Se_3 rod is placed in a CYTOP tube, then the assembly is placed in a PMMA tube. It is part of our fabrication process to systematically cover preforms of various nature with PMMA to fine-tune the fiber geometry. The As_2Se_3 rod, CYTOP and PMMA tubes are dried in a vacuum oven prior to the preform fabrication process. Figure 4.6(b) shows a schematic of the CYTOP-cladde d preform fabrication setup, and a photograph of extruded preform. The assembly is fed through an aluminium funnel. Under heat and pressure, the PMMA tube and CYTOP tube shrink and fuse with the As_2Se_3 rod. The multimaterial composite flows out of the funnel and is pulled at a constant velocity to obtain a uniform preform. Next, the fiber is made by feeding the preform into a drawing funnel heated at controlled temperature. The softened preform is pulled into a fiber with predefined As_2Se_3 core diameter $\phi_{As_2Se_3}$, to achieve a maximum coupling efficiency with e.g. SMF-28 fiber. Figure 4.6(c) shows a schematic of the CYTOP-cladde d fiber fabrication setup, a photograph of fiber drawing and a photograph of fiber cross-section. With a cladding to

core diameter ratio of 4.2, a microwire with a core diameter of $1.55 \mu\text{m}$ will allow 0.0002% of the evanescent field power to penetrate the PMMA coating in the $1.5\text{-}4.5 \mu\text{m}$ wavelength range, as estimated from Lumerical-MODE Solutions.

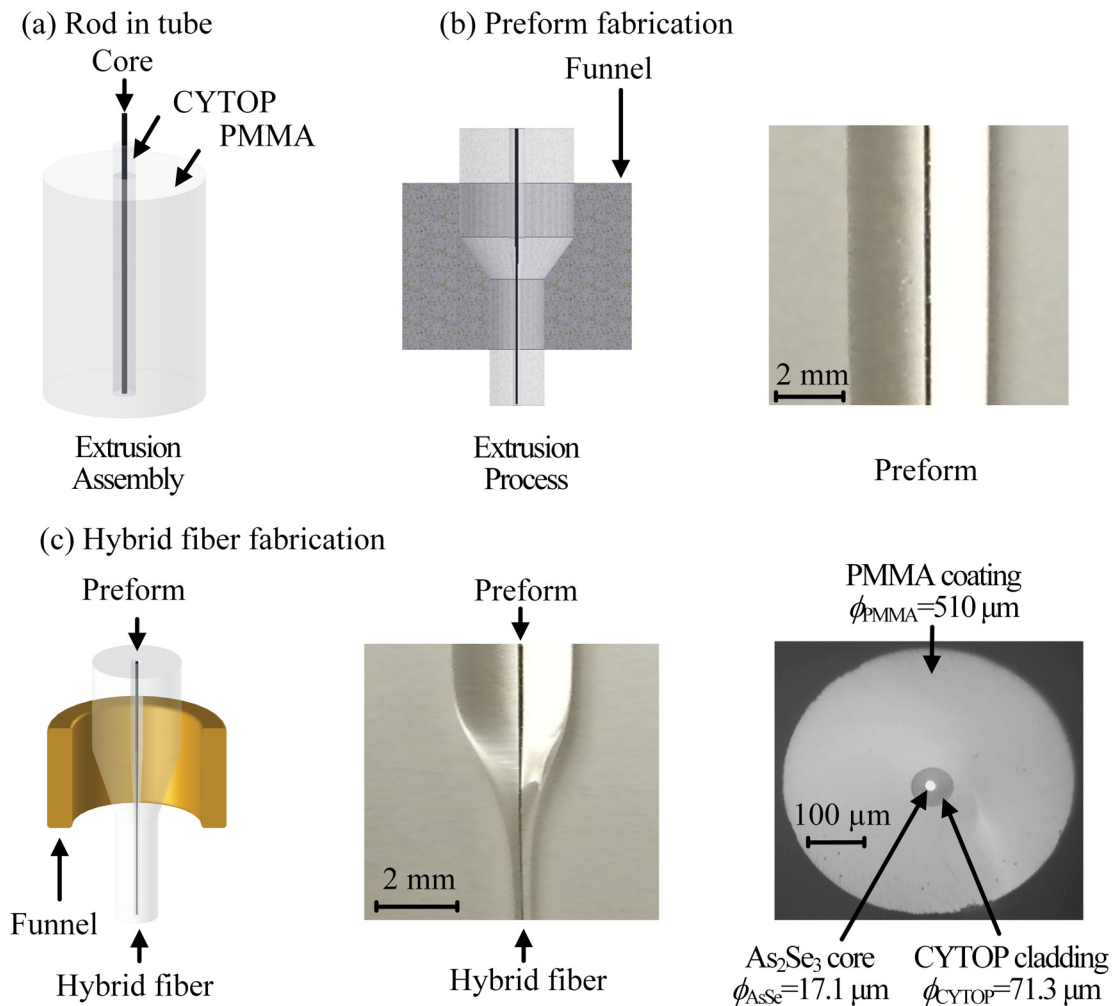


Fig. 4.6 Fabrication of a polymer-cladded As_2Se_3 fiber. (a) Schematic of the rod-in-tube method used to prepare the extrusion assembly. (b) Schematic of the CYTOP-cladded preform fabrication setup (left) and a photograph of extruded preform (right). (c) Schematic of the CYTOP-cladded fiber fabrication setup (left), photograph of fiber drawing (middle) and an optical reflection photograph of cross section (right).

The microwire is fabricated from a sample of fiber tapered using a heat brush method [172], then transferred to a butt-coupling setup. The input end of the microtaper is aligned and connected to SMF-28 fiber using UV-cured epoxy. Figure 4.7(a) shows the schematic of a microtaper subdi-

vided into fiber, transition and microwire sections. Figure 4.7(b) is the photograph of a microtaper with wire section length of 5 cm.

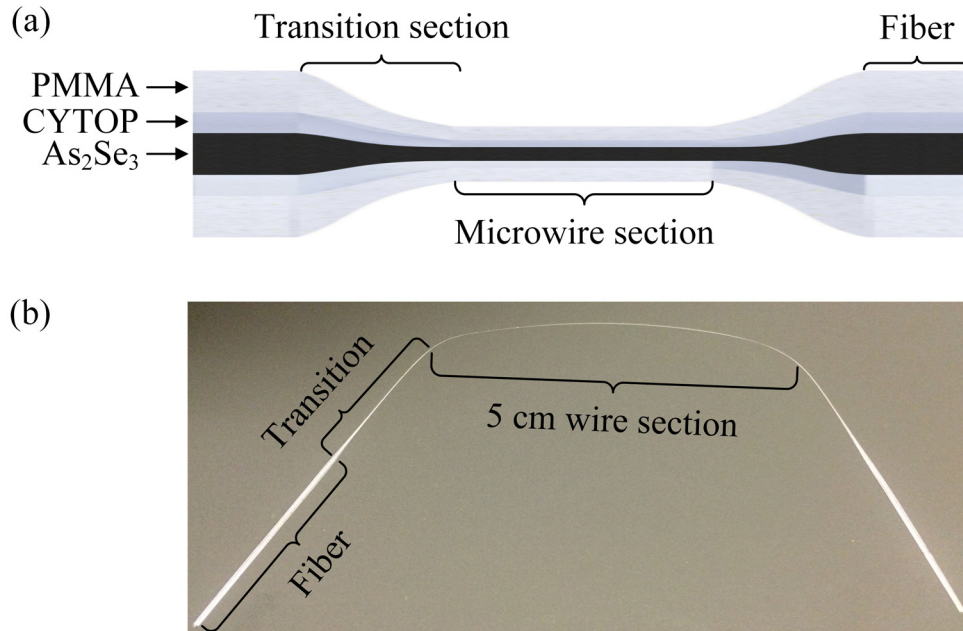


Fig. 4.7 Schematic of the CYTOP-cladded As_2Se_3 microtaper (not to scale). (b) Photograph of a microtaper with wire section length of 5 cm.

4.5 Results and discussion

The transmission loss spectrum of an As_2Se_3 microwire cladded with CYTOP is investigated experimentally. Figure 4.8(a) and (b) show the schematic of CYTOP-cladded As_2Se_3 microtaper and the setup for measuring the transmission loss, respectively. For the purpose of referencing, the transmittance of microwires cladded with hydrogen-based polymers that are COP 1020R and PMMA is also performed [147]. All microwires studied have a length of 5 cm and modal confinement factor $\Gamma=99\%$. This value of confinement factor is typical for nonlinear parametric processes because it leads to advantageous levels of group-velocity dispersion parameters (β_2 and β_4) while still leading to observable absorption characteristics of the cladding material. To result into $\Gamma=99\%$, the core diameter of CYTOP-, COP- and PMMA-cladded microwires are adjusted to $\phi_{\text{CYTOP}}=1.35 \mu\text{m}$, $\phi_{\text{COP}}=1.48 \mu\text{m}$ and $\phi_{\text{PMMA}}=1.46 \mu\text{m}$. The optical transmission loss of the microwires is measured at wavelengths in between $1.3 \mu\text{m}$ and $2.5 \mu\text{m}$ using a silica-based SC source

and an optical spectrum analyzer at either side of the device under test.

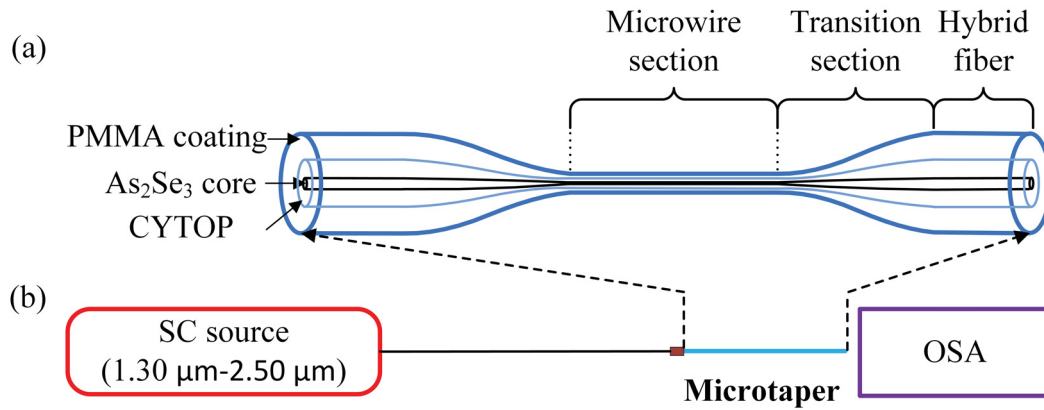


Fig. 4.8 (a) Schematic of the CYTOP-cladded As_2Se_3 microtaper. (b) Setup for transmission loss measurement.

Figure 4.9 shows the transmission loss of CYTOP-, COP- and PMMA-cladded As_2Se_3 microwires. The microwire with CYTOP cladding is transparent to light at wavelengths up to $>2.5 \mu\text{m}$, limited by the spectral range of the spectrum analyzer, without trace of absorption peaks from $1.3 \mu\text{m}$ to $2.5 \mu\text{m}$. Throughout this wavelength range, the transmission loss is stable between 0.11 dB/cm and 0.22 dB/cm . The main source of this uniform loss is the As_2Se_3 glass purity, which lies close to the state-of-the-art purity available. In contrast, the COP-cladded microwire reaches a transmission loss of 3 dB at $2.13 \mu\text{m}$ with traces of two absorption peaks at $\sim 1.72 \mu\text{m}$ and $\sim 1.76 \mu\text{m}$ due to the second order vibrational transition of C-H bonds. The transmission loss remains between 0.22 dB/cm and 0.83 dB/cm in the $1.30\text{-}2.25 \mu\text{m}$ range. Finally, the PMMA-cladded microwire reaches a transmission loss of 3 dB at a wavelength of $2.10 \mu\text{m}$ with traces of an absorption peak at $\sim 1.65 \mu\text{m}$ due to the second order vibrational transition of C-H bonds. The transmission loss remains between 0.30 dB/cm and 0.83 dB/cm from $1.30 \mu\text{m}$ to $2.20 \mu\text{m}$. The transmission loss of the CYTOP-cladded microwire is therefore substantially decreased with respect to COP- and PMMA-cladded microwires, especially at wavelengths in excess of $1.65 \mu\text{m}$.

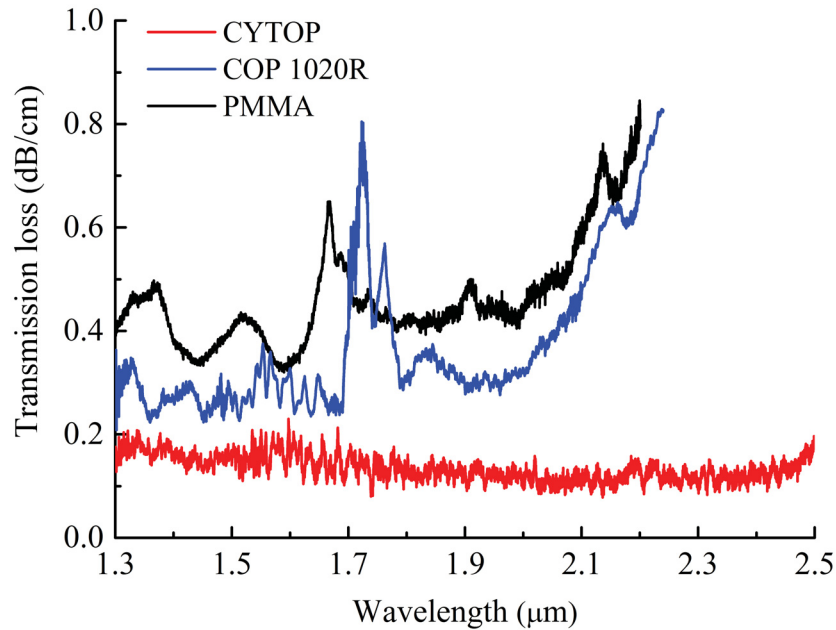


Fig. 4.9 Transmission loss spectra of CYTOP-, COP 1020R-, and PMMA-cladded As_2Se_3 microwires.

Nonlinear parametric processes in a CYTOP-cladded As_2Se_3 microwire are also investigated. Figure 4.10 shows the setup for Raman-enhanced FWM. The microwire has a length $L_w=5$ cm and core diameter $\phi=1.35$ μm , leading to $\gamma=27$ $\text{W}^{-1}\text{m}^{-1}$, $\beta_2=-0.273$ ps^2/m and $\beta_4=-1.17\times 10^{-5}$ ps^4/m . Taking into account a scattering loss of 0.15 dB/cm at a wavelength of 1.94 μm . Pump pulses centered at a wavelength of 1.94 μm with a duration of 3.5 ps after pulse shaping by a band-pass filter are launched into the microwire. Figure 4.11 shows spectra collected at the output of the microwire. As the coupled pump peak (average) power is increased up to 13.3 W (1.4 mW), side lobes of increasing power are observed along with spectral broadening of the pump signal. The nonlinear processes observed include SPM of the pump, but also Raman-enhanced FWM [59]; itself mixing with the pump to provide several orders of degenerate FWM.

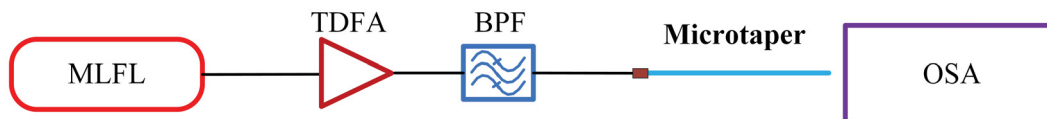


Fig. 4.10 Setup for Raman-enhanced FWM generation. MLFL: mode-locked fiber laser; TDFA: thulium-doped fiber amplifier; BPF: bandpass filter; OSA: optical spectrum analyzer.

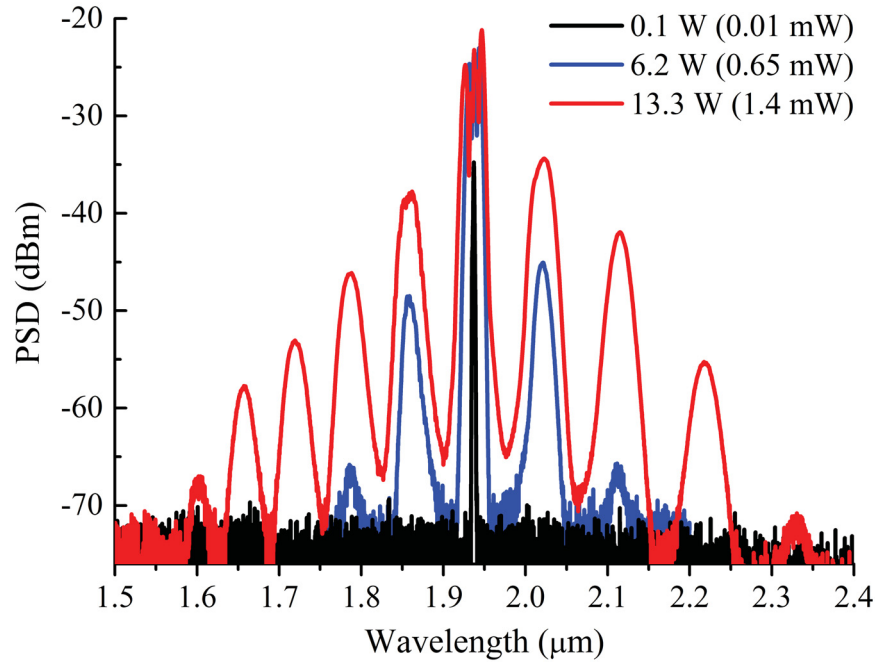


Fig. 4.11 Nonlinearly broadened spectra of CYTOP-cladded As_2Se_3 microwire at various pump powers. The legend presents corresponding coupled peak (average) powers.

SC generation in a CYTOP-cladded As_2Se_3 microwire is also investigated. Figure 4.12 shows the experimental setup for SC generation. The design includes a microwire with a length of $L_w=10$ cm and $\phi=1.55$ μm , leading to $\beta_2=-0.04$ ps^2/m , $\beta_3=0.003$ ps^3/m , $\beta_4=-0.09 \times 10^{-4}$ ps^4/m and $\gamma=21$ $\text{W}^{-1}\text{m}^{-1}$. The butt-coupling loss from SMF-28 fiber to the hybrid fiber is 1.1 dB, including 0.5 dB of Fresnel reflection loss at the fiber interface, and the rest due to mode-mismatch losses. Pump pulses centered at 1.94 μm with a duration of 3.0 ps are launched into the microwire and analyzed using a Fourier Transform Infrared Spectrometer (FTIR). As pump pulses are launched into the microwire, MI triggers the SC generation, breaking the input picosecond pulses into femtosecond sub-pulses, followed by soliton dynamics [57]. Figure 4.13 shows experimentally measured spectra as a function of the coupled pump power up to 1044 W (100 mW) in peak (average) power. A SC is generated, spanning from 1.0 μm to 4.3 μm at -30 dB relative to the peak value. A dip within the SC spectrum in the 2.5-3.0 μm spectral range could be caused by low pressure water vapour inside the FTIR [173]. The limited extent of the SC at wavelengths beyond 4.3 μm is expected to be caused by absorption from the second order vibrational overtone of the C-F bonds in CYTOP. Take note that the microwire length of 10 cm was chosen to emphasize the absorp-

tion features in the microwire and that a microwire of a few millimeters would provide sufficient nonlinearity and dispersion for SC generation with a reduced absorption signature by the cladding [5].

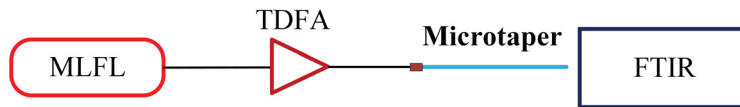


Fig. 4.12 Setup for SC generation. MLFL: mode-locked fiber laser; TDFA: thulium-doped fiber amplifier; BPF: bandpass filter; FTIR: Fourier Transform Infrared Spectrometer.

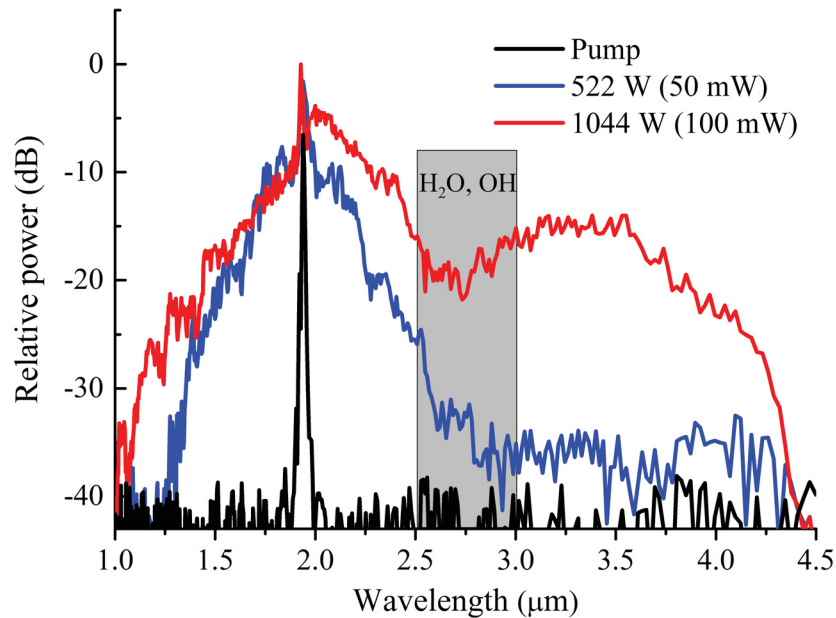


Fig. 4.13 SC spectra at various coupled pump powers for a CYTOP-cladded microwire with an As_2Se_3 core diameter of $1.55 \mu\text{m}$.

At last, SC generation is compared for CYTOP- and COP-cladded microwires with core diameters of $1.55 \mu\text{m}$ and $1.59 \mu\text{m}$, respectively. Those core diameters were chosen as they both lead to $\beta_2 = -0.04 \text{ ps}^2/\text{m}$ at the pump wavelength of $1.94 \mu\text{m}$. Both microwires are 10 cm long and pumped at 1044 W (100 mW) in peak (average) power. Figure 4.14 shows the resulting SC spectra. The SC spectrum of COP-cladded microwire is limited to $2.3 \mu\text{m}$ due to the strong absorption features of this hydrogen-based polymer, as observed in Fig. 4.9 [95].

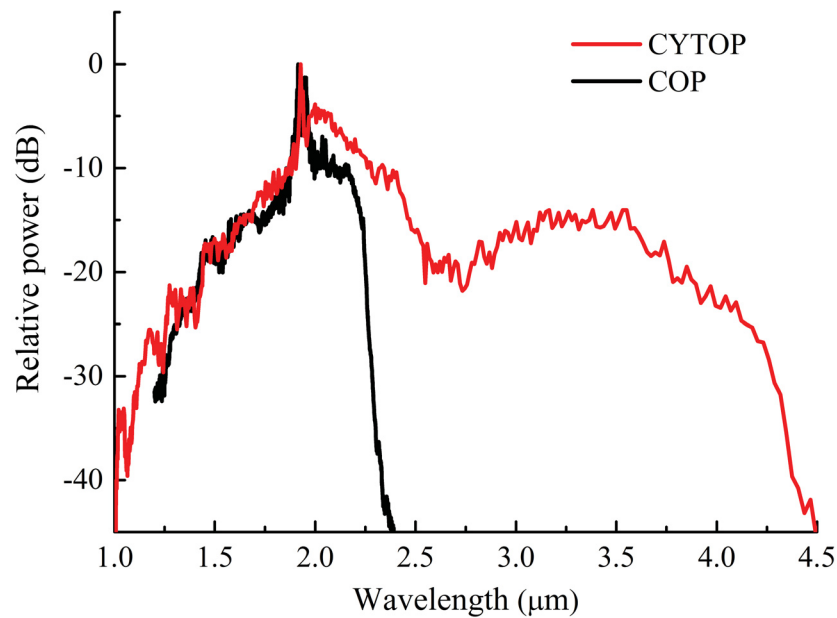


Fig. 4.14 SC spectra of CYTOP- and COP-cladded microwires at a peak (average) pump power of 1044 W (100 mW).

4.6 Conclusion

We have shown that fluorine-based CYTOP preserves the linear and nonlinear functionalities of As_2Se_3 microwires at wavelengths from 1.3 μm up to $>4.3 \mu\text{m}$. The CYTOP cladding significantly improves the transmission bandwidth with respect to hydrogen-based polymer claddings, especially at wavelengths above 1.65 μm . The CYTOP-cladded microwire has an engineerable group-velocity dispersion in the 1-7 μm wavelength range, enabling anomalous, normal, or zero dispersion. For the SC generation demonstrations, the microwire length of 10 cm was chosen to emphasize the absorption features in the microwire. In practice, a microwire design of a few millimeters would provide sufficient nonlinearity and dispersion for SC generation with a reduced absorption signature by the cladding.

Chapter 5

Mid-infrared wavelength conversion from As_2Se_3 microwires

5.1 Introduction

MIR sources are in strong demand for medical, scientific, spectroscopic, and defense applications [38, 42, 43]. Research efforts have intensified toward the development of compact and robust MIR sources, such as fiber-based OPOs, all-fiber SC sources and optical wavelength converters [56, 57, 59]. Most fiber lasers developed up to date rely on rare-earth doped silica fibers and operate at wavelengths up to $\sim 2 \mu\text{m}$, limited by the transparency window of fused silica [174, 175]. Rare-earth fiber lasers compatible at longer wavelengths toward the MIR emerge gradually, including erbium-doped ZBLAN sources with emission in the range of wavelengths of $2.80 \mu\text{m}$, $2.94 \mu\text{m}$, and $3.44 \mu\text{m}$ [176–178]. It is expected that the combination of such sources with an appropriate nonlinear medium would result into broadly tunable sources, in analogy to what is performed with state-of-the-art solid-state lasers.

ChG glasses are well known to provide transparency at wavelengths up to $12 \mu\text{m}$ and a high nonlinearity (n_2) up to $2.4 \times 10^{-17} \text{ m}^2/\text{W}$ [2, 179]. The ZDWs of bulk ChG glasses (As_2Se_3 and As_2S_3) are in the MIR, i.e. $\sim 7 \mu\text{m}$ for As_2Se_3 and $\sim 5 \mu\text{m}$ for As_2S_3 . Chromatic dispersion can, however, be engineered in ChG waveguides in order to slide the ZDW towards shorter wavelengths and taking advantage of nonlinear effects [7, 13, 147, 172]. Using ChG microwires, the ZDW has been shifted at wavelengths for which compact pump laser sources (e.g. semiconductor lasers and rare-earth doped fiber lasers) are available, thereby providing an easy access to nonlinear paramet-

ric processes, such as SC generations [14, 147], wavelength conversions [22, 23, 180], and optical parametric oscillations [20, 181]. Further in the MIR, a 14 cm long As_2Se_3 -PMMA microwire pumped by a 10 W solid-state OPO at a wavelength of 2.6 μm generated MI with frequency detuning of 30 THz (Stokes at 3.5 μm and anti-Stokes at 2.0 μm) [29]. A number of other materials have also been used to demonstrate normal dispersion FWM or MI with frequency detuning up to ~ 10 THz [182–184]. However, there is potential for greatly improving the technical specifications of all-fiber MIR wavelength converters in terms of frequency detuning, tunability and conversion efficiency.

In this chapter, we demonstrate all-fiber and far-detuned MIR wavelength conversion from As_2Se_3 microwires. Two experiments are presented to highlight the great potential of ChG microwires for the fabrication of MIR sources. Both experiments make use of a mode-locked fiber laser centered at a wavelength of 1.939 μm . In a first experiment, an idler is generated and tuned from 2.351 μm to >2.500 μm resulting from wavelength tuning of a probe from 1.650 μm to 1.587 μm , via normal dispersion FWM in a 0.5 cm long microwire. In a second experiment, tunable sidebands up to 2.845 μm are generated via MI in the normal dispersion regime of a 10 cm long As_2Se_3 microwire. In that experiment, the frequency detuning of 49.3 THz represents the largest reported in soft glass materials.

5.2 Theory

Figure 5.1 shows the schematic of a microtaper. The microtaper is subdivided into a microwire, into which nonlinear processes take place, a transition section where the profile of the propagating mode is converted adiabatically, and a hybrid fiber section designed to enable efficient coupling from/to a typical low numerical aperture fiber such as SMF-28. The 0.5 cm long microwire is made out of an As_2Se_3 core, a CYTOP cladding and a PMMA coating [180], and fabricated using the method described in [172]. The fluorine-based CYTOP polymer is transparent to wavelengths up to >2.5 μm [180]. The low refractive index of CYTOP (1.33 at 1.939 μm [167]) makes a large refractive index contrast with respect to As_2Se_3 (2.81 at 1.939 μm [2]), thus strongly confining the propagating mode inside the microwire and enabling a large nonlinear coefficient. For a microwire core dimension in the order of the wavelength, the large refractive index contrast is also responsible for the dominant term of chromatic dispersion, namely, waveguide dispersion. For this reason, the CYTOP-cladded microwire can be set to anomalous, normal or zero dispersion in 1-7 μm wavelength range by an appropriate choice of the core diameter.

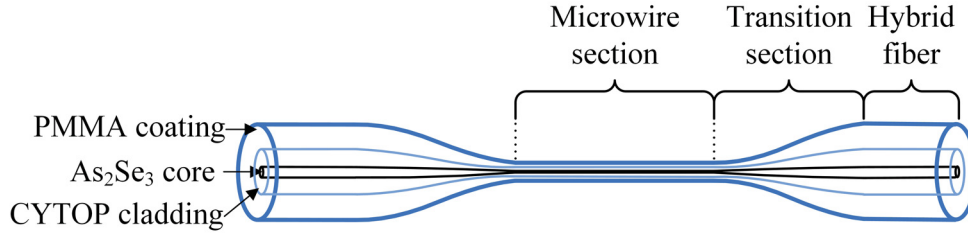


Fig. 5.1 Schematic of the As₂Se₃-CYTOP microtaper.

The FWM evolution of a picosecond pump and generated idler can be modeled by solving coupled-wave equations provided by the nonlinear Schrödinger equation. This calculation neglects pulse broadening and pulse temporal walk-off due to group velocity dispersion (GVD) given that the physical length of a microwire is much shorter than the walk-off length and dispersion length [59, 185, 186]

$$\frac{dA_p}{dz} = i(\gamma_p P_p + 2\gamma_{ps} P_s + 2\gamma_{pi} P_i)A_p + 2i\gamma_{pspi} A_s A_i A_p^* e^{i\Delta k z} - \alpha_p A_p / 2 \quad (5.1)$$

$$\frac{dA_s}{dz} = i(\gamma_s P_s + 2\gamma_{sp} P_p + 2\gamma_{si} P_i)A_s + i\gamma_{spip} A_p A_p A_i^* e^{-i\Delta k z} - \alpha_s A_s / 2 \quad (5.2)$$

$$\frac{dA_i}{dz} = i(\gamma_i P_i + 2\gamma_{ip} P_p + 2\gamma_{is} P_s)A_i + i\gamma_{ipsp} A_p A_p A_s^* e^{-i\Delta k z} - \alpha_i A_i / 2 \quad (5.3)$$

The first term on the right of the above equations represents the SPM effect, where γ_p , γ_s , and γ_i are the waveguide nonlinearity parameter at the pump wavelength, signal wavelength and idler wavelength, respectively. P_p , P_s , and P_i are the pump power, signal power and idler power, respectively. The second term and third term represent the XPM effects between pump and signal, pump and idler, and signal and idler, where $\gamma_{ps} = \gamma_{sp}$, $\gamma_{pi} = \gamma_{ip}$, and $\gamma_{is} = \gamma_{si}$ represent the waveguide nonlinearity parameters. The fourth term represents the FWM effect, where γ_{pspi} , γ_{spip} , and γ_{ipsp} are the waveguide nonlinearity parameters. The fifth term represents the attenuation effect, where α_p , α_s , and α_i are the attenuation coefficients at pump wavelength, signal wavelength and idler wavelength, respectively. Δk is the linear phase mismatch given by [59]

$$\Delta k = \frac{n(\omega_i)\omega_i + n(\omega_s)\omega_s - 2n(\omega_p)\omega_p}{c} \quad (5.4)$$

where ω_i , ω_s , ω_p are the angular frequencies of the idler, signal and pump waves, respectively; $n(\omega_i)$, $n(\omega_s)$, $n(\omega_p)$ are the effective refractive indices at ω_i , ω_s , ω_p , respectively; c is the light

velocity in vacuum.

In Eqs.5.1-5.3, $\gamma_m \equiv \gamma_{mmmm}$ and $\gamma_{mn} \equiv \gamma_{mnmn}$ ($m, n=p, s, i$ and $m \neq n$), respectively. These waveguide nonlinearity parameters together with those for FWM effect are defined in the following general form

$$\gamma_{ijkl}(-\omega_i; \omega_j, -\omega_k, \omega_l) = \frac{3\omega_i \eta_{ijkl}}{4\varepsilon_0 c^2 \bar{a} (n_i n_j n_k n_l)^{1/2}} \chi_{ijkl}^{(3)}(-\omega_i; \omega_j, -\omega_k, \omega_l) \quad (5.5)$$

where ε_0 is the vacuum permittivity, c is the velocity of light in vacuum, η_{ijkl} is the mode overlap defined in Eq.2.44, $n_v(\omega_v)$ ($v = i, j, k, l$) is the refractive index at ω_v , \bar{a} is the average effective mode area defined as

$$\bar{a} \equiv (a_i a_j a_k a_l)^{1/4} \quad (5.6)$$

where a_v ($v = i, j, k, l$) is the effective mode area at frequency ω_v and defined in Eq.2.8.

To generate FWM parametric gain over a wide conversion bandwidth, the phase-matching condition must be satisfied. The effective phase mismatch is given by [59]

$$\kappa = 2\gamma P_0 + \Delta k; \quad (5.7)$$

where $2\gamma P_0$ is the nonlinear phase mismatch, induced by Kerr effect, where γ and P_0 are the waveguide nonlinearity parameter and peak pump power, respectively. Δk is the linear phase mismatch give in Eq. 5.4. The achievement of a broad conversion bandwidth requires a far-detuned phase mismatch that is low or zero. It would thus be an asset that the nonlinear medium that serves for this wavelength conversion also has engineerable dispersion characteristics. ChG microwires have a dispersion level that can be adjusted from an appropriate choice of geometry. Figure 5.2(a), figure 5.2(b) and figure 5.2(c) respectively show second order chromatic dispersion β_2 , fourth order chromatic dispersion β_4 , and sixth order chromatic dispersion β_6 as a function of core diameter of As₂Se₃ microwire and wavelength.

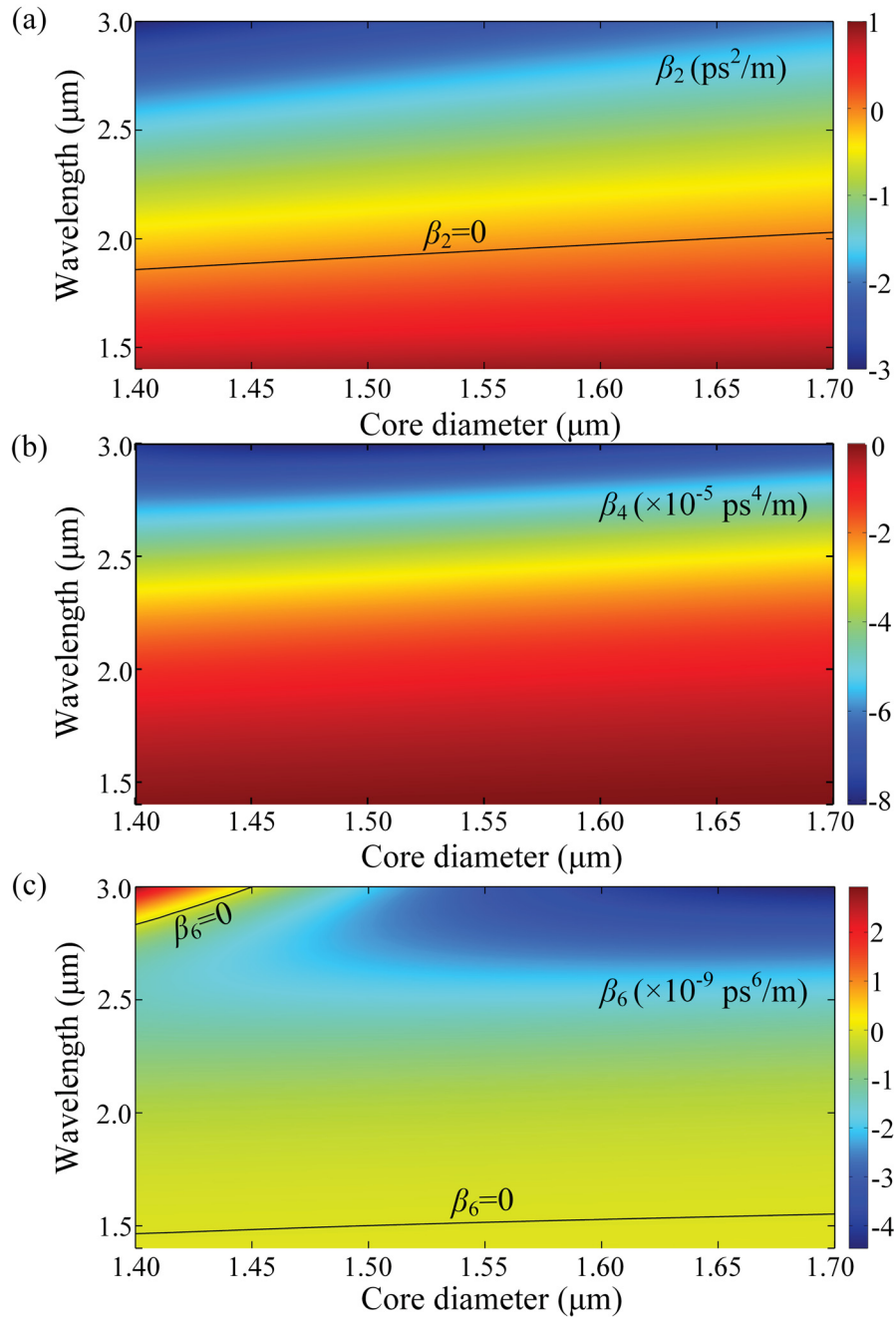


Fig. 5.2 (a) β_2 as a function of wavelength and As₂Se₃ microwire core diameter. (b) β_4 as a function of wavelength and As₂Se₃ microwire core diameter. (c) β_6 as a function of wavelength and As₂Se₃ microwire core diameter.

The phase-matched parametric wavelengths are evaluated from solving Eq. 5.7 while setting

$\kappa = 0$. Figure 5.3 shows the phase-matched parametric wavelengths as a function of core diameter of As₂Se₃ microwire at an operation wavelength of 1.939 μm for three different pump powers. When the pump wavelength is set into anomalous dispersion, parametric wavelengths remain relatively close to the pump wavelength and depend mostly on the group velocity dispersion β_2 . However pumping in normal dispersion leads to parametric wavelengths that are widely spaced from the pump wavelength and depend strongly on the higher order dispersion values. In both cases, as the pump power is increased, the nonlinear phase mismatch increases. As a result, the phase-matched parametric wavelengths shift further away from the pump wavelength as described in Eq. 5.7 and shown in fig. 5.3.

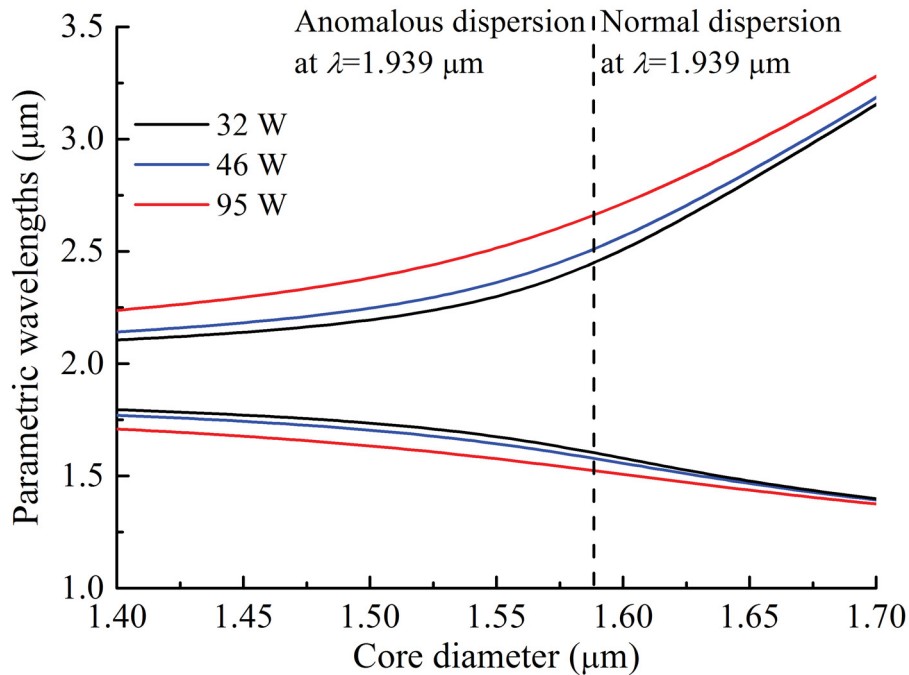


Fig. 5.3 Phase-matched parametric wavelengths as a function of As₂Se₃ microwire core diameter. The pump wavelength is set at 1.939 μm and the peak pump power is set at 32 W, 46 W and 95 W. The dotted line indicates the zero dispersion diameter at the pump wavelength. The microwire design includes a CYTOP cladding.

The microwire design selected for both experiments explained next includes a 2 cm long input/output hybrid fiber section with an As₂Se₃ core diameter of 17.1 μm , a CYTOP cladding diameter of 71.3 μm , and a PMMA coating diameter of 510 μm , a 2.3 cm long input/output transition section, and a microwire section with a core diameter $\phi=1.625$ μm . This value leads to positive β_2

($\beta_2=3.192\times 10^{-2}$ ps²/m), negative β_4 ($\beta_4=-8.089\times 10^{-6}$ ps⁴/m) and negative β_6 ($\beta_6=-2.797\times 10^{-10}$ ps⁶/m), enabling a good phase-matching condition over a large range of wavelengths. The resulting waveguide nonlinear coefficient γ is 19.7 W⁻¹m⁻¹.

5.3 FWM experiment

In a first experiment, the stimulated FWM process in a 0.5 cm long As₂Se₃ microwire is investigated. This length has been chosen because it ensures that the microwire section has a constant diameter, without significant random fluctuations. Figure 5.4 schematizes the setup used for the pump-probe experiment. Pump pulses with a duration of 800 fs from a mode-locked fiber laser and centered at a wavelength of 1.939 μ m are launched into the microwire at a repetition rate of 30 MHz. The pulses are previously broadened up to a duration of \sim 3.5 ps after passing through a bandpass filter with a bandwidth of 1.9 nm to increase the walk-off length. A probe signal provided by a tunable cw laser (1.490-1.650 μ m) is also coupled into the microwire via a fiber coupler. A polarization controller ensures that the polarized probe couples with the polarization state of the MLFL. Output spectra are recorded using an optical spectrum analyzer (OSA).

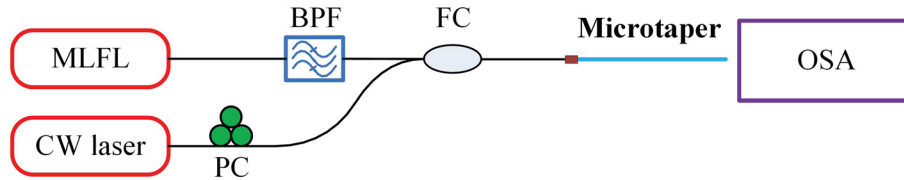


Fig. 5.4 Schematic of the pump-probe FWM setup. MLFL: mode-locked fiber laser; BPF: bandpass filter; FC: fiber coupler; PC: polarization controller; OSA: optical spectrum analyzer.

Figure 5.5(a) shows a series of idler spectra resulting from wavelength tuning of the probe from 1.587 μ m to 1.650 μ m with a power of 0.54 mW. The pump wavelength is centered at 1.939 μ m with a peak power of 3.5 W. The idler slides in wavelength from 2.494 μ m to 2.351 μ m under the influence of the tuning probe. The measured FWM conversion bandwidth is limited at the lower limit by the maximum wavelength of the probe and on the upper limit by the spectral range of OSA of 2.500 μ m. Figure 5.5(b) shows the conversion efficiency (CE), defined as the output peak idler power over the input probe power. The output peak idler power is calculated using the average output power, repetition rate and pulse duration. The theoretical CE is evaluated from solving

Eqs. 5.1-5.3. Those equations are valid for describing the FWM processes under the assumption of negligible walk-off and GVD effects. With 3.5 ps pump pulses in a 0.5 cm long microwire, the physical length is much shorter than the walk-off length (2.4 cm at $\lambda=2.5 \mu\text{m}$) and dispersion length (1.4 m at $\lambda=1.939 \mu\text{m}$). Error bars take into account cumulative uncertainties on pulse duration, coupling loss, and OSA background noise.

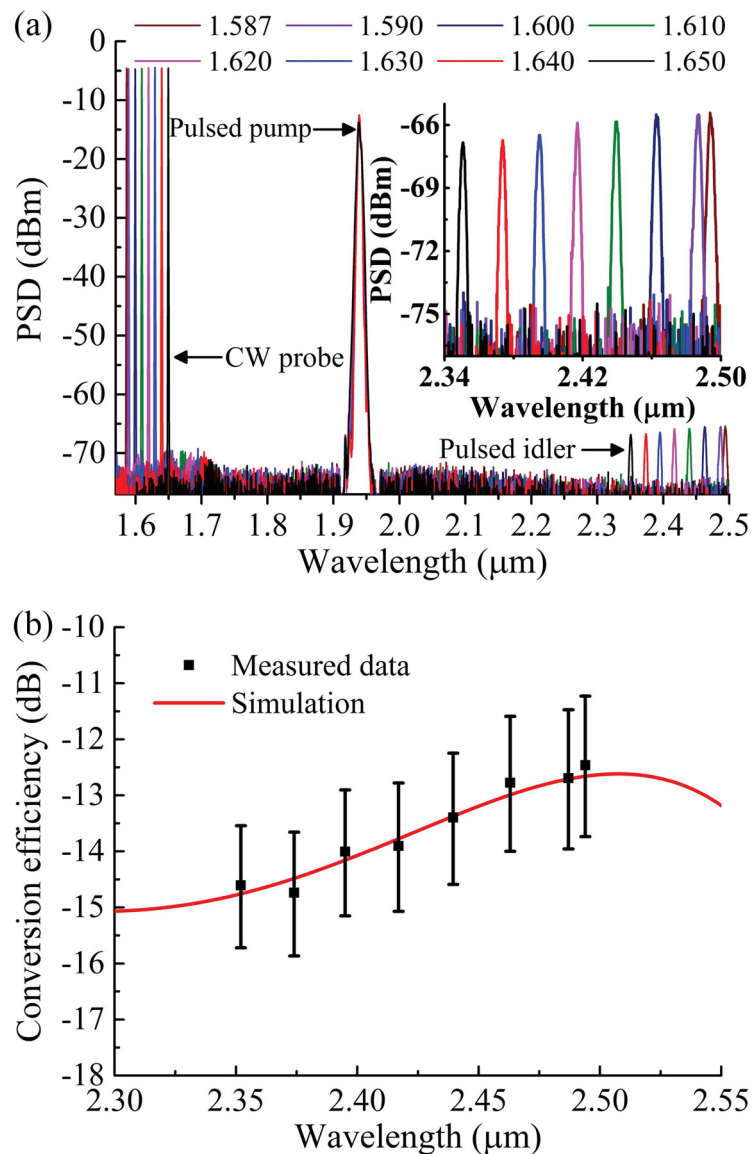


Fig. 5.5 (a) Measured output spectra. The legend presents corresponding probe wavelengths. The inset graph shows the zoomed-in spectra of the output idlers. (b) Conversion efficiency versus idler wavelength.

Figure 5.6(a) shows the peak idler power as a function of probe power in the As_2Se_3 microwire with a fixed peak pump power of 3.5 W and a fixed input probe wavelength of $1.587 \mu\text{m}$. The measurement is in good agreement with simulation results. Figure 5.6(b) shows the peak idler power as a function of peak pump power with fixed input probe wavelength and power of $1.587 \mu\text{m}$ and 0.54 mW, respectively. Again, the measurement agrees well with simulation results. The idler power can be further increased by increasing the pump power since there is no sign of saturation. Alternatively, the idler power can be further enhanced by employing a longer microwire.

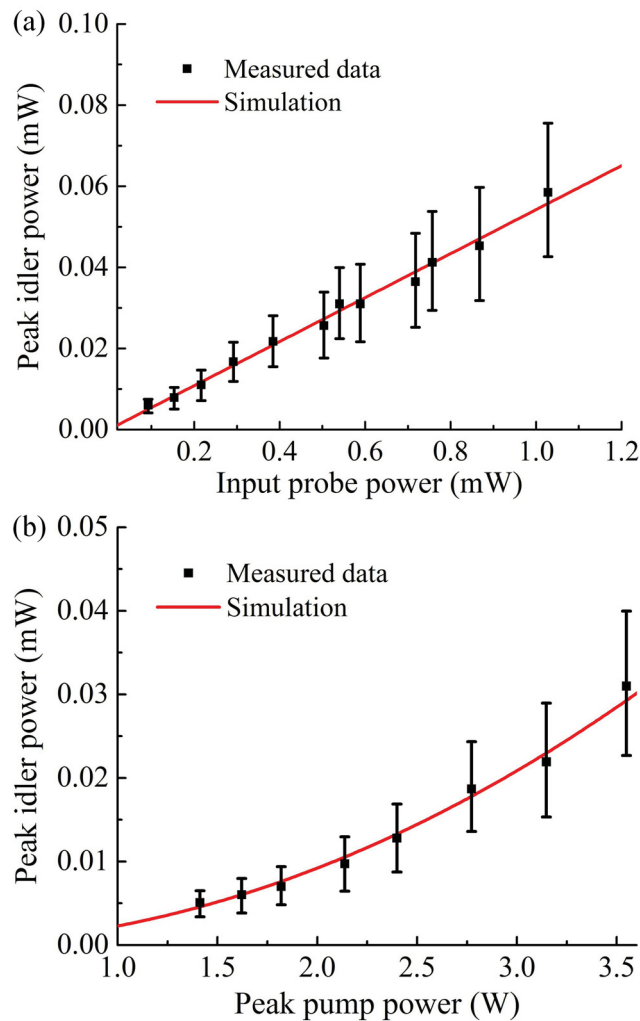


Fig. 5.6 (a) The output peak idler power as a function of input probe power at a fixed peak pump power $P_0=3.5$ W and a fixed input probe wavelength of $1.587 \mu\text{m}$. (b) The output peak idler power as a function of peak pump power at a fixed input probe wavelength and power of $1.587 \mu\text{m}$ and 0.54 mW, respectively.

5.4 MI experiment

In a second experiment, single pump MIR wavelength conversion via normal dispersion MI in an As₂Se₃ microwire is investigated. The microwire has a core diameter $\phi=1.625\ \mu\text{m}$, a propagation loss $\alpha=0.12\ \text{dB/cm}$, and a length $L_w=10\ \text{cm}$. This length is chosen to preserve the walk-off length relative to the microwire length. Figure 5.7 schematizes the experimental setup. The mode-locked fiber laser emits pulses centered at a wavelength of $1.939\ \mu\text{m}$ with a duration of 800 fs and repetition rate of 30 MHz. The laser output is launched into a 100 m long single mode fiber to temporally broaden the pulses to 25.3 ps and increase the walk-off length (10 cm between pump wavelength of $1.939\ \mu\text{m}$ and Stokes wavelength of $2.692\ \mu\text{m}$). The broadened pulses are passed through subsequent two-stage thulium-doped fiber amplifiers to enhance the output power. The amplified pulses are launched into the As₂Se₃ microwire and output spectra are recorded using a Fourier Transform Infrared Spectrometer.

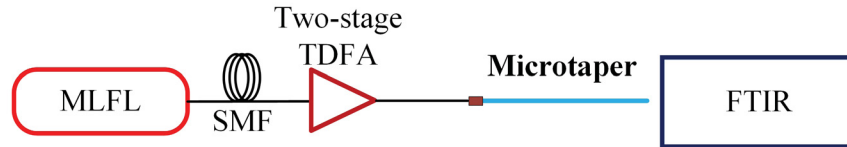


Fig. 5.7 Experimental setup. MLFL: mode-locked fiber laser; TDFA: thulium-doped fiber amplifier; FTIR: Fourier Transform Infrared Spectrometer.

Figure 5.8(a) shows the output spectra of the microwire at various pump powers. The newly generated Stokes and anti-Stokes emissions are observed, widely and equally separated from the pump in the frequency domain. As the pump power launched into the microwire is increased, the anti-Stokes and Stokes bands experience a shift towards shorter and longer wavelengths, respectively. The anti-Stokes signals are generated from $1.468\ \mu\text{m}$ to $1.521\ \mu\text{m}$, and the corresponding Stokes signals are generated from $2.845\ \mu\text{m}$ to $2.668\ \mu\text{m}$. When the peak pump power is set to 95 W, the corresponding Stokes and anti-Stokes bands are centered at $2.845\ \mu\text{m}$ and $1.468\ \mu\text{m}$, respectively. These two bands are symmetric in the frequency domain with a frequency shift $\Omega/2\pi=49.3\ \text{THz}$. To our knowledge, this is the largest frequency shift generated by MI in soft glass materials.

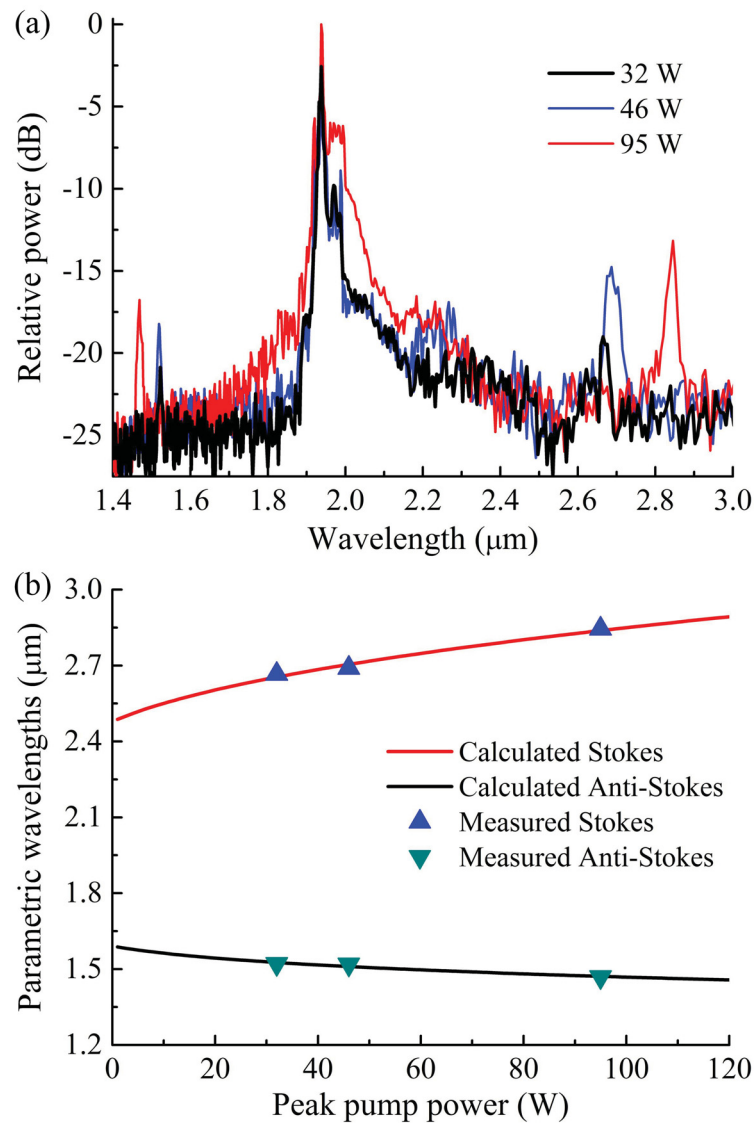


Fig. 5.8 (a) Measured output spectra of MI of an As_2Se_3 microwire with a core diameter of 1.625 μm and a length of 10 cm. (b) Measured and calculated parametric wavelengths as a function of peak pump power.

Figure 5.8(b) shows the measured and calculated parametric wavelengths as a function of peak pump power. The experimental results are in good agreement with calculated parametric wavelengths from the phase-matching condition described in Eq. 5.7. The wavelength shift can be further increased by either increasing the pump power or tuning the pump to shorter wavelengths. The power of parametric bands can be further enhanced by either increasing the pump power or

employing a longer microwire combined with longer pump pulses to preserve the walk-off length relative to the microwire length.

5.5 Conclusion

In summary, we have shown all-fiber parametric amplification- and MI-based MIR wavelength conversions from As₂Se₃ microwires, showing frequency conversion up to 49.3 THz. In the case of parametric amplification, the idlers are generated from 2.351 μm to 2.500 μm in a 0.5 cm As₂Se₃ microwire via a pump-probe scheme. In the case of MI, the widely spaced Stokes and anti-Stokes bands are generated with a frequency shift as large as 49.3 THz. The measured pump power dependence of parametric wavelengths is demonstrated and in good agreement with calculated results. The flexibility to generate parametric gain over a wide frequency range via normal dispersion parametric amplification and MI demonstrates the excellent potential of ChG microwires to provide far-detuned MIR wavelength converters and OPOs.

Chapter 6

Conclusion

In this thesis, hydrogen-based polymers, including PC and COP, and fluorine-based polymer, CYTOP, have been successfully demonstrated as the cladding materials for ChG microwires. Subsequently, the applications of those microwires have been presented. Firstly, we compare the optical transmission characteristics of PMMA-, PC-, COP-cladded As_2Se_3 microwires. For this purpose, PMMA-, PC-, and COP-cladded As_2Se_3 microtapers with wire length of 10 cm and wire section diameter of $1.5 \mu\text{m}$ are fabricated, and the infrared transmission spectra are measured and analyzed. The design rules and fabrication technique of each polymer-cladded microwire is provided. Relative to PMMA-cladded microwires, microwires cladded with PC and COP provide an increased transmission window. However, due to the strong absorption of C-H bonds, the transmission of a PC-cladded As_2Se_3 microwire with wire length of 10 cm is limited to an upper bound of $2.1 \mu\text{m}$. The COP 480R- and COP 1020R-cladded As_2Se_3 microwires with wire length of 10 cm transmit light up to at least $2.2 \mu\text{m}$. The transmission window of these microwires can be further extended by reducing the wire length. Secondly, we compare the optical transmission characteristic of CYTOP-cladded As_2Se_3 microwire with that of PMMA- and COP-cladded microwires. For this purpose, CYTOP-, COP-, and PMMA- cladded As_2Se_3 microtapers with identical wire length of 5 cm and identical confinement factor of 99 % are fabricated, and the transmission spectra from $1.3 \mu\text{m}$ up to $>2.5 \mu\text{m}$ are measured. Compared with COP- and PMMA-cladded microwires, microwires cladded with CYTOP provide excellent transmission throughout this wavelength range without any trace of absorption peak. The Raman-assisted cascaded FWM effect has been demonstrated to show that CYTOP preserves the nonlinear functionalities of As_2Se_3 microwires at wavelengths from $1.3 \mu\text{m}$ up to $>2.5 \mu\text{m}$. A SC generation spanning from $1.0 \mu\text{m}$ to $>4.3 \mu\text{m}$ has

been shown in a CYTOP-cladded microwire with a core diameter of $1.55\ \mu\text{m}$ and a wire length of 10 cm. This length was chosen to emphasize the absorption characteristics in the microwire. In practice, a microwire design of a few millimeters would provide sufficient nonlinearity and dispersion for SC generation with a reduced absorption signature from the cladding. Finally, we have shown all-fiber parametric amplification- and MI-based MIR wavelength conversions from As_2Se_3 microwires, showing frequency conversion up to 49.3 THz. In the case of parametric amplification combining a pump at a wavelength of $1.939\ \mu\text{m}$ with a probe that is tunable in the L-band, an idler is generated and tuned from $2.351\ \mu\text{m}$ to $2.500\ \mu\text{m}$ in a 0.5 cm As_2Se_3 microwire via a pump-probe scheme. The measured conversion efficiency is demonstrated and in good agreement with simulation results evaluated from solving the coupled amplitude equations. The measured peak idler power as a function of input probe power and peak pump power is demonstrated and in good agreement with simulation results. In the case of MI, the widely spaced Stokes and anti-Stokes bands are generated with a frequency shift as large as 49.3 THz, the largest ever reported in soft glass materials. The pump power dependence of parametric wavelengths has been experimentally and theoretically investigated. The measured and calculated results agree well. The flexibility to generate parametric gain over a wide frequency range via normal dispersion parametric amplification and MI demonstrates the excellent potential of ChG microwires to provide far-detuned MIR wavelength converters and OPOs.

A number of projects based on the microwires developed in this thesis are currently under investigation or will be further investigated: Firstly, a good next step is to write Bragg gratings compatible with the MIR in ChG microwires. This could be achieved by adjusting the angle between the interfering beams in the FBG fabrication setup described in [24]. The resulting MIR compatible Bragg gratings can be used to form a low loss linear cavity. Secondly, a MIR compact ChG microwire-based distributed Bragg reflector OPO can be realized. The gain medium is a microwire with a core of As_2Se_3 and a cladding of CYTOP, leading to high nonlinear coefficient and optimized chromatic dispersion characteristics. The linear cavity will be formed by inscribing two Bragg gratings with high reflectivity in the CYTOP-cladded As_2Se_3 microwire, thus minimizing the cavity losses. As a result, the OPO will have a low threshold power and high slope efficiency. Thirdly, a MIR ChG microwire-based distributed Bragg reflector Raman laser with small footprint can be achieved. Resulting from the combination of high photosensitivity and high nonlinear refractive index of ChG glasses, the Raman gain medium and the cavity mirrors can be integrated in a single microwire by inscribing two Bragg gratings within the microwire. As a result, the cavity losses will be low, thus reducing the power threshold of the laser and improving the slope

efficiency.

References

- [1] G. Lenz, J. Zimmermann, T. Katsufuji, M. E. Lines, H. Hwang, S. Splter, R. E. Slusher, S. W. Cheong, J. S. Sanghera, and I. D. Aggarwal, "Large Kerr effect in bulk Se-based chalcogenide glasses," *Opt. Lett.*, vol. 25, no. 4, pp. 254–256, 2000.
- [2] Amorphous materials Inc., *AMTIR-2: Arsenic selenide glass As_2Se_3* , <http://www.amorphousmaterials.com/products/>.
- [3] Amorphous materials Inc., *AMTIR-6: Arsenic trisulfide glass AsS_3* , <http://www.amorphousmaterials.com/products/>.
- [4] V. G. Taed, N. J. Baker, L. Fu, K. Finsterbusch, M. R. E. Lamont, D. J. Moss, H. C. Nguyen, B. J. Eggleton, D. Y. Choi, S. Madden, and B. Luther-Davies, "Ultrafast all-optical chalcogenide glass photonic circuits," *Opt. Express*, vol. 15, no. 15, pp. 9205–9221, 2007.
- [5] A. Al-Kadry, C. Baker, M. El-Amraoui, Y. Messaddeq, and M. Rochette, "Broadband supercontinuum generation in As_2Se_3 chalcogenide wires by avoiding the two-photon absorption effects," *Opt. Lett.*, vol. 38, no. 7, pp. 1185–1187, 2013.
- [6] P. Dumais, F. Gonthier, S. Lacroix, J. Bures, A. Villeneuve, P. G. J. Wigley, and G. I. Stegeman, "Enhanced self-phase modulation in tapered fibers," *Opt. Lett.*, vol. 23, no. 23, pp. 1996–1998, 1993.
- [7] C. Baker and M. Rochette, "High nonlinearity and single-mode transmission in tapered multimode As_2Se_3 -PMMA fibers," *IEEE Photon. J.*, vol. 4, no. 3, pp. 960–969, 2012.
- [8] A. B. Seddon, "Chalcogenide glasses: a review of their preparation, properties and applications," *J. Non-Cryst. Solids*, vol. 184, pp. 44–50, 1995.
- [9] J. A. Savage, "Optical properties of chalcogenide glasses," *J. Non-Cryst. Solids*, vol. 47, no. 1, pp. 101–115, 1982.
- [10] A. V. Vasiliev, E. M. Dianov, V. G. Plotchenko, V. K. Sysov, A. M. Bagrov, P. I. Baikalov, G. G. Devyatikh, I. V. Scripchev, and M. F. Churbonavov, "Middle IR As-S and As-Se glass fibres with optical losses lower than 1 dB/m," *Electron. Lett.*, vol. 15, no. 19, pp. 589–590, 1983.

- [11] D. I. Yeom, E. C. Mägi, M. R. E. Lamont, M. A. F. Roelens, L. B. Fu, and B. J. Eggleton, “Low-threshold supercontinuum generation in highly nonlinear chalcogenide nanowires,” *Opt. Lett.*, vol. 33, no. 7, pp. 660–662, 2008.
- [12] D. D. Hudson, S. A. Dekker, E. C. Mägi, A. C. Judge, S. D. Jackson, E. Li, J. S. Sanghera, L. B. Shaw, I. D. Aggarwal, and B. J. Eggleton, “Octave spanning supercontinuum in an As_2S_3 taper using ultralow pump pulse energy,” *Opt. Lett.*, vol. 36, no. 7, pp. 1122–1124, 2011.
- [13] E. C. Mägi, L. B. Fu, H. C. Nguyen, M. R. E. Lamont, D. I. Yeom, and B. J. Eggleton, “Enhanced Kerr nonlinearity in sub-wavelength diameter As_2Se_3 chalcogenide fiber tapers,” *Opt. Express*, vol. 15, no. 16, pp. 10324–10329, 2007.
- [14] A. Al-Kadry, M. El-Amraoui, Y. Messaddeq, and M. Rochette, “Two octaves mid-infrared supercontinuum generation in As_2Se_3 microwires,” *Opt. Express*, vol. 22, no. 25, pp. 31131–31137, 2014.
- [15] M. Duhant, W. Renard, G. Canat, J. Trols, P. Toupin, L. Brilland, F. Smektala, A. Btourn, P. Bourdon, and G. Renversez, “Mid-infrared strong spectral broadening in microstructured tapered chalcogenide AsSe fiber,” *SPIE LASE*, p. 823735, 2012.
- [16] A. Marandi, C. W. Ruby, V. G. Plotnichenko, E. M. Dianov, K. L. Vodopyanov, and R. L. Byer, “Mid-infrared supercontinuum generation in tapered chalcogenide fiber for producing octave-spanning frequency comb around $3\ \mu\text{m}$,” *Opt. Express*, vol. 20, no. 22, pp. 24218–24225, 2012.
- [17] C. W. Ruby, A. Marandi, K. L. Vodopyanov, and R. L. Byer, “Octave-spanning supercontinuum generation in *in situ* tapered As_2S_3 fiber pumped by a thulium-doped fiber laser,” *Opt. Lett.*, vol. 38, no. 15, pp. 2865–2868, 2013.
- [18] C. Markos and O. Bang, “Nonlinear label-free biosensing with high sensitivity using As_2S_3 chalcogenide tapered fiber,” *J. Lightwave Technol.*, vol. 33, no. 13, pp. 2892–2898, 2015.
- [19] C. Baker and M. Rochette, “Highly nonlinear hybrid AsSe-PMMA microtapers,” *Opt. Express*, vol. 18, no. 12, pp. 12391–12398, 2010.
- [20] R. Ahmad and M. Rochette, “Chalcogenide optical parametric oscillator,” *Opt. Express*, vol. 20, no. 9, pp. 10095–10099, 2010.
- [21] R. Ahmad and M. Rochette, “Raman lasing in a chalcogenide microwire-based Fabry-Perot cavity,” *Opt. Lett.*, vol. 37, no. 21, pp. 4549–4551, 2012.
- [22] R. Ahmad and M. Rochette, “High efficiency and ultra broadband optical parametric four-wave mixing in chalcogenide-PMMA hybrid microwires,” *Opt. Express*, vol. 20, no. 9, pp. 9572–9580, 2012.

- [23] R. Ahmad and M. Rochette, "All-chalcogenide Raman-parametric laser, wavelength converter, and amplifier in a single microwire," *IEEE J. Sel. Topics Quantum Electron.*, vol. 20, no. 5, pp. 299–304, 2014.
- [24] R. Ahmad, M. Rochette, and C. Baker, "Fabrication of Bragg gratings in subwavelength diameter As_2Se_3 chalcogenide wires," *Opt. Lett.*, vol. 36, no. 15, pp. 2886–2888, 2011.
- [25] A. Al-Kadry, L. Li, M. El-Amraoui, T. North, Y. Messaddeq, and M. Rochette, "Broadband supercontinuum generation in all-normal dispersion chalcogenide microwires," *Opt. Lett.*, vol. 40, no. 20, pp. 4687–4690, 2015.
- [26] A. Dot, E. Meyer-Scott, R. Ahmad, M. Rochette, and T. Jennewein, "Converting one photon into two via four-wave mixing in optical fibers," *Phys. Rev. A*, vol. 90, no. 4, pp. 043808–043808, 2014.
- [27] E. Meyer-Scott, A. Dot, R. Ahmad, L. Li, M. Rochette, and T. Jennewein, "Power-efficient production of photon pairs in a tapered chalcogenide microwire," *Appl. Phys. Lett.*, vol. 106, no. 8, pp. 081111–081111, 2015.
- [28] J. Beugnot, R. Ahmad, M. Rochette, V. Laude, H. Maillotte, and T. Sylvestre, "Reduction and control of stimulated Brillouin scattering in polymer-coated chalcogenide optical microwires," *Opt. Lett.*, vol. 39, no. 3, pp. 482–485, 2014.
- [29] T. Godin, Y. Combes, R. Ahmad, M. Rochette, T. Sylvestre, and J. M. Dudley, "Far-detuned mid-infrared frequency conversion via normal dispersion modulation instability in chalcogenide microwires," *Opt. Lett.*, vol. 39, no. 7, pp. 1885–1888, 2014.
- [30] A. Al-Kadry, M. El-Amraoui, Y. Messaddeq, and M. Rochette, "Mode-locked laser based on chalcogenide microwires," *Opt. Lett.*, vol. 40, no. 18, pp. 4309–4312, 2015.
- [31] I. Jones, "Process monitoring methods in laser welding of plastics," *Joining Plast.*, 2006.
- [32] Y. Sun, S. Dai, P. Zhang, X. Wang, Y. Xu, Z. Liu, F. Chen, Y. Wu, Y. Zhang, R. Wang, and G. Tao, "Fabrication and characterization of multimaterial chalcogenide glass fiber tapers with high numerical apertures," *Opt. Express*, vol. 23, no. 18, pp. 23472–23483, 2015.
- [33] M. Liao, C. Chaudhari, G. Qin, X. Yan, C. Kito, T. Suzuki, Y. Ohishi, M. Matsumoto, and T. Misumi, "Fabrication and characterization of a chalcogenide-tellurite composite microstructure fiber with high nonlinearity," *Opt. Express*, vol. 17, no. 24, pp. 21608–21614, 2009.
- [34] E. Snitzer and R. Tumminelli, "SiO₂-clad fibers with selectively volatilized soft-glass cores," *Opt. Lett.*, vol. 14, no. 14, pp. 757–759, 1989.

- [35] P. Kaiser and H. W. Astle, “Low-loss single-material fibers made from pure fused silica,” *Bell System Tech. J.*, vol. 53, no. 6, pp. 1021–1039, 1974.
- [36] N. Granzow, S. P. Stark, M. A. Schmidt, A. S. Tverjanovich, L. Wondraczek, and P. Russell, “Supercontinuum generation in chalcogenide-silica step-index fibers,” *Opt. Express*, vol. 19, no. 21, pp. 21003–21010, 2011.
- [37] Kirk-Othmer, ed., *Kirk-Othmer Encyclopedia of Chemical Technology*, 5th edition. John Wiley & Sons, 2006.
- [38] I. T. Sorokina and K. L. Vodopyanov, eds., *Solid-State Mid-Infrared Laser Sources*. Springer Science & Business Media, 2003.
- [39] S. Hilzensauer, C. Giesin, J. Schleife, J. Gilly, S. Patterson, and M. T. Kelemen, “High-power diode lasers between 1.8 μm and 3.0 μm for military applications,” *Proc. SPIE*, p. 88980U, 2013.
- [40] A. Tsekoun, A. Lyakh, R. Maulini, M. Lane, T. Macdonald, R. Go, C. Kumar, and N. Patel, “High power and efficiency quantum cascade laser systems for defense and security applications,” *Proc. SPIE*, p. 73250L, 2009.
- [41] T. Day, M. Pushkarsky, D. Caffey, K. Cecchetti, R. Arp, A. Whitmore, M. Henson, and E. B. Takeuchi, “Quantum cascade lasers for defense and security,” *Proc. SPIE*, p. 889802, 2013.
- [42] V. A. Serebryakov, E. V. Boiko, N. N. Petrishchev, and A. V. Yan, “Medical applications of mid-IR lasers. Problems and prospects,” *J. Opt. Technol.*, vol. 77, no. 1, pp. 6–17, 2010.
- [43] U. Willer, M. Saraji, A. Khorsandi, P. Geiser, and W. Schade, “Near- and mid-infrared laser monitoring of industrial processes, environment and security applications,” *Opt. Laser Eng.*, vol. 44, no. 7, pp. 699–710, 2006.
- [44] M. Ebrahim-Zadeh and I. T. Sorokina, eds., *Mid-Infrared Coherent Sources and Applications*. Springer Science & Business Media, 2008.
- [45] A. K. Majumdar and J. C. Ricklin, eds., *Free-Space Laser Communications: Principles and Advances*. Springer Science & Business Media, 2010.
- [46] E. Luzhansky, F. Choa, S. Merritt, A. Yu, and M. Krainak, “Mid-IR free-space optical communication with quantum cascaded lasers,” *Proc. SPIE*, p. 946512, 2015.
- [47] A. Soibel, M. W. Wright, W. H. Farr, S. A. Keo, C. J. Hill, R. Q. Yang, and H. C. Liu, “Midinfrared interband cascade laser for free space optical communication,” *IEEE Photon. Technol. Lett.*, vol. 22, no. 2, pp. 121–123, 2010.

- [48] D. H. Titterton, “A review of the development of optical countermeasures,” *Proc. SPIE*, pp. 1–15, 2004.
- [49] B. Molocher, “Countermeasure laser development,” *Proc. SPIE*, p. 598902, 2005.
- [50] S. W. Henderson, C. P. Hale, J. R. Magee, M. J. Kavaya, and A. V. Huffaker, “Eye-safe coherent laser radar system at 2.1 μm using Tm, Ho:YAG lasers,” *Opt. Lett.*, vol. 16, no. 10, pp. 773–775, 1991.
- [51] P. Maddaloni, M. Paturzo, P. Ferraro, P. Malara, P. D. Natale, M. Gioffre, G. Coppola, and M. Iodice, “Mid-infrared tunable two-dimensional Talbot array illuminator,” *Appl. Phys Lett.*, vol. 94, no. 12, p. 121105, 2009.
- [52] A. B. Seddon, “Potential for using mid-infrared light for non-invasive, early-detection of skin cancers in vivo,” *Proc. SPIE*, p. 85760V, 2013.
- [53] A. Krier, ed., *Mid-Infrared Semiconductor Optoelectronics*. Springer, 2007.
- [54] W. Petrich, “Mid-infrared and Raman spectroscopy for medical diagnostics,” *Appl. Spectrosc. Rev.*, vol. 36, no. 2-3, pp. 181–237, 2001.
- [55] P. Werle, F. Slemr, K. Maurer, R. Kormann, R. Mucke, and B. Janker, “Near- and mid-infrared laser-optical sensors for gas analysis,” *Opt. Lasers Eng.*, vol. 37, no. 2-3, pp. 101–114, 2002.
- [56] E. A. Zlobina and S. I. Kablukov, “Fiber optical parametric oscillators,” *Instrum. Data Process.*, vol. 49, no. 4, pp. 363–382, 2013.
- [57] J. M. Dudley and J. R. Taylor, eds., *Supercontinuum Generation in Optical Fibers*. Cambridge University Press, 2010.
- [58] A. W. Snyder and J. Love, *Optical Waveguide Theory*. Chapman and Hall, 1983.
- [59] G. P. Agrawal, *Nonlinear Fiber Optics*, 5th edition. Academic, 2013.
- [60] D. Marcuse, *Light Transmission Optics*, 2nd edition. Van Nostrand Reinhold, 1982.
- [61] A. Yariv, *Optical Electronics in Modern Communications*, 5th edition. Oxford University Press, 1997.
- [62] S. Afshar and T. M. Monro, “A full vectorial model for pulse propagation in emerging waveguides with subwavelength structures part i: Kerr nonlinearity,” *Opt. Express*, vol. 17, no. 4, pp. 2298–2318, 2009.

- [63] S. Afshar, W. Q. Zhang, H. Ebendorff-Heidepriem, and T. M. Monro, "Small core optical waveguides are more nonlinear than expected: experimental confirmation," *Opt. Lett.*, vol. 34, no. 22, pp. 3577–3579, 2009.
- [64] M. E. Lines, "Oxide glasses for fast photonic switching: A comparative study," *J. Appl. Phys.*, vol. 69, no. 10, pp. 6876–6884, 1991.
- [65] M. Sheik-Bahae, D. Hagan, and E. V. Stryland, "Dispersion and band-gap scaling of the electronic Kerr effect in solids associated with two-photon absorption," *Phys. Rev. Lett.*, vol. 65, no. 1, p. 96, 1990.
- [66] C. Aversa, J. E. Sipe, M. Sheik-Bahae, and E. W. V. Stryland, "Third-order optical nonlinearities in semiconductors: The two-band model," *Phys. Rev. B*, vol. 50, no. 24, p. 18073, 1994.
- [67] V. P. Tzolov, M. Fontaine, N. Godbout, and S. Lacroix, "Nonlinear modal parameters of optical fibers: a full-vectorial approach," *J. Opt. Soc. Am. B*, vol. 12, no. 10, pp. 1933–1941, 1995.
- [68] V. P. Tzolov, M. Fontaine, N. Godbout, and S. Lacroix, "Nonlinear self-phase-modulation effects: a vectorial first-order perturbation approach," *Opt. Lett.*, vol. 20, no. 5, pp. 456–458, 1995.
- [69] M. Foster, K. Moll, and A. Gaeta, "Optimal waveguide dimensions for nonlinear interactions," *Opt. Express*, vol. 12, no. 13, pp. 2880–2887, 2004.
- [70] P. V. Mamyshev and S. V. Chernikov, "Ultrashort-pulse propagation in optical fibers," *Opt. Lett.*, vol. 15, no. 19, pp. 1076–1078, 1990.
- [71] P. L. Francois, "Nonlinear propagation of ultrashort pulses in optical fibers: total field formulation in the frequency domain," *J. Opt. Soc. Am. B*, vol. 8, no. 2, pp. 276–293, 1990.
- [72] K. J. Blow and D. Wood, "Theoretical description of transient stimulated Raman scattering in optical fibers," *IEEE J. Quantum Electron.*, vol. 25, no. 12, pp. 2665–2673, 1989.
- [73] W. Shuang-Chun, S. Wen-Hua, Z. Hua, F. Xi-Quan, Q. Lie-Jia, and F. Dian-Yuan, "Influence of high-order dispersions and Raman delayed response on modulation instability in microstructured fibres," *Chinese Phys. Lett.*, vol. 20, no. 6, pp. 852–854, 2003.
- [74] J. S. Sanghera, L. B. Shaw, P. Pureza, V. Q. Nguyen, D. Gibson, L. Busse, I. D. Aggarwal, C. M. Florea, and F. H. Kung, "Nonlinear properties of chalcogenide glass fibers," *Int. J. Appl. Glass Sci.*, vol. 1, no. 3, pp. 296–308, 2010.
- [75] C. B. Faust, *Modern Chemical Techniques*. RSC Publishing, 1992.

- [76] B. Pal, ed., *Frontiers in Guided Wave Optics and Optoelectronics*. InTech, 2010.
- [77] H. K. Choi, ed., *Long-Wavelength Infrared Semiconductor Lasers*. John Wiley & Sons, 2004.
- [78] E. Kapon, ed., *Semiconductor Lasers II, Materials and Structures*. Academic, 1999.
- [79] P. F. Moulton, G. A. Rines, E. V. Slobodtchikov, K. F. Wall, G. Frith, B. Samson, and A. L. G. Carter, "Tm-doped fiber lasers: fundamentals and power scaling," *IEEE Sel. Topics Quantum Electron.*, vol. 15, no. 1, pp. 85–92, 2009.
- [80] C. W. Ruby, M. J. F. Digonnet, and R. L. Byer, "Advances in 2- μm Tm-doped mode-locked fiber lasers," *Opt. Fiber Technol.*, vol. 20, no. 6, pp. 642–649, 2014.
- [81] Q. Wang, J. Geng, T. Luo, and S. Jiang, "Mode-locked 2 μm laser with highly thulium-doped silicate fiber," *Opt. Lett.*, vol. 34, no. 23, pp. 3616–3618, 2009.
- [82] V. Matsas, T. Newson, D. Richardson, and D. Payne, "Selfstarting passively mode-locked fiber ring soliton laser exploiting nonlinear polarisation rotation," *Electron. Lett.*, vol. 28, no. 15, pp. 1391–1393, 1992.
- [83] R. H. Stolen, J. Botineau, and A. Ashkin, "Intensity discrimination of optical pulses with birefringent fibers," *Opt. Lett.*, vol. 7, no. 10, pp. 512–514, 1982.
- [84] R. H. Stolen, "Fiber Raman lasers," *Fiber Integr. Opt.*, vol. 3, no. 1, pp. 21–51, 1980.
- [85] K. Inoue and H. Toba, "Wavelength conversion experiment using fiber four-wave mixing," *IEEE Photon. Technol. Lett.*, vol. 4, no. 1, pp. 69–72, 1992.
- [86] K. A. Rauschenbach, K. L. Hall, J. C. Livas, and G. Raybon, "All-optical pulse width and wavelength conversion at 10 Gb/s using a nonlinear optical loop mirror," *IEEE Photon. Technol. Lett.*, vol. 6, no. 9, pp. 1130–1132, 1994.
- [87] J. C. Knight, "Photonic crystal fibers," *Nature*, vol. 424, no. 6950, pp. 847–851, 2003.
- [88] W. F. Smith and J. Hashemi, *Foundations of Materials Science and Engineering*, 5th ed.. McGraw-Hill, 2011.
- [89] J. F. Rabek and J. P. Fouassier, eds., *Lasers in Polymer Science and Technology: Applications*, vol. 1. CRC Press, 1989.
- [90] A. A. Bettiol, S. V. Rao, T. C. Sum, J. A. V. Kan, and F. Watt, "Fabrication of optical waveguides using proton beam writing," *J. Cryst. Growth*, vol. 288, no. 1, pp. 209–212, 2006.
- [91] Thorlabs, Inc., *PMMA transmission*, <https://www.thorlabs.com>.

- [92] S. Kalpakjian and S. R. Schmid, eds., *Manufacturing engineering and technology*, 5th edition. Prentice Hall, 2005.
- [93] N. A. Fleck, W. J. Stronge, and J. H. Liu, “High strain-rate shear response of polycarbonate and polymethyl methacrylate,” *Proceedings of the Royal Society of London A: Mathematical, Physical and Engineering Sciences*, vol. 429, no. 1877, pp. 459–479, 1990.
- [94] Z. Ruff, D. Shemuly, X. Peng, O. Shapira, Z. Wang, and Y. Fink, “Polymer-composite fibers for transmitting high peak power pulses at 1.55 microns,” *Opt. Express*, vol. 18, no. 15, pp. 15697–15703, 2010.
- [95] G-S Plastic Optics, *Transmission curves*, <http://www.gsoptics.com/transmission-curves/>.
- [96] Y. J. Chang, C. K. Yu, H. S. Chiu, W. H. Yang, H. E. Lai, and P. J. Wang, “Simulations and verifications of true 3D optical parts by injection molding process,” *Proc. of ANTEC*, vol. 22, no. 24, pp. 253–258, 2009.
- [97] M. D. Chidley, *High numerical aperture injection-molded miniature objective for fiber-optic confocal reflectance microscopy*. PhD thesis, The University of Arizona, 2005.
- [98] N. G. Sultanova, I. D. Nikolov, and C. D. Ivanov, “Measuring the refractometric characteristics of optical plastics,” *Opt. Quant. Electron.*, vol. 35, no. 1, pp. 21–34, 2003.
- [99] W. J. Huang, F. C. Chang, and P. P. J. Chu, “Functionalization and chemical modification of cyclo olefin copolymers (COC),” *Polym.*, vol. 41, no. 16, pp. 6095–6101, 2000.
- [100] K. E. Herold and A. Rasooly, eds., *Lab on a Chip Technology: Fabrication and Microfluidics*, vol. 1. Caister Academic Press, 2009.
- [101] G. Khanarian and H. Celanese, “Optical properties of cyclic olefin copolymers,” *Opt. Eng.*, vol. 40, no. 6, pp. 1024–1029, 2001.
- [102] Thorlabs, Inc., *Cyclo Olefin Polymer transmission*, <https://www.thorlabs.com>.
- [103] B. Ellis and R. Smith, eds., *Polymers: A Property Database*, 2nd edition. CRC Press, 2008.
- [104] M. J. El-Hibri and S. A. Weinberg, *Polysulfones, Encyclopedia of Polymer Science and Technology*, 4th edition, vol. 4. John Wiley & Sons, 2001.
- [105] C. Baker, “Fabrication and analysis of As₂Se₃ based microtapers and couplers,” Master’s thesis, McGill University, 2011.
- [106] Solvay Advanced Polymers, L.L.C., *Optical Properties of Sulfone Polymers*, <http://www.solvay.com/>.

- [107] J. Bijwe, U. S. Tewari, and P. Vasudevan, "Friction and wear studies of bulk polyetherimide," *J. Mater. Sci.*, vol. 25, no. 1, pp. 548–556, 1990.
- [108] J. Belana, J. C. Canadas, J. A. Diego, M. Mudarra, R. Diaz, S. Friederichs, C. Jaimes, and M. J. Sanchis, "Physical ageing studies in polyetherimide ULTEM 1000," *Polym. Int.*, vol. 46, no. 1, pp. 29–32, 1998.
- [109] R. A. Belmontes and B. A. Hall, "Analysis of the self-contained breathing apparatus face piece for fire service use." Bachelor thesis, 2012.
- [110] M. Biron, *Thermosets and Composites: Material Selection, Applications, Manufacturing and Cost Analysis*, 2nd edition. Elsevier, 2014.
- [111] N. A. Adrova, M. I. Bessonov, L. A. Laius, and A. P. Rudakov, *Polyimides, A New Class of Thermally Stable Polymers*, vol. 7. CRC Press, 1970.
- [112] R. H. French, J. M. Rodriguez-Parada, M. K. Yang, R. A. Derryberry, M. F. Lemon, M. J. Brown, C. R. Haeger, S. L. Samuels, E. C. Romano, and R. E. Richardson, "Optical properties of materials for concentrator photovoltaic systems," in *Photovoltaic Specialists Conference (PVSC), IEEE*, pp. 000394–000399, 2009.
- [113] J. Hu, *Shape Memory Polymers and Textiles*. Elsevier, 2007.
- [114] Y. Zhang, J. Zhang, Y. Lu, Y. Duan, S. Yan, and D. Shen, "Glass transition temperature determination of poly (ethylene terephthalate) thin films using reflection-absorption FTIR," *Macromolecules*, vol. 37, no. 7, pp. 2532–2537, 2004.
- [115] V. Prajzler, P. Nekvindova, P. Hyps, O. Lyutakov, and V. Jerabek, "Flexible polymer planar optical waveguides," *Radioengineering*, vol. 23, no. 3, pp. 776–782, 2014.
- [116] Hitachi High-Technologies Corporation, *Measurement of Optical Characteristic of Plastic by UH4150 Spectrophotometer*, <http://www.hitachi-hightech.com/>.
- [117] Y. Wang, M. Rafailovich, J. Sokoly, D. Gersappe, T. Araki, Y. Zou, A. D. L. Kilcoyne, H. Ade, G. Marom, and A. Lustiger, "Substrate effect on the melting temperature of thin polyethylene films," *Phys. Rev. Lett.*, vol. 96, no. 2, p. 028303, 2006.
- [118] D. R. Lide, ed., *CRC Handbook of Chemistry and Physics*, 85th edition. CRC Press, 2004.
- [119] FILMETRICS, Inc., *Refractive index of Polyethylene, PE, Polyethene*, 2016.
- [120] D. L. Snavely and J. Dubsky, "Near-IR spectra of polyethylene, polyethylene glycol, and polyvinylethyl ether," *J. Polym. Sci. A Polym. Chem.*, vol. 34, no. 13, pp. 2575–2579, 1996.
- [121] M. Yamazaki, "Industrialization and application development of cyclo-olefin polymer," *J. Mol. Catal. A: Chem.*, vol. 213, no. 1, pp. 81–87, 2004.

- [122] P. S. Nunes, P. D. Ohlsson, O. Ordeig, and J. P. Kutter, "Cyclic olefin polymers: emerging materials for lab-on-a-chip applications," *Microfluid Nanofluid*, vol. 9, no. 2, pp. 145–161, 2010.
- [123] H. Yaghoubi and N. Taghavinia, "Surface chemistry of atmospheric plasma modified polycarbonate substrates," *Appl. Surf. Sci.*, vol. 257, no. 23, pp. 9836–9839, 2011.
- [124] D. Dorrnian, Z. Abedini, A. Hojabri, and M. Ghoranneviss, "Structural and optical characterization of PMMA surface treated in low power nitrogen and oxygen RF plasmas," *J. Non-Oxide Glasses*, vol. 1, no. 3, pp. 217–229, 2009.
- [125] I. Kaminow, T. Li, and A. E. Willner, *Optical Fiber Telecommunications*, 6th edition. Academic, 2013.
- [126] J. Workman and L. Weyer, *Practical Guide to Interpretive Near-Infrared Spectroscopy*. CRC Press, 2007.
- [127] W. Groh, "Overtone absorption in macromolecules for polymer optical fibers," *J. Non-Oxide Glasses*, vol. 189, no. 12, pp. 2861–2874, 1988.
- [128] T. N. Sorrell, *Organic Chemistry*, 2nd edition. University Science Books, 2006.
- [129] J. Malek and J. Shanelova, "Structural relaxation of As_2Se_3 glass and viscosity of supercooled liquid," *J. Non-Cryst. Solids*, vol. 351, no. 43, pp. 3458–3467, 2005.
- [130] D. W. Henderson and D. G. Ast, "Viscosity and crystallization kinetics of As_2Se_3 ," *J. Non-Cryst. Solids*, vol. 64, no. 1-2, pp. 43–70, 1984.
- [131] A. S. Tverjanovich, "Temperature dependence of the viscosity of chalcogenide glass-forming melts," *Glass Phys. Chem.*, vol. 29, no. 6, pp. 532–536, 2003.
- [132] T. Tofteber and E. Andreassen, "Injection moulding of microfeatured parts," *Proceedings of the Polymer Processing Society 24th Annual Meeting*, 2008.
- [133] P. Lomellini, "Viscosity-temperature relationships of a polycarbonate melt: Williams-Landel-Ferry versus Arrhenius behavior," *Die Makromol. Chem.*, vol. 193, no. 1, pp. 69–79, 1992.
- [134] C. Liu, J. He, R. Keunings, and C. Bailly, "New linearized relation for the universal viscosity-temperature behavior of polymer melts," *Macromolecules*, vol. 39, no. 25, pp. 8867–8869, 2006.
- [135] W. Martienssen and H. Warlimont, eds., *Springer Handbook of Condensed Matter and Materials Data*. Springer Science & Business Media, 2005.

- [136] X. Lin, A. Kelly, D. Ren, M. Woodhead, P. Coates, and K. Wang, “Geometrical dependence of viscosity of polymethylmethacrylate melt in capillary flow,” *J. Appl. Polym. Sci.*, vol. 130, no. 5, pp. 3384–3394, 2013.
- [137] F. W. Billmeyer, *Textbook of Polymer Science*, 3rd edition. John Wiley & Sons, 1984.
- [138] J. E. Mark, ed., *Physical Properties of Polymer Handbook*, 2nd edition. Springer Science & Business Media, 2007.
- [139] Zeon Chemicals L. P., *The lowest autofluorescent injection-moldable plastic*, <http://www.zeonex.com/life-sciences.aspx>.
- [140] M. N. Eakins, “New plastics for old vials,” *Bioprocess International*, vol. 3, pp. 52–58, 2005.
- [141] Zeon Chemicals L. P., *World’s foremost optical polymer for precision-molded optics*, <http://www.zeonex.com/optics.aspx>.
- [142] J. Nishii, T. Yamashita, and T. Yamagishi, “Chalcogenide glass fiber with a core-cladding structure,” *Appl. Opt.*, vol. 28, no. 23, pp. 5122–5127, 1989.
- [143] F. Languy, K. Fleury, C. Lenaerts, J. Loicq, D. Regaert, T. Thibert, and S. Habraken, “Flat Fresnel doublets made of PMMA and PC: combining low cost production and very high concentration ratio for CPV,” *Opt. Express*, vol. 19, no. 103, pp. A280–A294, 2011.
- [144] S. N. Kasarova, N. G. Sultanova, C. D. Ivanov, and I. D. Nikolov, “Analysis of the dispersion of optical plastic materials,” *Opt. Materials*, vol. 29, no. 11, pp. 1481–1490, 2007.
- [145] C. Pollock and M. Lipson, *Integrated Photonics*. Springer Science & Business Media, 2003.
- [146] P. Russell, “Photonic crystal fibers,” *Science*, vol. 299, no. 5605, pp. 358–362, 2003.
- [147] L. Li, A. Al-Kadry, N. Abdukerim, and M. Rochette, “Design, fabrication and characterization of PC, COP and PMMA-cladded As₂Se₃ microwires,” *Opt. Mater. Express*, vol. 6, no. 3, pp. 912–921, 2016.
- [148] Y. Sun, S. Dai, P. Zhang, X. Wang, Y. Xu, Z. Liu, F. Chen, Y. Wu, Y. Zhang, R. Wang, and G. Tao, “Fabrication and characterization of multimaterial chalcogenide glass fiber tapers with high numerical apertures,” *Opt. Express*, vol. 23, no. 18, pp. 23472–23483, 2015.
- [149] J. G. Drobny, *Technology of fluoropolymers*, 2nd edition. CRC Press, 2008.
- [150] T. Tsutsumino, Y. Suzuki, N. Kasagi, and Y. Sakane, “Seismic power generator using high-performance polymer electret,” in *In 19th IEEE International Conference on Micro Electro Mechanical Systems*, pp. 98–101, 2006.

- [151] G. Gupta, *Microring resonator based filters and modulators: optical coupling control and applications to digital communications*. PhD thesis, University of Southern California, 2008.
- [152] J. C. Salamone, ed., *Concise polymeric materials encyclopedia*. CRC Press, 1998.
- [153] J. H. Lowry, J. S. Mendlowitz, and N. S. Subramanian, "Optical characteristics of the Teflon AF fluoro-plastic materials," in *In Optical Surfaces Resistant to Severe Environments*, pp. 142–151, 1991.
- [154] Z. Guo, ed., *Progress in Optical Fibers Research*. Nova Science Publishers, 2008.
- [155] M. K. Yang, R. H. French, and E. W. Tokarsky, "Optical properties of Teflon AF amorphous fluoropolymers," *J. Micro. Nanolithogr. MEMS MOEMS*, vol. 7, no. 3, pp. 033010–033010, 2008.
- [156] Y. P. Khanna, "The melting temperature of polytetrafluoroethylene," *J. Mater. Sci. Lett.*, vol. 7, no. 8, pp. 817–818, 1988.
- [157] P. J. Rae and D. M. Dattelbaum, "The properties of poly (tetrafluoroethylene)(PTFE) in compression," *Polym.*, vol. 45, no. 22, pp. 7615–7625, 2004.
- [158] W. Groh and A. Zimmermann, "What is the lowest refractive index of an organic polymer?," *Polym.*, vol. 24, no. 25, pp. 6660–6663, 1991.
- [159] P. Kaiser, A. C. Hart, and L. L. Blyler, "Low-loss FEP-clad silica fibers," *Appl. Opt.*, vol. 14, no. 1, pp. 156–162, 1975.
- [160] B. Gupta and G. G. Scherer, "Radiation-induced grafting of styrene onto FEP^a films: Structure and thermal behaviour of copolymers," *Die Angew. Makromol. Chem.*, vol. 210, no. 1, pp. 151–164, 1993.
- [161] Z. Liu, Y. Song, Y. Shangguan, and Q. Zheng, "Conductive behavior of composites composed of carbon black-filled ethylene-tetrafluoroethylene copolymer," *J. Mater. Sci.*, vol. 42, no. 8, pp. 2903–2906, 2007.
- [162] V. Saarinen, M. Karesoja, T. Kallio, M. Paronen, and K. Kontturi, "Characterization of the novel ETFE-based membrane," *J. Membrane Sci.*, vol. 280, no. 1, pp. 20–28, 2006.
- [163] D. M. Esterly, "Manufacturing of Poly(vinylidene fluoride) and evaluation of its mechanical properties," Master's thesis, Virginia Polytechnic Institute and State University, 2002.
- [164] E. Merchand, *Gradient Index Optics*. Academic, 1978.
- [165] C. C. Ibeh, *Thermoplastic Materials: Properties, Manufacturing Methods, and Applications*. CRC Press, 2011.

- [166] J. Brandrup, E. H. Immergut, E. A. Grulke, A. Abe, and D. R. Bloch, eds., *Polymer Handbook*, vol. 7. John Wiley & Sons, 1989.
- [167] Asahi Glass Co., *CYTOP*, <http://www.agc.com/kagaku/shinsei/cytop/en/>.
- [168] D. S. Montero, *Multimode fibre broadband access and self-referencing sensor networks*. PhD thesis, Universidad Carlos III de Madrid, 2011.
- [169] P. A. Belanger, *Optical Fiber Theory: A Supplement to Applied Electromagnetism*, vol. 5. World Scientific, 1993.
- [170] D. M. Hoffman and A. L. Shields, "Rheological properties & molecular weight distributions of four perfluorinated thermoplastic polymers," *Polym. Prepr.*, vol. 50, no. 2, p. 156, 2009.
- [171] C. Stamboulides and S. G. Hatzikiriakos, "Rheology and processing of molten poly (methyl methacrylate) resins," *Int. Polym. Proc.*, vol. 21, no. 2, pp. 155–163, 2006.
- [172] C. Baker and M. Rochette, "A generalized heat-brush approach for precise control of the waist profile in fiber tapers," *Opt. Mater. Express*, vol. 6, no. 1, pp. 1065–1076, 2011.
- [173] T. A. Cerni, "An infrared hygrometer for atmospheric research and routine monitoring," *J. Atmos. Oceanic Technol.*, vol. 11, no. 2, pp. 445–462, 1994.
- [174] C. Jauregui, J. Limpert, and A. Tunnermann, "High-power fibre lasers," *Nat. Photonics*, vol. 7, no. 11, pp. 861–867, 2013.
- [175] W. Shi, Q. Fang, X. Zhu, R. A. Norwood, and N. Peyghambarian, "Fiber lasers and their applications [Invited]," *Appl. Opt.*, vol. 53, no. 28, pp. 6554–6568, 2014.
- [176] M. Bernier, V. Michaud-Belleau, S. Levasseur, V. Fortin, J. Genest, and R. Vallee, "All-fiber DFB laser operating at 2.8 μm ," *Opt. Lett.*, vol. 40, no. 1, pp. 81–84, 2015.
- [177] V. Fortin, M. Bernier, S. T. Bah, and R. Vallee, "30 W fluoride glass all-fiber laser at 2.94 μm ," *Opt. Lett.*, vol. 41, no. 3, pp. 559–562, 2016.
- [178] V. Fortin, F. Maes, M. Bernier, S. T. Bah, M. D'Auteuil, and R. Vallee, "Watt-level erbium-doped all-fiber laser at 3.44 μm ," *Opt. Lett.*, vol. 40, no. 12, pp. 2882–2885, 2015.
- [179] R. E. Slusher, G. Lenz, J. Hodelin, J. Sanghera, L. B. Shaw, and I. D. Aggarwal, "Large Raman gain and nonlinear phase shifts in high purity As_2Se_3 chalcogenide fibers," *J. Opt. Soc. Am. B*, vol. 21, no. 6, pp. 1146–1155, 2004.
- [180] L. Li, N. Abdukerim, and M. Rochette, "Chalcogenide optical microwires cladded with fluorine-based CYTOP," *Opt. Express*, vol. 24, no. 17, pp. 18931–18937, 2016.

-
- [181] N. Abdukerim, L. Li, and M. Rochette, “Chalcogenide-based optical parametric oscillator at 2 μm ,” *Opt. Lett.*, vol. 41, no. 18, pp. 4364–4367, 2016.
- [182] P. Apiratikul, J. J. Wathen, G. A. Porkolab, B. Wang, L. He, T. E. Murphy, and C. J. K. Richardson, “Enhanced continuous-wave four-wave mixing efficiency in nonlinear AlGaAs waveguides,” *Opt. Express*, vol. 22, no. 22, pp. 26814–26824, 2014.
- [183] L. Zhang, T. H. Tuan, H. Kawamura, K. Nagasaka, T. Suzuki, and Y. Ohishi, “Highly efficient picosecond degenerate four-wave mixing in a tellurite microstructured optical fiber,” *Appl. Phys. Express*, vol. 9, no. 6, p. 062501, 2016.
- [184] C. S. Brès, S. Zlatanovic, A. O. J. Wiberg, and S. Radic, “Continuous-wave four-wave mixing in cm-long chalcogenide microstructured fiber,” *Opt. Express*, vol. 19, no. 26, pp. B621–B627, 2011.
- [185] Q. Lin, O. J. Painter, and G. P. Agrawal, “Nonlinear optical phenomena in silicon waveguides: Modeling and applications,” *Opt. Express*, vol. 15, no. 25, pp. 16604–16644, 2007.
- [186] Q. Lin, J. Zhang, P. M. Fauchet, and G. P. Agrawal, “Ultrabroadband parametric generation and wavelength conversion in silicon waveguides,” *Opt. Express*, vol. 14, no. 11, pp. 4786–4799, 2006.